Paleo-hydrogeologic Models of Freshwater Emplacement on the Atlantic Continental Shelf: Offshore Martha's Vineyard Island

by

Whitney DeFoor

Submitted in Partial Fulfillment

of the Requirements for the Degree of

Master of Science in Hydrology

New Mexico Institute of Mining and Technology

Socorro, New Mexico

December, 2010

I want to thank my academic and research advisor, Dr. Mark Person, for this research project and his frequent availability, assistance, and guidance. Dr. Person provided me with several experiences that would help me in my future careers. I appreciate all he has taught me about science and research, and especially his recommendations and efforts in helping me get a job. I also desire to thank my advisory committee, Dr. Fred Phillips and Dr. John Wilson, for their knowledge and counsel. I appreciate my advisory committees' straight forward approach to research, as well as their encouragement for me to look at different aspects, views, and applications of my study. I also want to thank my committee for steering me towards working as a teaching assistant. I found the experience broadening and informative.

I also owe much gratitude to my collaborators on this work, Dr. Brandon Dugan, Dr. Daniel Lizarralde, and Jacob Siegel. We became well acquainted after spending two weeks in close quarters on a research vessel and since then they have had integral roles in my research project. They helped me focus my research and they also provided me with indispensable data, which I could not have done without.

Special thanks to Dr. Hans Christian Larsen and Dr. Denis Cohen for their collaboration and support in a Greenland study, parts of which fingered into my thesis project. Further, my fellow graduate students were great moral busters and friends. They provided me with much needed technical help (especially my lab mates in the third floor computer lab) and with many great memories. I can not forget the behind the scenes efforts of the EES faculty and staff.

Finally, over the past two years, my husband (Aaron Greenwood), parents (Jim and Sally DeFoor), sister (Brandyn DeFoor Horrall), and in-laws provided me with continual encouragement and support, even though they often faced a grim and retentive recipient.

This research was supported by the National Science Foundation Ocean Science Grant (OCE-082426) to Brandon Dugan, Mark Person, and Dan Lizarralde.

Whitney DeFoor
New Mexico Institute of Mining and Technology
December, 2010

ABSTRACT

We conducted a series of regional-scale reconstructions of the Pleistocene hydrogeology of the continental shelf offshore of Martha's Vineyard Island using the finite element method. The models incorporated multiple groundwater impelling mechanisms, including sedimentation, subsidence, erosion, sea-level loading, variable-density flow, ice-sheet loading, and lithospheric flexure. Using detailed hydro-stratigraphy acquired from high resolution multi-channel seismic data, we attempted to determine the influence of the above fluid impelling mechanisms and permeability on offshore fresh water, isotope ($\delta^{18}O$), hydraulic head, and groundwater age distribution. This information can be used to constrain future drilling locations in which relatively fresh pore fluids may be found. We found that compaction associated with sedimentation had a dominant influence on present-day hydraulic heads, inducing overpressuring and restricting freshwater emplacement. Underpressuring was induced by sea-level fluctuations and erosion. Density instabilities tended to increase the salinity in nearshore sediments. Ice-sheet loading increased the percentage of brackish-to-fresh pore fluids ($< 5\ ppt$) compared to ice free simulations, actually doubling brackish-to-fresh pore fluids when the more expansive ice sheet is present. Due to dispersive mixing, few simulated pore-fluid $\delta^{18}O$ signatures returned the glacial end member value. Simulated groundwater ages were relatively old; ages between 0 and 50 ky were restricted to the nearshore environment and shallow depths across the continental shelf. Past local topographic gradients, not in present-day stratigraphy, could have increased fresh water emplacement into shallow aquifers. We

found that offshore results were highly sensitive to sand and clay permeability, as well as Pleistocene sediment stratigraphy. However, nearshore salinity and pore pressure were relatively insensitive to permeability and glacial history. Salinity and hydraulic head data from Martha's Vineyard and Nantucket Island provided some degree of ground truth to our models, however more data is needed to constrain the hydro-stratigraphy and glacial history offshore of Martha's Vineyard Island. Model results suggest that proposed IODP boreholes should be deepened to about 1.3 km to maximize chances of encountering fresh water.

Keywords: Continental Shelf; Hydrology; Pleistocene; Glaciations; Martha's Vineyard; Fresh Water; Laurentide Ice Sheet

CONTENTS

LIST OF TABLES

LIST OF FIGURES

This thesis is accepted on behalf of the faculty of the Institute by the following committee:

Mark Person, Advisor

I release this document to the New Mexico Institute of Mining and Technology.

Whitney DeFoor Date

CHAPTER 1

BACKGROUND

In 1976, over a dozen offshore boreholes were drilled on the Atlantic continental shelf, from Florida to Massachusetts, in hopes of discovering petroleum resources and obtaining a better understanding of the mineralogy, lithology, and paleo-environments of the Atlantic continental shelf (bullets, Figures 1.1) (Hathaway, 1981; Hathaway et al., 1979). Surprisingly, instead of petroleum, relatively brackish-to-fresh water (0 to 5 ppt; Figure 1.2) was found in the pore fluids of coarse-grained sand units to depths greater than 500 m and extending over 100 km offshore (Figure 1.3). Some wells, such as USGS 6001, were found to be modestly overpressured by about 7.5 m above sea-level (Figure 1.4) (Marksamer, 2007). Similar salinity conditions have also been documented more recently offshore Suriname (Figure 1.3) (Kooi and Groen, 2001) and coastal Europe (Edmunds et al., 2001; Manzano et al., 2001). Coarse Pleistocene deposits that act as important coastal aquifers in Spain (Manzano et al., 2001) and along the North Sea European coastline (Edmunds et al., 2001), contain relatively fresh water offshore in excess of 100 m depth below sea-level. This offshore fresh water represents a large, albeit nonrenewable resource that could be utilized by megacities in coastal regions of the world (Cohen et al., 2010). The volume of fresh water (less than 1 ppt) on continental shelf in New England is estimated to be 1300 km^3, up to 10^4 km^3 along the entire North American Atlantic seaboard, and $3x10^5$ km^3 globally along all passive margins (Cohen et al., 2010).

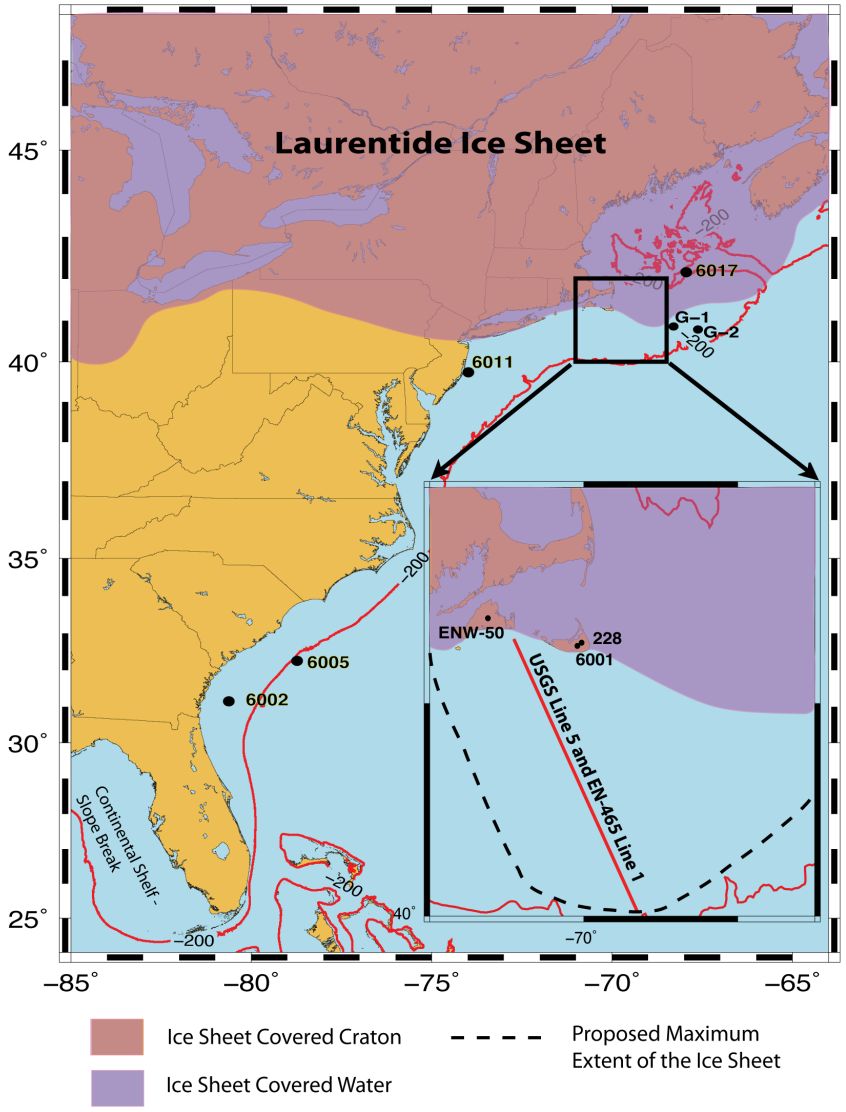

Figure 1.1: Four AMCOR boreholes (6002, 6005, 6011, and 6017) and two Cost boreholes (G-1 and G-2) off the coast of the Massachusetts, New Jersey, South Carolina, and Georgia (black circles in large map). Well 228, well ENW-50, and well USGS 6001 are also present (see map inset). USGS Seismic Line 5 and EN-465 Seismic Line 1 are also shown. USGS Line 5 corresponds with the cross-section used for this study. The continental shelf-slope break is at -200 m and is presented as a red line. The maximum known ice sheet extent during the Wisconsin glaciation (20 ka) is indicated by the purple area (Dyke et al., 2002; Hughes et al., 1981; Marshall et al., 2000). Data from EN-465 Line 1 suggests that the ice sheet may have extended near the continental shelf-slope break offshore of Martha's Vineyard Island during the Pleistocene (black dashed line in map inset). Sediment data from Cost G-1 and Cost G-2 were used to determine the stratigraphy.

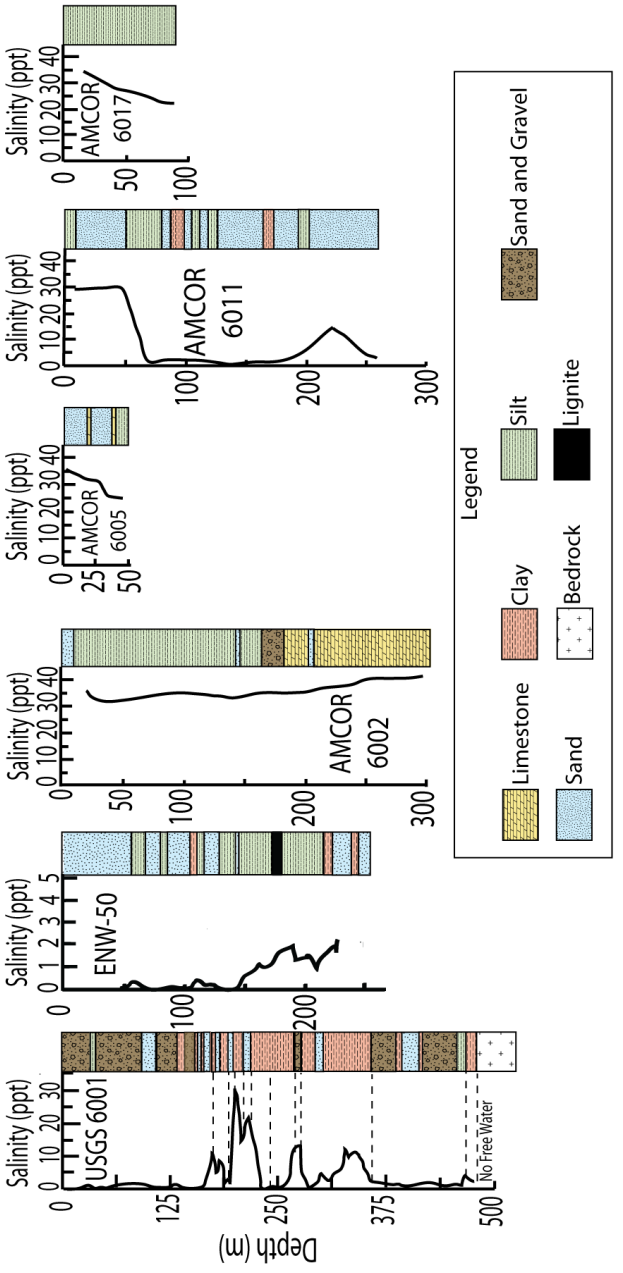

Figure 1.2: The pore-fluid salinity (ppt) and stratigraphy of boreholes and wells shown in Figure 1.1. Notice the scale of ENW-50 salinity plot has a smaller salinity range than the other boreholes and wells. The depth of USGS 6001 is around 2 to 5 times deeper than the other boreholes and wells.

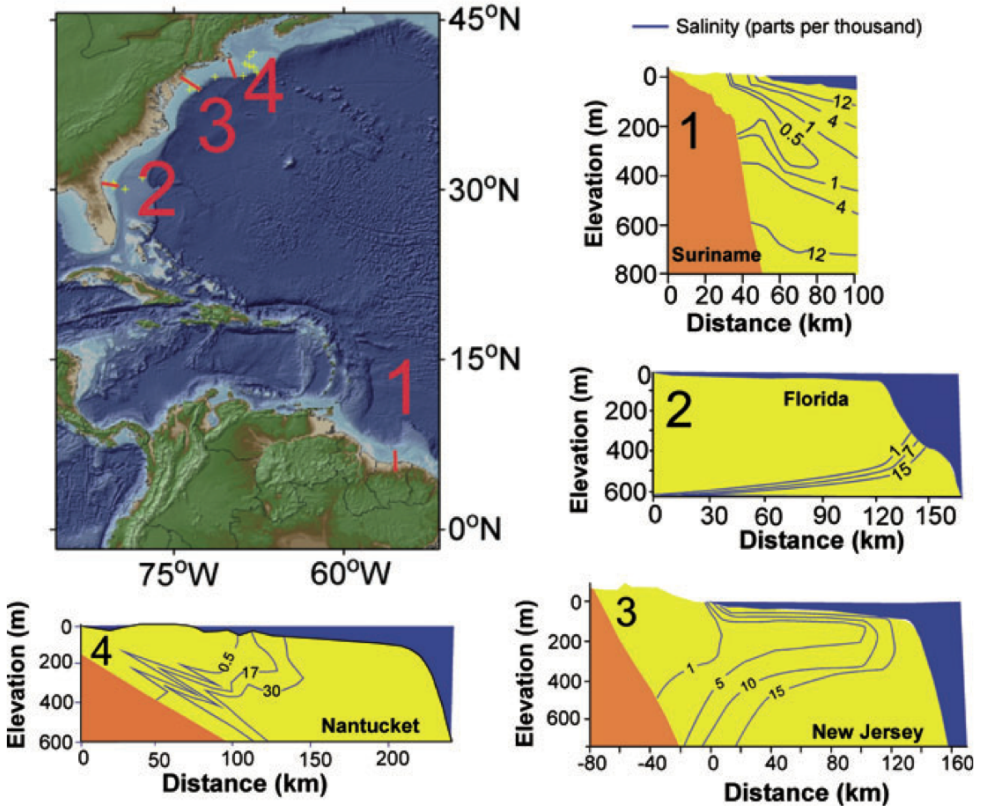

Figure 1.3: Salinity distribution (ppt) for four cross-sections (1 to 4) along the Atlantic continental shelf, extending from North America to South America (Cohen et al., 2010; Hathaway et al., 1979; Johnston, 1983; Kooi and Groen, 2001; Marksamer, 2007). Corresponding red lines and numbers on the map designate the locations of cross-sections 1-4. Orange and yellow shaded patterns represent crystalline bedrock and continental shelf sedimentary rocks, respectively. This figure was taken from Cohen et al. (2010).

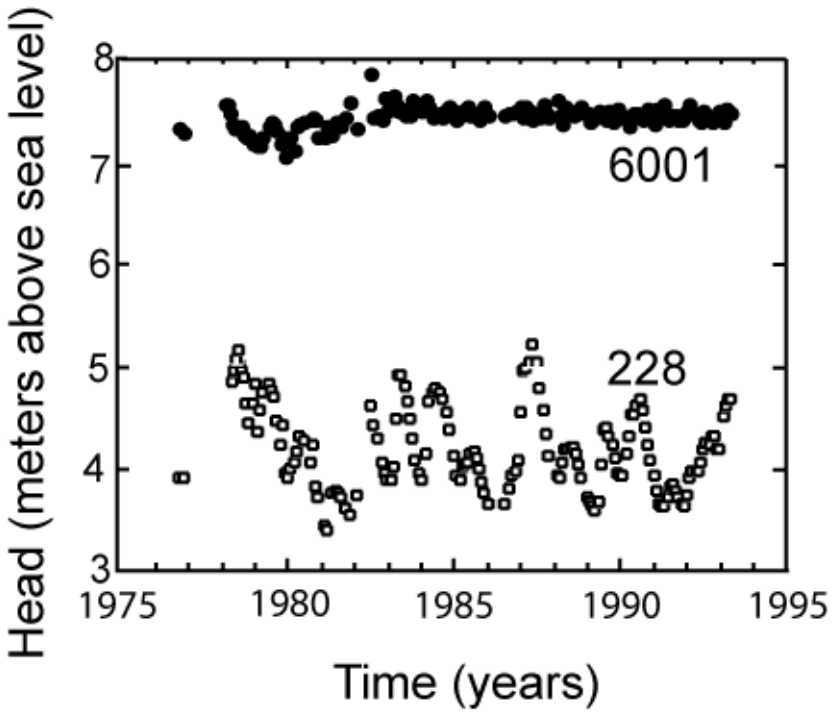

Figure 1.4: Temporal changes in hydraulic heads in Cretaceous aquifers in USGS 6001 and water table elevation (well 228) on Nantucket Island, Massachusetts. The locations of wells USGS 6001 and 228 are shown in Figure 1.1. Well 228 is located less than 100 *m* from USGS 6001

Pore fluids on Martha's Vineyard Island are completely fresh to depths of at least 225 m (Well ENW-50; Figure 1.2). USGS well 6001, drilled on Nantucket Island, indicates a correlation between salinity and sediment permeability (Figure 1.2). Sandy (relatively higher permeability) units found in these wells tended to have lower salinities levels ($< 6\ ppt$) than silty-clay (lower permeability) units, which have salinities that range between 30 % and 70 % seawater (Hall et al., 1980; Person et al., 2003). This suggests that fresh water was emplaced sometime after deposition of marine units. The saline water contained within the low permeability units have much longer residence times. Parabolic salinity profiles in confining units and relatively fresh water in permeable sand suggests disequilibrium of the system with current sea-level conditions (Person et al., 2003).

What is the source of the coastal offshore fresh water, particularly offshore of Martha's Vineyard Island, Massachusetts? Several mechanisms have been proposed (Figure 1.5). In some instances, relatively fresh water could be the extension of onshore, shore-normal groundwater flow offshore. For example, the limestone dominated Floridian Aquifer System extends at least 100 km offshore mainland Florida, providing a vital fresh water source for the Florida Keys (Wilson, 1980). Density effects due to seawater tend to inhibit offshore migration of fresh water, unless onshore hydraulic heads are high. In New England, present-day near-shore topographic relief is not high enough to induce emplacement of fresh water far offshore. Maximum water levels of Martha's Vineyard Island are about 3 - 4 m above sea level.

Kohout et al. (1977) was one of the first to suggest that freshwater pore fluids on Nantucket were likely emplaced during sea-level low-stands (Kohout et al., 1977). When sea levels were low, shore-normal topographic hydraulic-head gradients, as well as vertical infiltration associated with local flow, induced

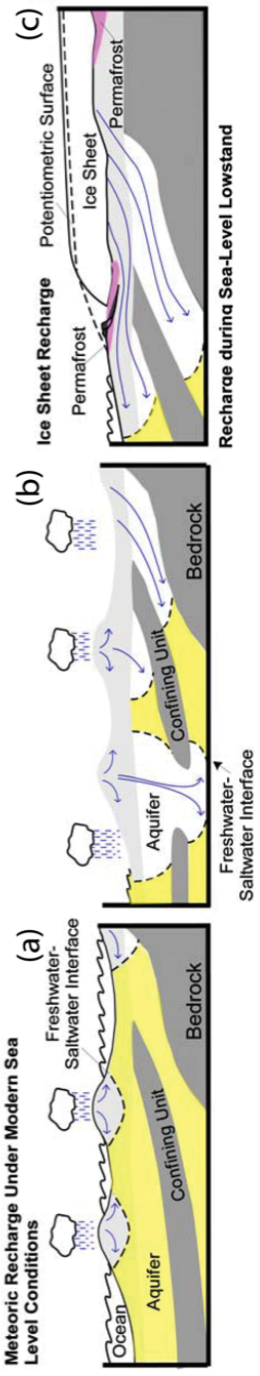

Figure 1.5: Compared to variable-density groundwater flow associated with (a.) modern sea-level conditions, (b.) past sea-level low-stands, and (c.) sub-ice-sheet recharge provide compelling mechanisms to explain freshwater emplacement in the continental shelf sediments.

freshwater infiltration into sediments. Environmental isotopic data ($\delta^{18}O$) obtained from U/Th dating of coral and foraminifera from deep-sea cores indicate that sea-level was 120 m lower (compared to present day) during the Last Glacial Maximum / Wisconsin glaciation (about 20 ka), compared to present-day sea level (Peltier, 1998). Recently, analysis of nobel gas geochemistry of the Floridian Aquifer System indicates that during Pleistocene sea-level low-stands induced shore normal lateral flow and recharge of the entire aquifer system with meteoric waters (Morrissey et al., 2010). Today, hydraulic head data suggests a reversal of groundwater flow has occurred, associated with modern sea-level high-stands. In New England, submarine canyons exposed during sea-level low-stand may have provided a source of modest topographic relief. The associated hydraulic gradient may have helped to drive fresh water deep into continental-shelf sediments (Person et al., 2003; Pratson et al., 1994).

The presence of ice sheets on the Atlantic continental shelf in New England during the Pleistocene may have played an important role in freshwater emplacement by increasing the hydraulic-head gradient of underlying sediments (Engelhardt and Kamb, 1997; Hooyer and Iverson, 2002; Person et al., 2007). The Laurentide Ice Sheet covered large portions of North America during the Pleistocene (Hughes et al., 1981). At about 22 ka the Laurentide Ice Sheet reached a maximum thickness between 3.9 - 4.5 km over northern Manitoba and Hudson Bay, and extended $5,000$ km across North America, from Martha's Vineyard Island, Massachusetts to the northern boarder of the Yukon Territory (Hughes et al., 1981; Marshall et al., 2000). In the area of Cape Cod, Martha's Vineyard Island, and Nantucket Island the ice sheet rapidly decreased from about 1 km thick on Cape Cod to 0 km thick at its toe on Nantucket Island and Martha's Vineyard Island (Hughes et al., 1981; Marshall et al., 2000). North of Nantucket, along Georges

Bank, the Laurentide Ice Sheet is thought to have extended out close to the continental shelf-slope break during the Wisconsin glaciation (Hughes et al., 1981; Schlee and Pratt, 1970). Geochemical tracers and numerical reconstructions of Pleistocene hydrogeologic conditions suggest that the Laurentide Ice Sheet substantially increased infiltration rates all across North America (Grasby et al., 2000; Lemieux and Sudicky, 2010; McIntosh and Walter, 2005; Person et al., 2003). Seepage from proglacial lakes that formed in Nantucket Sound, Cape Cod Bay, Block Island Sound, and Long Island Sound could have also played a significant role in inducing freshwater infiltration into Atlantic continental-shelf aquifers (Marksamer, 2007; Uchupi et al., 1996).

Today there is evidence of excess head conditions on the Atlantic continental shelf. Dugan and Flemings (2000, 2002) presented evidence of undercompacted clays near the continental shelf-slope break, suggesting near lithostatic pressures. Overpressuring is a result of glacial loading and rapid sedimentation. Rapid sedimentation likely occurred during deglaciation (Breckenridge et al., 2004). These overpressures drive groundwater shoreward and represent a competing force preventing freshwater emplacement. Underpressuring (i.e. sub-hydrostatic heads) is likely a result of sea-level rise, rapid deglaciation, and erosion. Free-convection due to density instabilities induces gravity / buoyancy driven flow when relatively dense seawater overruns less dense fresh water, such as might occur during sea-level rise (Groen et al., 2000; Kooi and Groen, 2001).

Several hydrogeologic studies have investigated the impacts of ice sheets and sea-level low-stands on continental-shelf hydrogeologic systems. These studies suggest that sea-level low-stands alone can produce freshwater infiltration into offshore aquifers (80 *km* offshore). Ice-sheet loading will promote periods

of significant influx of fresh water into offshore aquifers (up to 150 km offshore) if the confining units are thin and the aquifers permeable ($10^{-11}m^2$) (Kooi and Groen, 2001; Marksamer, 2007; Person et al., 2003). However, these conditions only occur for a few thousand years each glacial cycle, as the continental shelf represents the terminus of the Laurentide Ice Sheet. Nevertheless, ice sheets could have a substantial effect on continental groundwater flow, including increasing groundwater and nutrient fluxes and local reversal of the hydraulic gradient (Hood et al., 2009; Lemieux et al., 2008a). Relatively high-resolution models that take into account the influence of density on flow (variable-density flow) find that saltwater overlying fresh water on the continental shelf promotes instabilities and meter-scale fingering of saline and fresh water (Kooi and Groen, 2001). While more coarsely discretized regional models of the continental-shelf hydrology bring to light important dynamics in glacio-hydrogeologic systems, these models relied on simple and idealized stratigraphy based on coarse geophysical data and sparsely-spaced well data (Cohen et al., 2010; Marksamer, 2007; Person et al., 2003). These continental-shelf scale models can't resolve meter-scale fingering described above.

A seismic survey was conducted in support of our Integrated Ocean Drilling Program (IODP) proposal to complete 4-6 boreholes on the Atlantic continental shelf offshore Martha's Vineyard Island. The acquired high-resolution seismic data provides a better understanding of the stratigraphy and depositional units offshore Martha's Vineyard (Figure 1.6). The data reveals a series of transgressive sequences and unconformities. Shoreward-dipping reflectors (the shore is towards the North-West) near the eastern edge of EN-465 Line 5 are suggestive of glacial erosion and/or glacio-tectonic deformation and indicates that the Laurentide Ice Sheet may have extended close to the continental shelf-slope break

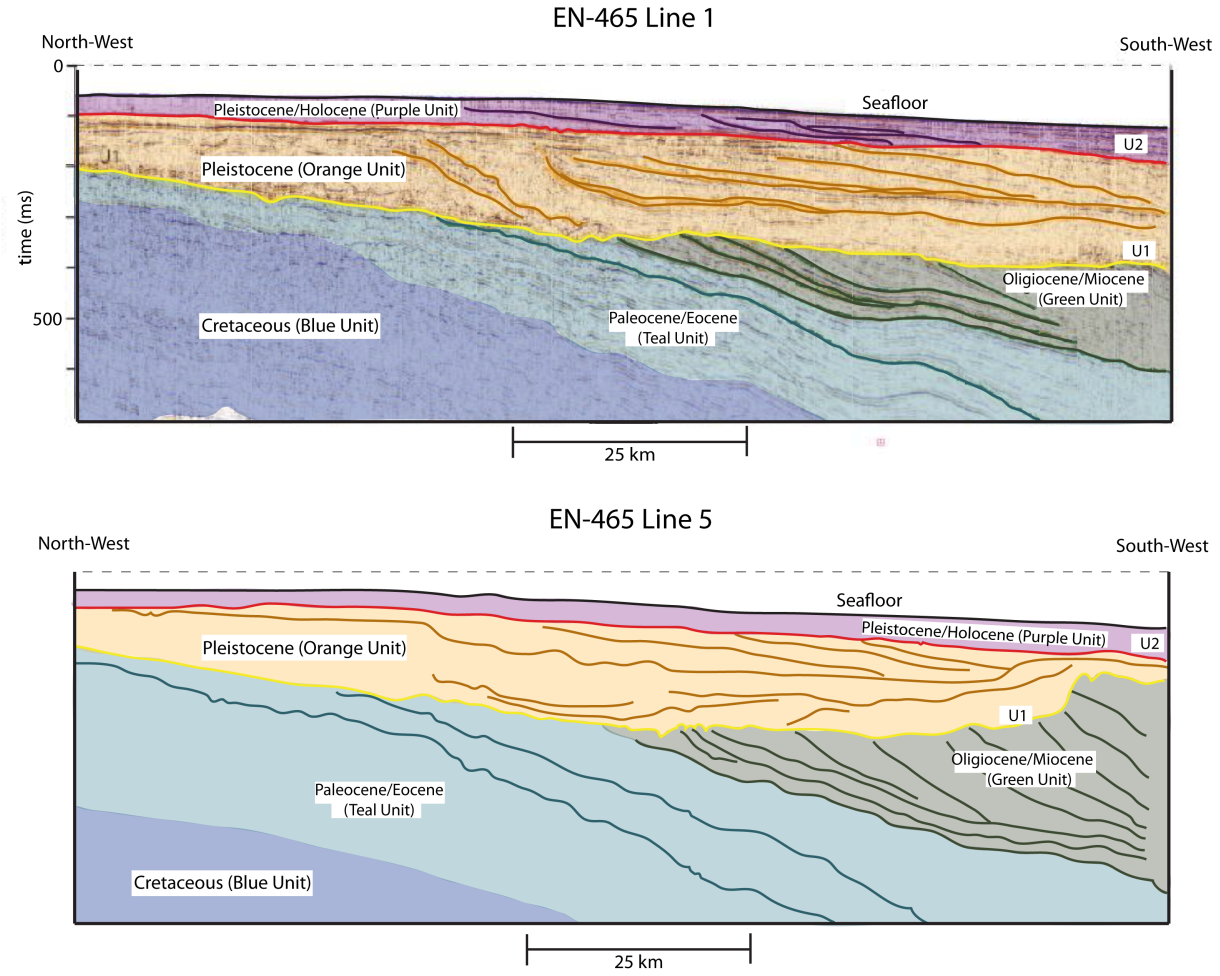

Figure 1.6: Two shore-normal profiles from high resolution multi-channel survey of the continental shelf. EN-465 Line 1 and Line 5 seismic reflectors collected offshore of Martha's Vineyard Island, Massachusetts as part of this study. Sedimentary packages have been divided into 5 units; purple, orange, green, teal, and blue. U1 (red line) and U2 (yellow line) represent large erosional events. Back dipping reflectors in the Orange Unit and on the right side of the Line 5 sit above a large erosional feature that was significant enough to change the direction of sediment deposition. This deep erosional cut may have been caused by the Laurentide Ice Sheet during a pre-Wisconsin glaciation. Line 5 is parallel and to the north of Line 1.

offshore Martha's Vineyard Island, during at least one glacial episode prior to the Wisconsin Glaciation (Figure 1.1).

The purpose of our study was to better understand the mechanisms controlling pore pressure, salinity, isotope ($\delta^{18}O$), and groundwater age distribution on the continental shelf. We addressed these issues by constructing two-dimensional finite-element models using newly acquired seismic data taken offshore of Martha's Vineyard Island (Figure 1.6). We used basic principles of seismic stratigraphy analysis to develop an improved representation of the continental-shelf hydro-stratigraphy. Our model was dynamic, in that it includes sediment deposition, erosion, and subsidence starting 2.75 Ma.

Several specific questions were addressed as part of this study: (1) What fluid flow driving forces are most important and when? Does compaction-driven flow (Bethke, 1986), density instabilities (free convection) (Kooi and Groen, 2003), or topography driven flow (forced convection) dominate (Person et al., 2003)? (2) Does the presence of the ice sheet have a significant effect on simulated salinity and pore pressure? (3) What effect does ice sheet maximum extent have on computed present-day salinity and pore pressure patterns? (4) How does an improved representation of deposition, erosion, and sedimentation during the evolution of the continental shelf influence simulated present-day salinity and pore pressure? (5) How sensitive are calculated present-day pore pressures and salinities to permeability magnitude and permeability distribution? (6) Are the proposed IODP boreholes likely to intersect paleo-fresh water? Observed salinity and hydraulic-head data from Martha's Vineyard Island and Nantucket Island served as ground truth for our model study. In the remainder of this paper we describe the geology, paleo-climate, and Pleistocene sea-level fluctuations. We

describe the transport processes represented in our model, and the method used to used to represent ice-sheet loading.

CHAPTER 2

SITE DESCRIPTION

Cape Cod and Martha's Vineyard Island are part of the Atlantic Coastal Plain, characterized by relatively gentle slopes (about 0.7 m/km). Glacial end moraines form the highest topographic relief at 53 m above sea-level (Klitgord et al., 1994; Oldale, 1992). This area is dominated by unconsolidated marine and glacial deposits ranging in age from Late Cretaceous to Quaternary (Folger et al., 1978; Hall et al., 1980; Hathaway et al., 1979; Kaye, 1964). Geophysical data in combination with sediment cores suggest that these sediments extend offshore, increasing in thickness and forming a wedge of sediment overlying the bedrock (Klitgord et al., 1994; Poppe and Poag, 1993). The slope of the interface between the sediments and the bedrock increases from northeast to southwest, from about 0.005 km/km to 0.013 km/km (Garrison, 1970; Klitgord et al., 1994; Uchupi and Mulligan, 2006).

Offshore New Jersey and Martha's Vineyard Island, Atlantic continental shelf sediments are composed of a sequence of clinoforms (Figure 1.6) (Garrison, 1970; Metzger et al., 2000; Pirmez et al., 1998), prograding stratigraphic sequences that are assumed to document the position of paleo-shorelines (Fulthorpe and Austin, 2008; Gale et al., 2002; Haq et al., 1987). The shoreline is marked by a transition between coarse and fine sediment. Sea-level fluctuations over geologic time resulted in alternating sand and clay with depth (Christie-Blick, 1991; Metzger et al., 2000).

Global eustatic sea-level during the Wisconsin glaciation (about 20 ka) is estimated to have been 120 m below modern sea-level (Figure 2.1) (Peltier, 1998). Cores taken from Nantucket Sound, Barnstable Marsh, Vineyard Sound, and Buzzard Bay indicate that sea-level at Martha's Vineyard Island could have been -12 m below modern sea-level at 4.5 ka, -16.5 m at 7.6 ka, and -57 m at 14.2 ka (Gutierrez et al., 2003; Oldale and O'Hara, 1980; Redfield and Rubin, 1962). Global sea-levels were about -8 m below modern sea-level at 4.5 ka, -16 m at 7.6 ka, and -92 m at 14.2 ka (Siddall et al., 2003). The disparity between the local (area around Martha's Vineyard) and global sea-level records is due to local disequilibrium between deposition and subsidence rates (Fulthorpe and Austin, 2008) and lithostatic flexure caused by the load of the Laurentide Ice Sheet.

Large expanses of North America are currently still rebounding from the Wisconsin glaciation (Peltier, 1998). Hudson Bay area is currently experiencing postglacial rebound, resulting in a local decrease in sea-level by 1.2 cm/yr (Peltier, 1998). Massachusetts is currently experiencing relative sea-level rise of 0.2 cm/yr due to crustal collapse of the glacial forebulge (Uchupi et al., 1996). At about 16 - 14 ka, southern Maine and northeastern Massachusetts were inundated by the sea due to ice sheet retreat and slow recovery of the lithosphere (Barnhardt et al., 1995; Uchupi et al., 1996).

Starting about 2.7 Ma - 3.0 Ma (the beginning of the Pleistocene), temperature ranges increased compared to temperature ranges during the pre-Pleistocene. Climatic cycles during the Pleistocene initially had a period of about 41 ky, increasing to a period of 100 ky between 900 - 700 ka (Raymo and Huybers, 2008). Starting around 2.6 Ma the Laurentide ice sheet advanced and covered large expanses of North America, extending down to Long Island, New York and the

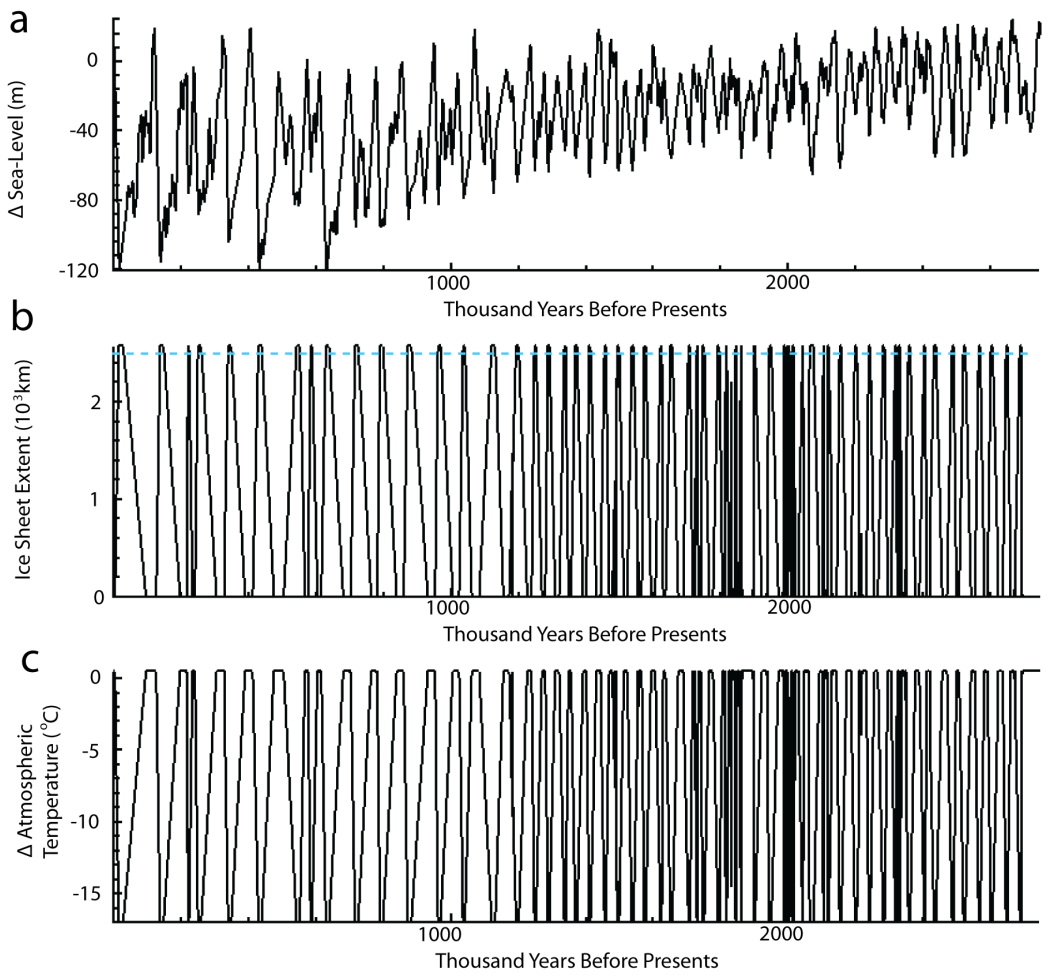

Figure 2.1: Temporal variations in a.) sea-level (Miller et al., 2005), b.) ice sheet extent, and c.) temperature evolution from 2.75 *Ma* to 0 *Ma* used in our model. We adjusted Δ temperature by adding modern land surface temperature (13^oC) over Martha's Vineyard Island. In b.) the line only represents the curves used to implement ice sheet extent to Martha's Vineyard Island. The ice sheet length (presented in Figure 2.1) is measured from the southern part of Hudson Bay (Hughes et al., 1981). When the ice sheet extent is greater than the light-blue dashed line then the ice sheet was on the continental shelf.

northern part of New Jersey along the North American East Coast (Balco and Rovey, 2010; Gustavson, 1976).

According to the recent cosmogenic-nuclide (^{10}Be and ^{26}Al) data from end moraines, the most recent glacial advance of the Laurentide ice sheet reached its maximum at Martha's Vineyard Island 23.5 *ka* (Balco et al., 2002). The margin of the ice sheet likely started advancing across New England between 31 and 27 *ka*, reaching its maximum extent on Martha's Vineyard Island between 25 and 23 *ka*. The ice sheet then started to retreat at 18.8 *ka* (Dyke et al., 2002; Oldale, 1992), indicating that the Laurentide ice sheet was likely out on the continental shelf for about 10-15 *ky*. Prior to 18 *ka*, a proglacial lake formed over what is now Nantucket Sound (Masterson et al., 1997; Uchupi et al., 1996). Tills and paleosols from Kansas, Nebraska, Missouri, and Iowa suggest that there were at least seven pre-Wisconsin advances of the Laurentide Ice Sheet that reached a position further south in the mid-continent than it did during the Wisconsin glacial stage (Roy et al., 2004). The Laurentide Ice Sheet reached a similar southern extent (around 39 ^{o} *N*) in Missouri during the Early Pleistocene (around 2.4 Ma) (Balco and Rovey, 2010).

Prior to this study, the furthest extent of the of the Laurentide Ice Sheet offshore of Massachusetts was thought to be to Martha's Vineyard Island during the Wisconsin glaciation (around 20 *ka*). To the North, near George's Bank, the ice sheet is assumed to have extended further past the modern shoreline, likely coming very close to the continental slope, due to the presence of thick gravels found in sediment cores (Hughes et al., 1981; Schlee and Pratt, 1970). However, our new geophysical data suggests that the ice sheet may have extended near to the continental shelf-slope break offshore of Martha's Vineyard Island during

pre-Wisconsin glaciations. The geophysical data shows backward dipping reflectors (thought to indicate glacial erosion) that are very similar to what is observed on Greenland's southeastern continental shelf (Figure 1.6) (Larsen et al., 1998).

CHAPTER 3

METHODS

3.1 Introduction

In order to characterize New England's present-day and paleo-hydrology, and to address the questions described in Chapter 1, we sequentially solved a suite of transport equations that represent two-dimensional, transient, variable-density groundwater flow, heat, and solute transport. These systems of equations were solved using the classical finite-element method in a model called RIFT2D. The fluid flow, heat, and solute transport equations were coupled using equations of state for viscosity and fluid density.

RIFT2D has been used by many prior studies and represents a powerful tool to estimate past groundwater flow conditions in basins (Mailloux et al., 1999; Person et al., 2003; Person et al., 1996; Wieck et al., 1995). This code was modified as part of this study to include the effects of lithospheric flexure, and stable isotope ($\delta^{18}O$) and groundwater age transport. Mathematical models, such as RIFT2D, can represent processes that change slowly over tens of thousands of years and can be compared to present-day pressure and geochemical tracer data. The drawback of these models is that paleo-boundary conditions and model parameters are poorly known and some uncertainty exists in simulation results.

3.2 Model Domain

The cross-sectional hydrogeologic model was used to simulate the paleohydrology of the Atlantic continental shelf along a shore-normal transect that extends from Cape Cod, through Martha's Vineyard Island, and 250 *km* offshore (just before the shelf break in a NW-SE direction; Figure 3.1). Simulated hydrostratigraphy incorporated geophysical data (Klitgord et al., 1994), and nearby core data (AMCOR and COST boreholes, Figure 1.1) (Folger et al., 1978; Hall et al., 1980; Hathaway, 1981; Hathaway et al., 1979; Poppe and Poag, 1993). Biostratigraphy data from Georges Bank (Cost-G1 and Cost-G2; Figure 1.1) provided approximate transition zones between fine (clay) and coarse (sand) sediment in sediment deposited before the Late Mesozoic (Poppe and Poag, 1993). However, due to the dearth of offshore core data stratigraphic sequences and associated sediments deposited before the Late Mesozoic times were highly idealized. Late Mesozoic to Quaternary stratigraphy geometry was taken directly from EN-465 Line 1 (Figure 1.6). Again, the paucity of sediment data made it difficult to correlate the seismic reflectors with stratigraphic sequences. Due to the uncertainty of sediment distribution in the stratigraphic sequences we considered different sedimentary realizations within the Pleistocene-Holocene stratigraphy in an attempt to quantify our uncertainty (this is discussed more in Section 3.17).

Our finite element grid evolved through time in order to represent glaciofluvial sedimentation and erosion during the Pleistocene (Figure 3.1). The evolving stratigraphy is described in further detail in Section 3.15. Evolution, in particular the change in surface topography and elevation, of the area that now contains Cape Cod and Martha's Vineyard Island is presented in Figure 3.2.

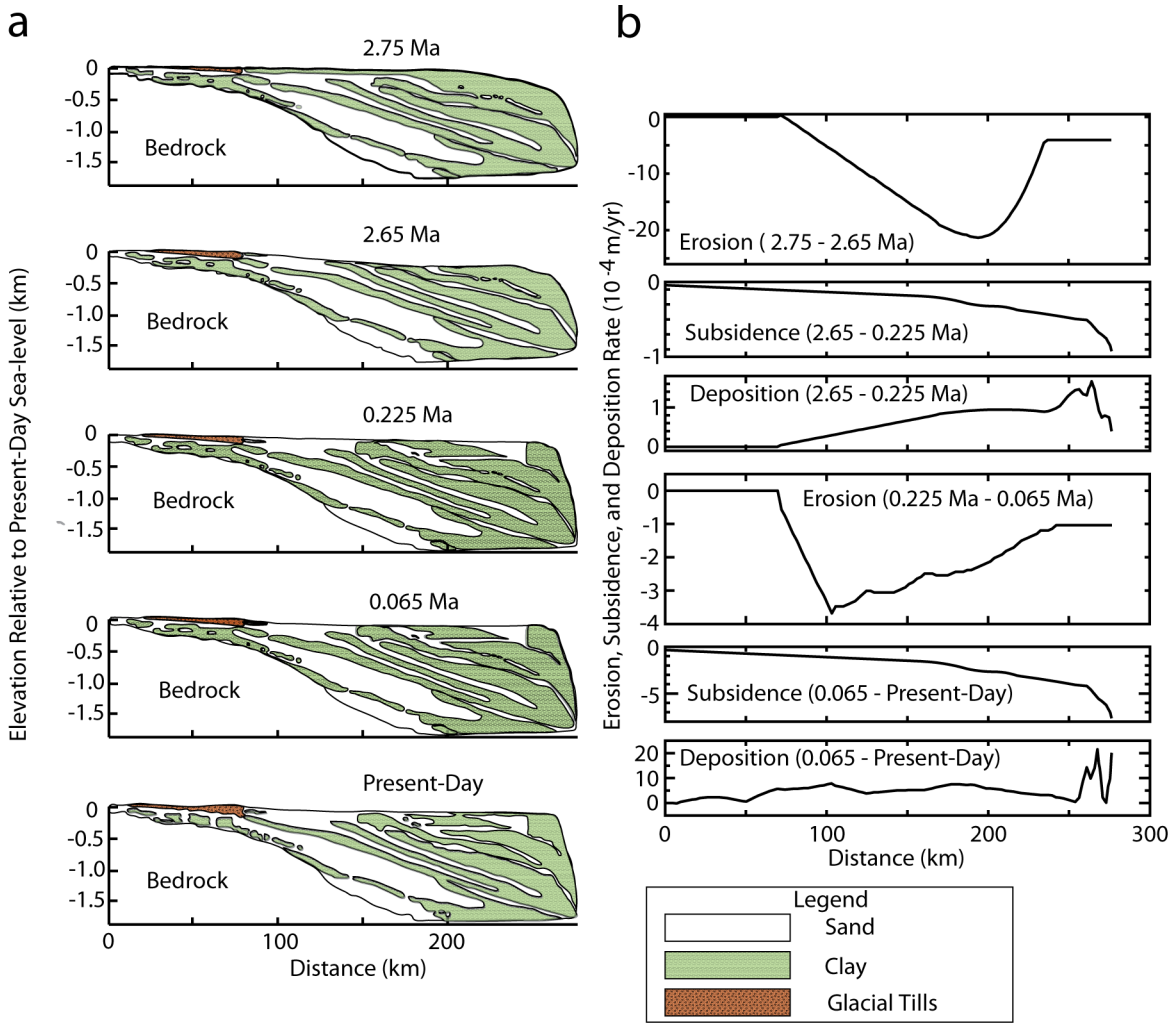

Figure 3.1: Implemented stratigraphic evolution of the continental shelf offshore Martha's Vineyard Island over the past 2.75 My. a.) stratigraphy at 4 important transitional points in our simulation. b.) the subsidence, deposition, and erosion rates between the time periods in a.) Elevation is relative to modern sea-level.

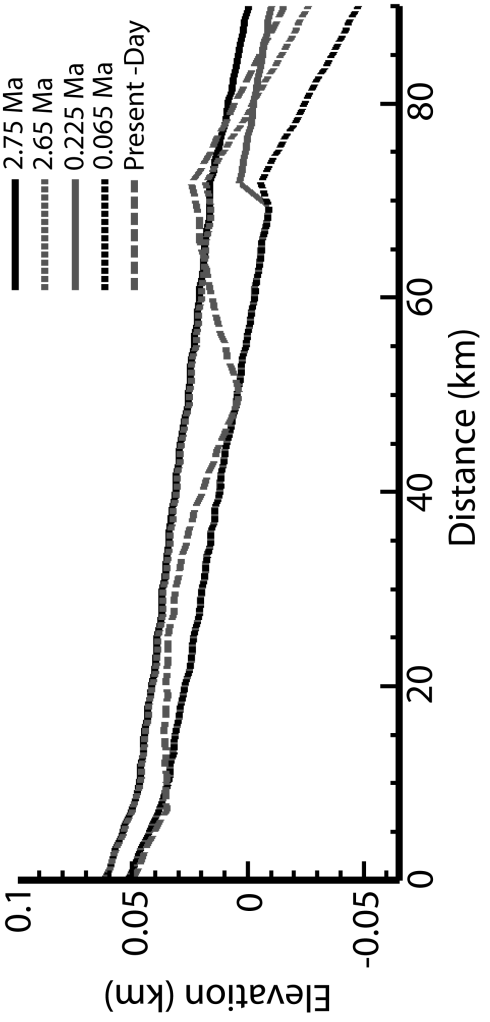

Figure 3.2: Topographic evolution in the area that presently includes Cape Cod and Martha's Vineyard Island. These elevations are relative to modern sea-level.

We used three-node triangular elements and linear trial solutions to approximate unknown nodal heads, temperature, concentrations, stable isotope composition, and groundwater age. At the start of all our simulations with evolving stratigraphy, 20342 elements and 10457 nodes were used to discretize Precambrian bedrock (not shown) and Cretaceous to Pliocene deposits. During the simulations, top surface elements and nodes were removed to represent erosion and were added to represent sedimentation. At the end of the simulated 2.75 *My*, the grid contained 25900 elements and 13249 nodes. The added elements and nodes represented Pleistocene and Holocene sediments. All our simulations started at 2.75 *Ma* and ended at present-day. All simulations had a time step size of 100 *years*. Since the focus of the IODP drilling was on continental-shelf sediments (Cretaceous to Holocene), we do not show the bedrock hydro-stratigraphy in our results. All elevations used in this study are relative to modern sea-level.

3.3 Groundwater Flow

We solved for variable-density groundwater flow using the following transport equation,

$$\nabla \cdot [\mu_r \rho_f \mathbf{K} \nabla (h + \rho_r z)] = S_s \rho_o [\frac{\partial h}{\partial t} - \frac{\partial \eta}{\partial t} \frac{\rho_i}{\rho_w} - \frac{\rho_{sw}}{\rho_f} \frac{\partial sl}{\partial t} - \frac{\rho_s - \rho_f}{\rho_f} \frac{\partial L}{\partial t}] \tag{3.1}$$

where ∇ is the gradient operator, $\mathbf{K}$ is the hydraulic conductivity tensor, h is the hydraulic head, ρ_o is the water density at standard conditions ($10^o C$, 0.0ppt salinity, and 0.0 MPa), ρ_r is the relative density, μ_r is the relative water viscosity, S_s is the specific storage, ρ_f is the density of groundwater, t is time, η is the elevation of the ice sheet, ρ_s is the density of the solid phase, ρ_w is the density of water, ρ_i

is the density of ice, ρ_{sw} is the density of seawater, sl is sealevel, and L is the sediment water interface elevation. Using the term $\rho_r z$ allowed us to take into account flow induced by density instabilities (more dense water over less dense water).

Equation 3.1 is a variation of the groundwater flow equation presented in Garven and Freeze (1984), except in addition to temporal changes in temperature we take into account loading due to the ice sheet, sea level, and sedimentation. The first term on the right-hand side of Equation 3.1 accounts of changes in storage due to temporal variations in hydraulic head. The second and third terms on the right-hand side of Equation 3.1 accounts for ice-sheet loading and seawater loading, respectively. Sediment loading is represented by the fourth term on the right-hand side of Equation 3.1. These terms are required because changes in sea-level and ice sheet thickness induces a change in vertical stress which is felt instantaneously at depth. We assume a loading efficiency of one. This may overestimate pore pressures induced due to ice-sheet or sediment loading at depths less than 300 m. Freshwater hydraulic head in Equation 3.1 is given by

$$h = \frac{P}{\rho_o g} + z \tag{3.2}$$

where P is fluid pressure, g is gravitational acceleration, and z is elevation above the reference datum (Hubbert, 1940). We also corrected for hydraulic head changes due to subsidence and flexure, which caused elevation change.

We used the following equation for the variable-density form of Darcy's Law in our model (Garven and Freeze, 1984):

$$\vec{q} = -\mathbf{K}\mu_r \nabla(h + \rho_r z) \tag{3.3}$$

Relative density (ρ_r) and viscosity (μ_r) used in Equation 3.1 and 3.3 are given by

$$\rho_r = \frac{\rho_f - \rho_o}{\rho_o} \tag{3.4}$$

$$\mu_r = \frac{\mu_o}{\mu_f} \tag{3.5}$$

where μ_o is the viscosity of water at standard conditions (10^oC, 0.0 ppt salinity, and 0.0 MPa) and μ_f is the viscosity of water. μ_f and ρ_f are dependent on temperature and concentration.

The principal components of the hydraulic conductivity tensor **K** are parallel and normal to the geologic units. Components K_{xx}, K_{zz}, K_{zx}, and K_{xz} are calculated using

$$\begin{aligned} K_{xx} &= K_{max} \\ K_{zz} &= K_{min} \\ K_{xz} &= K_{zx} = 0 \end{aligned} \tag{3.6}$$

where K_{max} is the maximum component of permeability and K_{min} is the minimum component of permeability.

3.4 Solute Transport

Transport of solute through porous media is controlled by advection, Fickian diffusion, and hydrodynamic dispersion (Freeze and Cherry, 1979). For relatively low pore velocities ($< 10^{-5}$ m/yr), solute transport is dominated by diffusion; dispersive and advective transport are more important when fluid velocities

are higher. We used the following equation to represent advective/dispersive solute transport (Konikow and Grove, 1977),

$$\nabla \cdot [\mathbf{D}\nabla C] - \vec{v} \cdot \nabla C - C(\nabla \cdot \vec{v}) = \frac{\partial C}{\partial t} \tag{3.7}$$

where $\mathbf{D}$ is the hydraulic dispersion-diffusion tensor, $\vec{v}$ is the groundwater velocity ($\vec{v} = \vec{q}/\phi$), ϕ is porosity, and C is species concentration total dissolved solids reported as solute mass fraction (kilograms of solute per kilograms of solution). We converted mass fraction to ppt (parts per thousand solute) for use in our study.

Equation 3.7 neglects the effects of solute diffusion into low permeability blocks and rapid advection through fractures (i.e. double porosity effects) (Feehley et al., 2000). It also neglects the effects of sources/sinks, such as fluid-rock geochemical reactions (Provost et al., 1998). The tensor $\mathbf{D}$ has the four components, D_{xx}, D_{zz}, D_{zx}, and D_{xz}, defined by

$$\begin{aligned} D_{xx} &= \frac{v_x^2}{|\vec{v}|}\alpha_L + \frac{v_z^2}{|\vec{v}|}\alpha_T + D_d \\ D_{zz} &= \frac{v_z^2}{|\vec{v}|}\alpha_L + \frac{v_x^2}{|\vec{v}|}\alpha_T + D_d \\ D_{xz} = D_{zx} &= (\alpha_L - \alpha_T)\frac{v_x v_z}{|\vec{v}|} \end{aligned} \tag{3.8}$$

where v_x and v_z are components of seepage velocity in the $x-$ and $z-$directions ($v_x = q_x/\phi$ and $v_z = q_z/\phi$), D_d is the diffusion coefficient, α_L is the longitudinal dispersivity, α_T is the transverse dispersivity, and $|\vec{v}| = \sqrt{v_x^2 + v_z^2}$.

3.5 ^{18}O Transport

Water-rock oxygen isotope exchange reactions can generally be neglected when temperatures are less than 100^oC (Bowman et al., 1994). This was the case for our hydrologic models of New England; temperatures at the base of our model never exceeded 90^oC. We used ^{18}O transport equations homologous to Equations (3.7)-(3.9);

$$\nabla \cdot [\mathbf{D} \nabla R_f] - \vec{v} \cdot \nabla R_f = \frac{\partial R_f}{\partial t} \tag{3.9}$$

where R_f is the fluid $^{18}O/^{16}O$ ratio. In systems that the dominant constituent (solute) contains the dominant isotope (^{16}O) then the mole fraction of ^{16}O approaches unity. Thus conservation of R_f can be considered conservation of ^{18}O (Criss et al., 1987).

3.6 Heat Transport

Temperature can affect fluid density (Garven and Freeze, 1984) and permafrost in our model (Bense and Person, 2008). We used a conductive heat-transfer equation:

$$[c_f \rho_f \phi + c_s \rho_s (1 - \phi)] \frac{\partial T}{\partial t} = \nabla \cdot [\lambda_f^{\phi} \lambda_s^{1-\phi} \nabla T] \tag{3.10}$$

where λ_f is the thermal conductivity of the fluid phase, λ_s is the thermal conductivities of the solid phases, ϕ is porosity, T is temperature, c_s and c_f are the specific heat capacities of the solid and liquid phases, respectively, and ρ_s is the density of the solid phase. Equation 3.10 accounts for heat capacity of the water and

the solid phase and neglects thermal source/sinks (i.e. latent heat of freezing) associated with freezing/thawing of permafrost. Convective heat transfer was neglected because the systems we considered here did not produce high vertical velocities over a significant fraction of the sedimentary pile. Studies that have included the effects of freezing/thawing require very fine temporal and vertical grid discretization that preclude long (paleo-hydrology) simulations (McKenzie et al., 2007). Bense and Person (2008) found that the latent heat of melting would delay permafrost thawing for no longer than a few thousand years (Bense and Person, 2008). On the time scale of a glacial cycle (41-100 ky) the effects of neglecting this should be small. We adopt a simplified approach where by we lower the hydraulic conductivity of the porous media by two orders of magnitude if the temperature drops below the pressure melting temperature. A similar approach was used by Cohen et al. (2010).

3.7 Groundwater Residence Time

We calculated groundwater age using a numerical method similar to the method used for salinity (Section 3.4) and $\delta^{18}O$ (Section 3.5) (Goode, 1996):

$$\nabla \cdot [\mathbf{D}\nabla A] - \vec{v} \cdot \nabla A + 1 = \frac{\partial A}{\partial t} \tag{3.11}$$

where $\mathbf{D}$ is the hydraulic dispersion-diffusion tensor, $\vec{v}$ is the groundwater velocity ($\vec{v} = \vec{q}/\phi$), ϕ is porosity, and A is the groundwater age. In Equation 3.11, transport of groundwater age is homologous to transport of a solute: in particular groundwater age can be advected, diffused, dispersed, and mixed with water with different groundwater ages. The largest difference between Equation 3.11 and Equations 3.7 and 3.9 is the third term on the left-hand side of Equation 3.11,

which accounts for the unit increase in age with a unit time step. The age calculated using this equation represents mean age.

3.8 Equations of State

Thermodynamic equations of state are used to compute the density and viscosity of groundwater at elevated temperature, pressure, and salinity conditions. RIFT2D uses the polynomial expressions from Kestin et al. (1981):

$$\frac{1}{\rho_f} = a(T) + b(T)P + c(T)P^2 + Cd(T) + C^2e(T) - PCf(T) - C^2Pg(T) - \frac{h(T)}{2}P^2 \tag{3.12}$$

$$\mu_f = \mu_o[1 + B(T,C)P] \tag{3.13}$$

where C is the solute concentration, T is temperature, P is pressure, and $a(T)$,$b(T)$,...$h(T)$, and $B(T,C)$ are $3^{rd}-$ and $4^{th}-$ order temperature- and concentration-dependent polynomials (Kestin et al., 1981). These polynomial expressions are valid for temperatures between 10 to 150^oC and salinities between 0 and 6m NaCl. Fluid density is more sensitive to temperature and salinity than fluid pressure. Below 10^oC, we set viscosity and fluid density to standard state conditions (10^oC, 0.0ppt salinity, and 0.0 MPa).

3.9 Sea-Level and Ice Sheet Evolution

In our analysis we did not solve for the ice-sheet dynamics, as has been done recently (Flowers et al., 2005; Le Brocq et al., 2009). Rather we imposed ice sheet position and thickness using polynomial functions. Changes in the position and thickness of the ice sheet are tied to marine isotope records, which provide a

measure of continental ice storage. By knowing the approximate size, elevation, and maximum lateral extent of the Laurentide ice sheet relative to our model coordinates, we were able to reconstruct ice loading by altering the top boundary conditions, in particular hydraulic head, temperature, salinity, and $\delta^{18}O$, as well as appropriately altering the elevation of portions of our mesh affected by lithospheric flexure due to ice-sheet loading. Exactly how the boundary conditions were changed will be discussed in later sections. Though, it is important to know that the boundary conditions of salinity, $\delta^{18}O$, and groundwater age were adjusted to a zero gradient boundary condition for areas experiencing groundwater discharge.

We approximated sea level during the Pleistocene (2.75 *Ma*) by using fluctuations in $\delta^{18}O$ data derived from foraminifera (Figure 2.1) (Bintanja et al., 2005; Dutton et al., 2009; Kawamura et al., 2007; Miller et al., 2005; Raymo et al., 2006; Raymo and Huybers, 2008; Siddall et al., 2003; Sosdian and Rosenthal, 2009). $\delta^{18}O$ data from marine foraminifera suggest substantial eustatic sea-level changes over the last glacial cycle and similar changes throughout the Pleistocene (Bintanja et al., 2005; Miller et al., 2005). Presumably these sea-level changes are due changes in continental ice storage.

We estimated the timing of Laurentide Ice Sheet advances and retreats by assuming the ice sheet was absent (sea-levels highstands) when the marine carbonate $\delta^{18}O$ was depleted ($\delta^{18}O < 0.3$ ‰) and the ice sheet was at its maximum size (sea-levels low-stands) when the marine carbonate $\delta^{18}O$ was enriched ($\delta^{18}O > 0.3$ ‰; Figure 2.1). Taking into account a shift between 41 *ky* and 100 *ky* glacial cycle at 900 *ka*, there were potentially 60 glacial stages since 3 *Ma* (Raymo and Huybers, 2008). We allowed the Laurentide Ice Sheet to wax and wane using

simple linear equations (Figure 2.1). The rate of ice sheet advance and sea-level decline was always slower than ice sheet retreat and sea-level rise. As shown in Figure 2.1 we assumed that the ice sheet maximum extent was the same for all glacial periods, but not necessarily the same for the last glacial period (Wisconsin) in which the ice sheet only extended to Martha's Vineyard Island. Since the Laurentide Ice Sheet may have reached the continental slope, we tested two different scenarios of ice sheet maximum extent (Figures 3.3 and 3.4). In one case the ice sheet had a maximum thickness of 1.4 *km* at Cape Cod and extends to the continental shelf-slope break (about 250 *km* south-east of Cape Cod) during all pre-Wisconsin glaciations. In the other scenario, the ice sheet's maximum thickness was 1.1 *km* at Cape Cod and maximum extent was only to Martha's Vineyard Island (about 80 *km* south-east of the most western portion of our model domain) for every glacial period throughout the Pleistocene (See Figure 3.4).

We approximated ice sheet thickness (H) using a polynomial similar to one presented by Vialov (1958) (Figure 3.4),

$$H(x) = H_t \sqrt{|1.0 - (x/L_t)^2)|} \tag{3.14}$$

where H_t is the thickness of the ice sheet at the summit, L_t is extent of the ice sheet from its center in Hudson Bay and Northern Manitoba, and x is the distance from the summit (center) of the ice sheet (Vialov, 1958). The load due to the ice sheet (η) is then,

$$\eta(x) = 0.9H(x). \tag{3.15}$$

Only about 90 % of the ice sheet thickness contributed to hydraulic head (This is explained in Section 3.10).

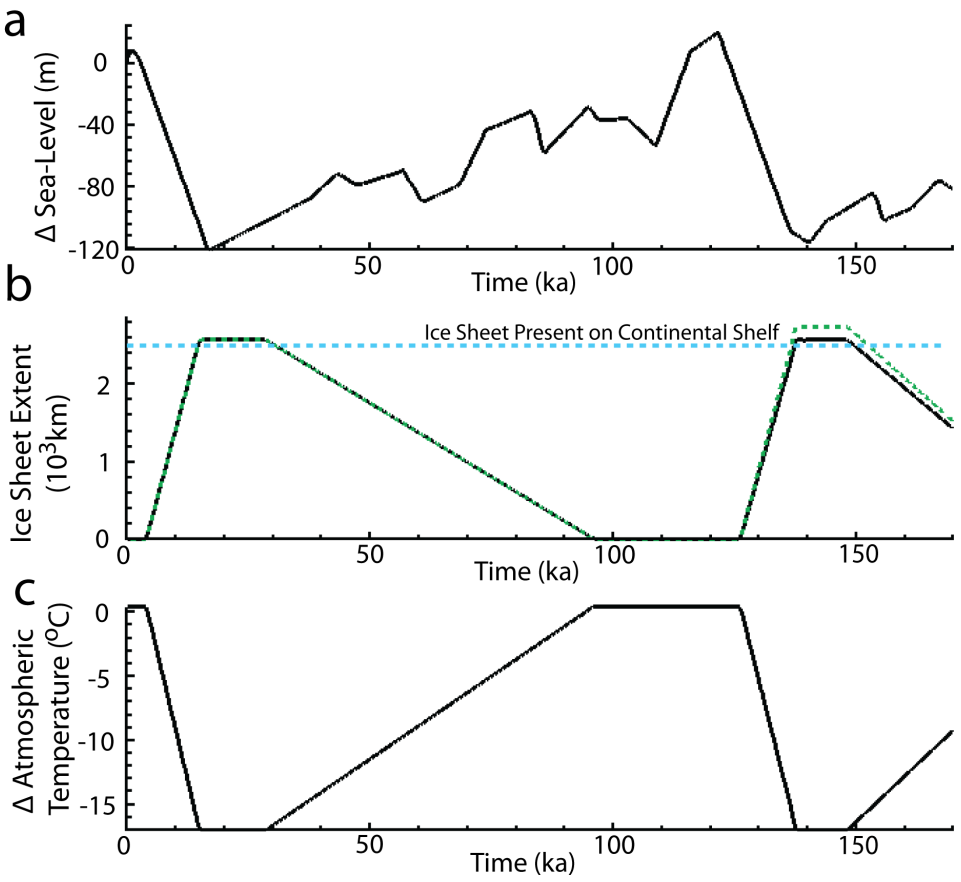

Figure 3.3: Temporal variations in a.) sea-level (Miller et al., 2005), b.) ice sheet extent from the center of the ice sheet (southern part of Hudson Bay) (Hughes et al., 1981). , and c.) temperature evolution since 170 ka used in our model. We used a modern land surface temperature of 13^oC over Martha's Vineyard Island (Gustavson, 1976). In b.) the green dashed line represents the imposed ice sheet extent scenarios used in which the ice sheet came out almost to the shelf-slope break (250 km in our model domain) during pre-Wisconsin glaciations and the black line represents the imposed ice sheet extent scenarios in which the ice sheet just came out to Martha's Vineyard Island for all Pleistocene glaciations. For both scenarios, the ice sheet extended to Martha's Vineyard for the Wisconsin glaciation (most recent glaciation). For extents greater than the blue dashed line, the ice sheet was on the continental shelf.

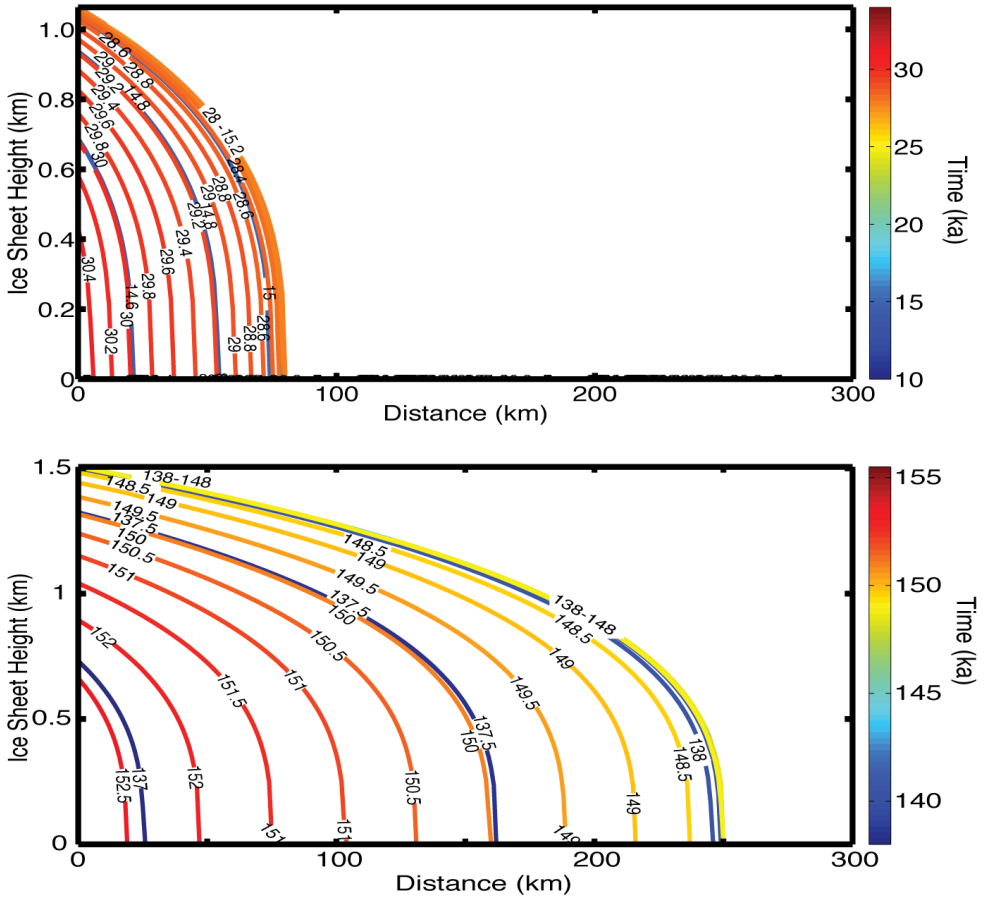

Figure 3.4: Two scenarios of the evolution of the ice sheet on the continental shelf (starting on the eastern side of Cape Cod) during the last two glacial cycle. Top: ice sheet extends to Martha's Vineyard Island during the Wisconsin glaciation. Bottom: ice sheet extends near the continental shelf-slope break (250 km) during the Illinoian glaciation. Note, the x-distance is relative to the furthest eastern portion of our model domain, which is near Cape Cod.

We used Equation 3.15 to represent the mechanical load of the entire Laurentide Ice Sheet into Canada, in order to calculate flexural adjustments to the lithosphere. Flexural adjustments to the land surface elevation decreased the imposed elevations heads by as much as 400 m to 500 m (about 33 - 36 % of the ice sheet thickness) along the left side of our mesh.

3.10 Boundary Conditions for Groundwater Flow

The sides and bottom of the model domain were prescribed no-flow boundaries. A specified hydraulic head was imposed along the top boundary. It is important to note that the continental shelf-slope break is considered as part of the top boundary, thus having prescribed head boundary. Top nodes below sea level were given a freshwater hydraulic head equal to sea-level elevation corrected for the density of seawater ($head = sl * 1.025/1.0$). Figure 2.1 contains the sea level curve used in all simulations. In areas overrun by the ice sheet, we increased hydraulic head by adding 90% of the ice sheet thickness to the rock surface elevation. This assumes that the Laurentide Ice Sheet had liquid water present at its base and that basal and surface meltwater generation rates were high enough to keep fluid pressures at or near floating conditions. This assumption is supported by paleo-pore pressure reconstruction from under consolidated tills from the Des Moines Lobe in Iowa (Hooyer and Iverson, 2002), as well as modern fluid pressure measurements beneath modern ice streams in Antarctica (Engelhardt and Kamb, 1997). As discussed below (Section 3.11), this condition is modified when permafrost is present. Subaerial top nodes not covered by the ice sheet were assigned heads equal to the land surface elevation.

3.11 Thermal Boundary Conditions and Initial Conditions

For heat transfer we assumed insulated side boundary conditions and an initial linear increase in temperature with depth ($30^oC/km$). At the base of the model we imposed a basal heat flux of 0.06 W/m^2, which is typical for the continental crust. At the top boundary condition of the domain we set prescribed temperatures, dependent on the location of top nodes relative to the ice sheet and the shore line. A temperature of 4^oC was specified for all surface nodes below sea-level. Surface nodes exposed to the air were set to the atmospheric temperature. We approximated atmospheric paleo-temperature changes using Pleistocene marine foraminifera $\delta^{18}O$ records (Bintanja et al., 2005). The average atmospheric temperature (2001-2010) in Martha's Vineyard Island is 13^oC, similar to average temperatures in New England (12.5^oC) (Gustavson, 1976). During the last glacial maximum, isotopic records suggest that temperatures decreased by 17^oC (Figure 2.1) (Bintanja et al., 2005).

Depending on the location of the boundary node, if basal ice-sheet temperatures or atmospheric temperatures were less than the pressure melting point, we decreased the permeability of its respective triangular element by two orders of magnitude to represent the effects of permafrost formation. Top boundary nodes under the ice sheet were assigned a temperature calculated using an analytical solution for vertical advective-conductive heat transport through the ice sheet (See Section 3.12).

3.12 Ice Sheet Basal Temperature Boundary Condition: Analytical Solution

Temperatures within an ice sheet are controlled by both conduction and advection of heat (Hooke, 1998). We used the following analytical solution to

the one-dimensional vertical, steady-state, advective-conductive heat transport equation (Hooke, 1998),

$$T_i(z_i) = T_s - \frac{\sqrt{\pi}}{2}\frac{\beta_o}{\zeta}[erfi(\zeta H) - erfi(\zeta z_i)] \tag{3.16}$$

$$\zeta = \sqrt{\frac{w}{2\kappa H}} \tag{3.17}$$

$$erfi(r) = \frac{1}{\sqrt{2\pi}}\int_0^r e^{\frac{s^2}{2}}ds \tag{3.18}$$

$$w = -b_n \tag{3.19}$$

where z_i is the elevation above the base of the ice sheet, T_i is the temperature within the ice sheet at z_i, T_s is the surface temperature of the ice sheet, β_o is the basal temperature gradient, H is the thickness of the ice sheet, κ is the ice thermal diffusivity, w is the vertical ice velocity at the ice surface, b_n is the net accumulation rate, and $erfi(r)$ is the *imaginary error function*. This analytical solution is intended for only positive vertical advection (negative net accumulation), thus is used for the ablation zone. Due to our location near the edge of the ice sheet, the portion of the ice sheet over our study area is assumed to always be in the ablation zone.

We set T_s, the temperature at the top of the ice sheet, equal to the air temperature. Instances where the calculated basal temperature was higher than the pressure melting temperature (T_{pmp}) we set basal temperatures to T_{pmp},

$$T_{pmp} = T_{TP} - c_i\rho_i g H \tag{3.20}$$

where T_{TP} is the triple point temperature, c_i is the depression of the melting point of water with increased pressure, ρ_i is the density of ice, g is gravity, and H is the thickness of the ice sheet.

We approximated net snow accumulation rate (b_n) at the ice sheet summit (over Hudson Bay and Northern Manitoba) by assuming a linearly temperature dependent accumulation rate (Cuffey and Clow, 1997), based on data presented by Cuffey and Clow (1997),

$$b_n = 0.00213T_s + 0.1212 \tag{3.21}$$

Then, we calculated b_n across the ice sheet by having b_n decrease linearly down the ice sheet, crossing zero midway down; the transition point between the accumulation and ablation zone occurred at the point along the ice sheet in which the thickness of the ice was half the thickness of the ice sheet at the summit. The accumulation rate, b_n is negative in the ablation zone of the ice sheet, where the ice is sublimating and melting. Permafrost occurs where the mesh surface temperature is less than the pressure melting temperature (T_{pmp}; Equation 3.20). Figure 3.5 illustrates how the top temperature boundary condition may appear during a glacial period.

3.13 Groundwater Age Boundary and Initial Conditions

We specified the age of the top boundary to 0 years; we altered this condition to a zero gradient boundary in areas experiencing groundwater discharge. The initial age for the entire mesh was 0 years, allowing us to differentiate the time and frequency of infiltration during our simulation. The side and bottom boundaries were assigned as no-flux boundaries.

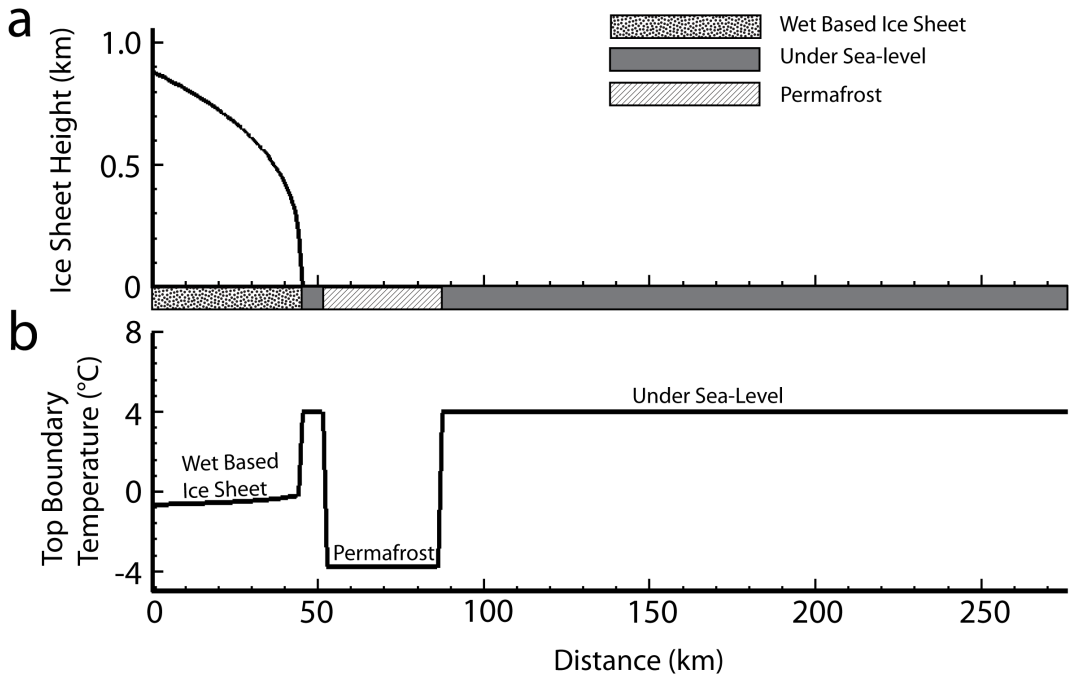

Figure 3.5: (a) Imposed ice sheet thickness during the Wisconsin glaciation as the ice sheet has started to retreat. (b) Computed surface temperatures of the mesh were dictated by atmospheric temperature, ice sheet thickness, and sea-level elevation. Permafrost is present in aerially exposed topography. When top boundary temperatures were less than the pressure melting temperature permafrost formed. The ice sheet tended to insulate the ground, preventing formation of permafrost.

3.14 Salinity and $\delta^{18}O$ Boundary and Initial Conditions

Choosing an initial salinity distribution for Pliocene-Cretaceous sediments is problematic due to the long diffusive response time of thick continental shelf sequences. Some studies have assumed a linear increase in salinity with depth (e.g. Bense and Person, 2008). We felt it was appropriate to prescribe Cretaceous-Pliocene sediments in our model using a constant value of 35 ppt (0.035 mass fraction) and 0‰ $\delta^{18}O$, equivalent to seawater compositions. The top boundary conditions for solute transport equations were a constant concentration of 0 ppt (0 g/ml NaCl) for surface nodes above sea level and beneath the ice sheet, and 35 ppt for surface nodes below sea level. The concentration of $\delta^{18}O$ of top boundary nodes was set to 0‰ $\delta^{18}O$ when below sea level, -20‰ $\delta^{18}O$ when below the ice sheet , and -10‰ $\delta^{18}O$ when subaerial. The ice sheet $\delta^{18}O$ end member boundary condition may be more enriched than actual conditions (Remenda et al., 1994). The Michigan Basin contains glacial meltwater ranging between -16‰ and -22‰ (Grasby et al., 2000; Ma et al., 2004; McIntosh and Walter, 2005). Salinity and $\delta^{18}O$ boundaries are adjusted to zero gradient for surface nodes that experience discharge.

3.15 Simulated Continental Shelf Evolution

Our model represented sedimentation, erosion, and clinoformal development over geologic time. The geometry of the deposited sedimentary packages (clinoforms) were taken directly from reflectors in our geophysical data (EN-465 Line 1; Figures 1.6 and 3.1). We assumed a lever-like subsidence where the subsidence rate increased out towards the continental-shelf break. The subsidence

rate also took into account the isostatic response due to clinoform development (McKenzie, 1978; White and McKenzie, 1988).

Most of the reflectors within Line 1 are clinoformal structures that have been partially eroded during sea-level low-stands. In order to allow our mesh to represent erosional and depositional periods we projected the clinoforms back to their pre-erosional sigmoid-oblique shapes. This portion of the clinoform package was eroded during our simulated continental-shelf evolution. The thickness of sedimentary packages were derived then from the projected clinoforms. The deposition rate was calculated by dividing the sedimentary package thickness by the duration of the depositional period. The deposition rates ranged between 0 and 0.002 m/yr (Figure 3.1). These rates are consistent with depositional rates in New Jersey (Dugan and Flemings, 2000; Steckler et al., 1999).

We prescribed depositional time periods (i.e. periods of constant specified subsidence rates) used in the Line 1 reflectors (Figure 1.6). We based the age of clinoforms in EN-465 Line 1 on similar units found off the coast of New Jersey (Fulthorpe and Austin, 2008; Metzger et al., 2000), USGS Line 5 (Klitgord et al., 1994), and wells from Georges Bank (Cost G1 and G2). Our model evolved over 2.75 My. We only represented two erosional periods in our simulations, however the seismic data indicates that there were several minor erosional periods (Figure 1.6). We felt it was appropriate to neglect these in our simulations, dominantly for the sake of simplicity.

The first erosional period took place from 2.75 Ma to 2.65 Ma (yellow line in Figure 1.6), accounting for erosion that occurred during early (maybe first) three glacial episodes when the ice sheet may have extended near its most southernly extent and the continental shelf sediments were not in equilibrium with

glacial forcings. The first three advances of the Laurentide Ice Sheet into central North America could have occurred between 2.6 and 2.4 *Ma* (Balco and Rovey, 2010), though some may argue as early as 2.7 *Ma* (Raymo and Huybers, 2008). Even though it is unimportant in our simulations when this erosional event occurred (either between 2.75 and 2.65 *Ma* or between 2.6 and 2.4 *Ma*), in either case a 100 *ky* erosional period would be appropriate for spanning over three glacial periods or three sea-level low-stands. The model built up clinoformal packages from 2.65 *Ma* to 0.225 *Ma* (orange unit in in Figure 1.6).

A second erosional period occurred 0.225 *Ma* to 0.065 *Ma* (red line in in Figure 1.6), which represented a recent erosional event that we have spanning over the Illinoian glaciation (around 155 - 135 *ka*). This erosional event may in reality represent the cumulative erosion that occurred during the 100 *ky* glacial cycles (starting around 900 *ka*), however exactly representing this would be unnecessary and would have little impact on magnitudes of sedimentation and erosion rates and our final results. Further, the exact rates and durations of sedimentation and erosion associated with the 100 *ky* glacial cycles (between 0.9 *Ma* and 0.065 *Ma*) is not known, thus using a erosional period of 160 *ky* is a good median value.

The last depositional period extended from 0.065 *Ma* to present, during which we deposited a series of prograding clinoforms (purple unit in Figure 1.6) and the glacial sediments forming Cape Cod and Marthas Vineyard. The prograding clinoforms represented sediments deposited during the most recent interglacial, deltaic progradation during sea-level fall, and flushing of glacial sediments during deglaciation in the Wisconsin. The Laurentide Ice Sheet did not extend as far south during the Wisconsin than it did during earlier glaciations

(Balco and Rovey, 2010). Thus, the erosional event during the Wisconsin sea-level low-stand may have been less significant. It is important to know that the continental shelf evolution has an insignificant impact on simulated solute patterns and that the most recent sedimentation has the greatest control on simulated present-day pore-pressure patterns.

We set the model to have a temporally varying lateral transition point between high permeability (sand) and low permeability (clay) units during sedimentation. This produced alternating clay and sand units with depth. We ran two stratigraphic alternatives: one that deposited equal distribution of sand and clay and another that deposited predominantly clay.

3.15.1 Simulating Ice Sheet Flexure Magnitude

We represent flexure of the continental shelf in response to ice-sheet loading on the North American Craton by assuming an elastic lithosphere model, where the upper lithosphere responds to a load as a beam overlying a dense and highly viscous fluid (i.e. the mantle) (Turcotte and Schubert, 1982; Watts, 2001). This approach neglects the multi-dimensional effects of a spherical earth and mantle flow. On the other hand, this approach goes beyond assuming isostatic response to ice-sheet loading (i.e. local compensation only) (Bense and Person, 2008; Le Meur and Huybrechts, 1996). We approximated the effects of transient mantle flow empirically (described later). The magnitude of flexure is a function of the density difference between the ice and the mantle, and the stiffness of the lithosphere.

We calculated flexure (w_f) using an analytical solution to the following beam flexure model (Turcotte and Schubert, 1982),

$$D\frac{d^4w_f}{dx^4} + (\rho_m - \rho_i)gw_f = 0 \tag{3.22}$$

where x is the distance away from the load, ρ_i is the density of ice, and ρ_m is the density of the mantle, and g is gravity.

Assuming the the thickness of the lithosphere is constant, we can use the solution for an infinite beam (Hetenyi, 1946). Flexural displacement (w_f) was calculated by separating portions of the ice sheet across Canada and the northern United States into columns of equal width. Each column was assigned an ice sheet height based on Equation 3.14. We determined the flexural response of the elastic lithosphere to these point loads separately and then added all the responses using superposition theory. The deflection (w_f) of a point located at a given distance from a load column can be calculated using the following analytical solution to Equation 3.22,

$$w_f = \left(\frac{\eta\rho_i}{2\rho_f}\right)\left(2 - e^{(-a/\alpha)}\cos(a/\alpha) - e^{(-b/\alpha)}\cos(b/\alpha)\right) \tag{3.23}$$

$$w_f = \left(\frac{\eta\rho_i}{2\rho_f}\right)\left(e^{(-a/\alpha)}\cos(a/\alpha) - e^{(-b/\alpha)}\cos(b/\alpha)\right) \tag{3.24}$$

$$w_f = \left(-\frac{\eta\rho_i}{2\rho_f}\right)\left(e^{(-a/\alpha)}\cos(a/\alpha) - e^{(-b/\alpha)}\cos(b/\alpha)\right) \tag{3.25}$$

where η is the thickness of ice sheet (load), $\alpha = \left[\frac{4D}{\rho_f g}\right]^{1/4}$, D is the stiffness of the lithosphere, $\rho_f = \rho_m - \rho_i$, and a and b are the distances of point x from the the left and right borders of the load column, respectively. Equation 3.23 is used for deflection of points directly under the load column, Equation 3.24 calculates the deflection of points to the left of the load column, and Equation 3.25 calculates

the deflection of points to the right of the load column. We used a stiffness (D) of $1x10^{22}\ Pa \cdot s^2 m^{-2}$, which is typical for continental crust (Turcotte and Schubert, 1982).

3.15.2 Simulating Ice Sheet Flexure Rate

Flexure of the lithosphere does not occur instantaneously, there is a lag due to the effects of viscous mantle flow. The mantle is a dense (3300 kg/m^3), highly viscous semi-fluid material that takes thousands of years to reach an equilibrium state (Peltier, 1996). The viscosity of the mantle is about $10^{21}\ Pa \cdot s$ (Peltier, 1996). This viscosity produces a 3-6 ky mantle response time (τ) to ice-sheet loading (Le Meur and Huybrechts, 1996; Peltier, 1996; Peltier, 1998). We used the following equation to approximate the timed rate of flexure:

$$\frac{dz}{dt} = \frac{z_i - (z_o - w_f)}{\tau} \tag{3.26}$$

where $\frac{dz}{dt}$ is the timed rate of change of the continental shelf elevation, z_i is the elevation of the ice sheet at the earlier timestep, z_o is the elevation without flexural load, w_f is the equilibrium flexure , and τ is the mantle response time. Equation 3.26 accounts for flexure under the load of the ice sheet and lithospheric rebound when the ice sheet is removed. We used τ equal to 3 ky; this gave a flexural response and resulting relative sea level more consistent with field observations on Martha's Vineyard Island and Nantucket (Peltier, 1998).

3.16 Porosity

Porosity is calculated using Athy's Law (Bethke and Corbet, 1988; Hubbert and Rubey, 1959):

$$\phi = \phi_o e^{-\beta \sigma_e} \tag{3.27}$$

where ϕ_o is the initial porosity at the top of the sediment column, ϕ is the porosity at the maximum effective stress, β is the bulk compressibility of the sediment, and σ_e is the effective stress. Equation 3.27 relates porosity to effective stress and compressibility. Equation 3.27 also assumes that all porosity loss can be uniquely tied to effective stress (σ_e). The equation does not take into account loss of porosity due to diagenetic effects. Using Terzaghi's principle, σ_e is calculated as follows,

$$\sigma_e = \sigma_v - P \tag{3.28}$$

where σ_v is the total vertical overburden stress and P is the hydrostaic pore pressure.

3.17 Analysis Approach

We conducted a numerical sensitivity study running a series of simulations in order to answer the questions outlined in Chapter (1). We ran a total of twelve simulations, designated SN1 - SN12 (Table 3.1). Analysis of pore-pressure and salinity patterns in continental-shelf environments is complicated by multiple fluid flow and solute transport driving mechanisms that vary on geologic time scales. Ice-sheet encroachment on the continental shelf would represent an extreme form of topography-driven flow with heads up to 90 % of ice-sheet thickness imposed beneath a wet-based glacier. During periods of sea-level low-stands we would expect a topography-driven flow system to dominate with heads higher near the coastline and lower towards the continental slope (Figure

Table 3.1: Simulation Scenarios

Scenarios	Clay K_x (m^2)	Sand K_x (m^2)	Variable-Density Flow (Yes/No)	Max. Ice Sheet Extent (km) during Pre-Wisconsin	Sedimentation Deposition (Yes/No)	Pleistocene Stratigraphy	Sea-Level (Transient / Static)	Wisconsin Ice Sheet Extent (km)
SN1	10^{-16}	10^{-11}	Yes	Absent	Yes	Even Sand / Clay	Transient	Absent
SN2	10^{-16}	10^{-11}	Yes	Absent	Yes	Even Sand / Clay	Static	Absent
SN3	10^{-16}	10^{-11}	Yes	Absent	No	Even Sand / Clay	Transient	Absent
SN4	10^{-16}	10^{-11}	Yes	80	Yes	Even Sand / Clay	Transient	80
SN5	10^{-16}	10^{-11}	No	80	Yes	Even Sand / Clay	Transient	80
SN6	10^{-16}	10^{-11}	Yes	250	Yes	Even Sand / Clay	Transient	80
SN7	10^{-16}	10^{-11}	Yes	80	No	Even Sand / Clay	Transient	80
SN8	10^{-18}	10^{-11}	Yes	80	Yes	Even Sand / Clay	Transient	80
SN9	10^{-16}	$10^{-13.5}$	Yes	80	Yes	Even Sand / Clay	Transient	80
SN10	10^{-16}	–	Yes	80	Yes	Clay Rich	Transient	80
SN11	10^{-16}	10^{-11}	Yes	80	Yes	Clay Rich	Transient	80
SN12	10^{-16}	10^{-11}	No	Absent	No	Even Sand / Clay	Static	Absent

3.6a). Under these conditions, solute transport is driven by forced convection. During periods of sea-level high-stands, sea-level rise can lead to conditions of underpressure formation in fine-grained sediments that require time to equilibrate. Seawater overlying fresh water can lead to density instabilities and onset of free convection (Figure 3.6b). Rapid deglaciation can lead to sedimentation on the continental shelf and the formation of associated overpressures. This will drive saline groundwater shoreward and generate anomalously high pore pressures (Figure 3.6c).

We determined the influence of sediment loading, sea-level variation, and density instabilities on groundwater flow (Question 1) by isolating each fluid flow driving force and comparing their separate impact on simulated present-

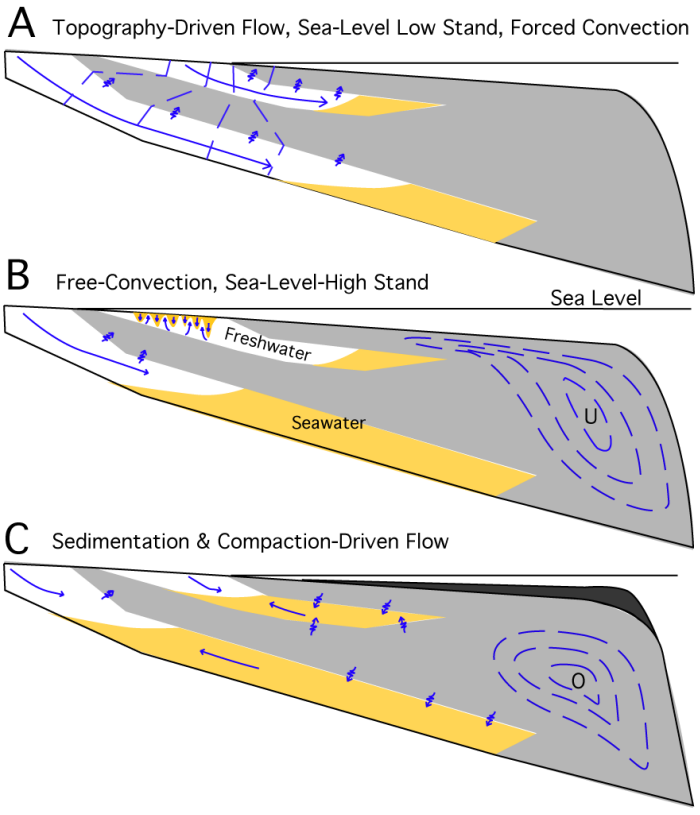

Figure 3.6: On the Atlantic continent shelf, pore-fluid driving forces include a.) forced convection due to topographic driven flow, b.) free-convection due to density instabilities at fresh water and saltwater interfaces, as well as underpressures due to average Pleistocene sea-level lower than present-day, and c.) pressure gradients caused by overpressures owing to rapid sedimentation and compaction.

day hydraulic head. For example, we compared a simulation in which we imposed both sediment loading and sea-level variation (SN1), a simulation that had a constant sea level (modern sea level) and evolving mesh (SN2), and a simulation that had a static mesh set at present-day stratigraphy and transient sea level (SN3). We determined the influence of density instabilities on groundwater flow by comparing a simulation that took into account variable water density (SN4) to a simulation that neglected water density effects (SN5); both SN4 and SN5 included an ice sheet that extended to Martha's Vineyard Island for the entire Pleistocene and sediment loading. We examined the influence of ice sheet maximum extent (Questions 2 and 3), by running simulations in which the ice sheet was absent (SN1), the ice sheet extended to Martha's Vineyard Island for all Pleistocene glaciations (80 km; SN4), and the ice sheet extended near the continental shelf-slope break for pre-Wisconsin glaciations (250 km) and then to Martha's Vineyard Island for the Wisconsin glaciation (SN6). These three simulations (SN1, SN4, and SN6) were compared to a steady state simulation that had no ice sheet represented (SN12). An in-depth comparison of salinity and hydraulic-head patterns produced by SN4 and SN7 (static mesh simulation, stratigraphy held at modern day stratigraphy) helped us ascertain the importance of using the improved hydro-stratigraphy versus a static mesh (Question 4).

Owing to the considerable uncertainty in the magnitude of sand/clay permeability and the sediment stratigraphy, we ran simulations in which we varied the permeability magnitude and the permeability distribution on the continental shelf. For most of our model runs we used a sand horizontal permeability (k_x) of 10^{-11} m^2 and a clay k_x of 10^{-16} m^2. These permeabilities were taken from prior studies and are thought to best represent actual conditions on the New England continental shelf (Person et al., 2003). These values also match permeabilities in

continental-shelf sediments in Suriname (Groen et al., 2000). We also used a k_x of 10^{-16} m^2 for glacial sediments, which is consistent with permeability measurements of tills in Missouri and Alberta (Hendry, 1982; Sharp, 1984). We were able to obtain permeability data from Cost G-1 and Cost G-2 boreholes (Figure 1.1), which were relatively high, ranging from about 10^{-9} m^2 for the highest permeability units to 10^{-15} m^2 for the lowest permeability units (Amato and Bebout, 1980; Amato and Simonis, 1980). These permeabilities were about 1-2 orders of magnitude lower than the ones estimated for shallow aquifers on Nantucket Island and Long Island, which were about 10^{-9} to $10^{-9.5}$ m^2 for sand aquifers and about 10^{-14} m^2 for clay confining units (Buxton and Modica, 1992; Guswa and LeBlanc, 1985; Person et al., 1998). Continental-shelf sediments off the coast of New Jersey had lower permeabilities, which ranged between about 10^{-16} m^2 for sand aquifers and 10^{-18} m^2 for clay aquitards (Dugan and Flemings, 2002; Dugan and Flemings, 2000; Blum et al., 1996). We ran a simulation in which we decreased the k_x of clay to 10^{-18} m^2 (SN8) and a simulation in which we decreased the k_x of the sand to $10^{-13.5}$ m^2 (SN9). We also included a simulation in which all the continental-shelf sediments, excepting the glacial tills, were given a k_x of 10^{-16} m^2 and a k_y of 10^{-17} m^2 (SN10). Finally, we ran a simulation in which the deposited Pleistocene sediments were clay rich (SN11) compared to SN1 - SN9, which had approximately an even distribution between clay and sand in the Pleistocene sediments. All simulations we ran are listed in Table 3.1. Parameters held constant in our sensitivity study are presented in Table 3.2 and Table 3.3.

In the results section, we present deviatoric head, which is the difference between hydrostatic conditions and simulated hydraulic head. The hydrostatic

Table 3.2: Constant Hydraulic Parameters

Parameter	Value
Till Permeability (K_x)	$10^{-16}\ m^2$
Longitudinal Dispersivity (α_L)	$1000\ m$
Transverse Dispersivity (α_T)	$10\ m$
Sand Specific Storage	$1x10^{-4}\ m^{-1}$
Clay Specific Storage	$1x10^{-3}\ m^{-1}$
Till Specific Storage	$1x10^{-4}\ m^{-1}$
Sand Anisotropy	100
Clay Anisotropy	10
Till Anisotropy	1
Diffusion	$3.15x10^{-3}\ m^2/yr$

conditions assumes freshwater head for seawater at standard conditions (hydrostatic heads increase linearly with depth); the hydrostatic head at sea level is 0 m. This causes topography above sea level to have negative hydrostatic heads. Using this approach, we are able to define ”overpressures” as positive deviatoric heads and ”underpressures” as negative deviatoric heads. Ultimately, while using these definitions regions above sea level, with topographic driven flow, will always be considered ”overpressured”.

Table 3.3: Constant Parameters

Parameters	Variable	Values
Water Density at Standard Conditions*	ρ_o	999.7 kg/m^3
Ice Density	ρ_i	900 kg/m^3
Water Density	ρ_w	1000 kg/m^3
Density of Seawater	$\rho_s w$	1025 kg/m^3
Water Viscosity at Standard Conditions*	μ_o	$1.3x10^{-3}$ Ns/m^2
Specific Heat Capacity of Water	c_f	1000 Cal/kgK
Specific Heat Capacity of Rock	c_s	200 Cal/kgK
Density of Rock	ρ_s	2500 kg/m^3
Thermal Conductivities of Fluid	λ_f	0.58 W/mK
Thermal Conductivities of Rock	λ_s	2.51 W/mK
Basal Temperature Gradient of Ice	β_o	0.151 K/m
Ice Thermal Diffusivity	κ	37.2 m^2/y
Ice Triple Point Temperature	T_{TP}	0.0098 ^oC
Melting Point Depression	c_i	0.0861 $^oCms^2/kg$
Density of the Mantle	ρ_m	3300 kg/m^3
Crustal Stiffness	D	$1x10^{22}$ $Pa \cdot s^2/m^2$
Mantle Response Time	τ	3 ky
Initial Porosity	ϕ_o	0.5
Bulk Compressibility	β	$5.50x10^{-8}$ Pa^{-1}

CHAPTER 4

RESULTS

In this chapter we present the results of our analysis. The sections are focused towards answering the questions outlined in Section (3.17).

4.1 Influence of Sea-Level Variation and Sediment Loading on Hydraulic Head (Question 1, part 1)

Here we analyze the effect of sea-level variation and sedimentation on simulated present-day hydraulic head, by looking at present-day deviatoric heads. We define deviatoric heads as the difference between hydrostatic and computed transient heads.

Figure 4.1 contains the present-day deviatoric head simulations for SN2 (sediment loading and erosion were represented, sea-level fluctuations were not), SN3 (sea-level fluctuations were represented, sediment loading and erosion were not), and SN1 (both sediment loading, erosion, and sea-level fluctuations were represented). In all of these model runs (SN1 - SN3), glacial effects were not considered.

In Figure 4.1 and all the following simulated present-day deviatoric head plots, deviatoric heads are defined as the difference between computed transient heads and hydrostatic freshwater heads for saltwater (density of 1025 kg/m^3). Modern sea level is assumed to have a hydraulic head and hydrostatic head of 0

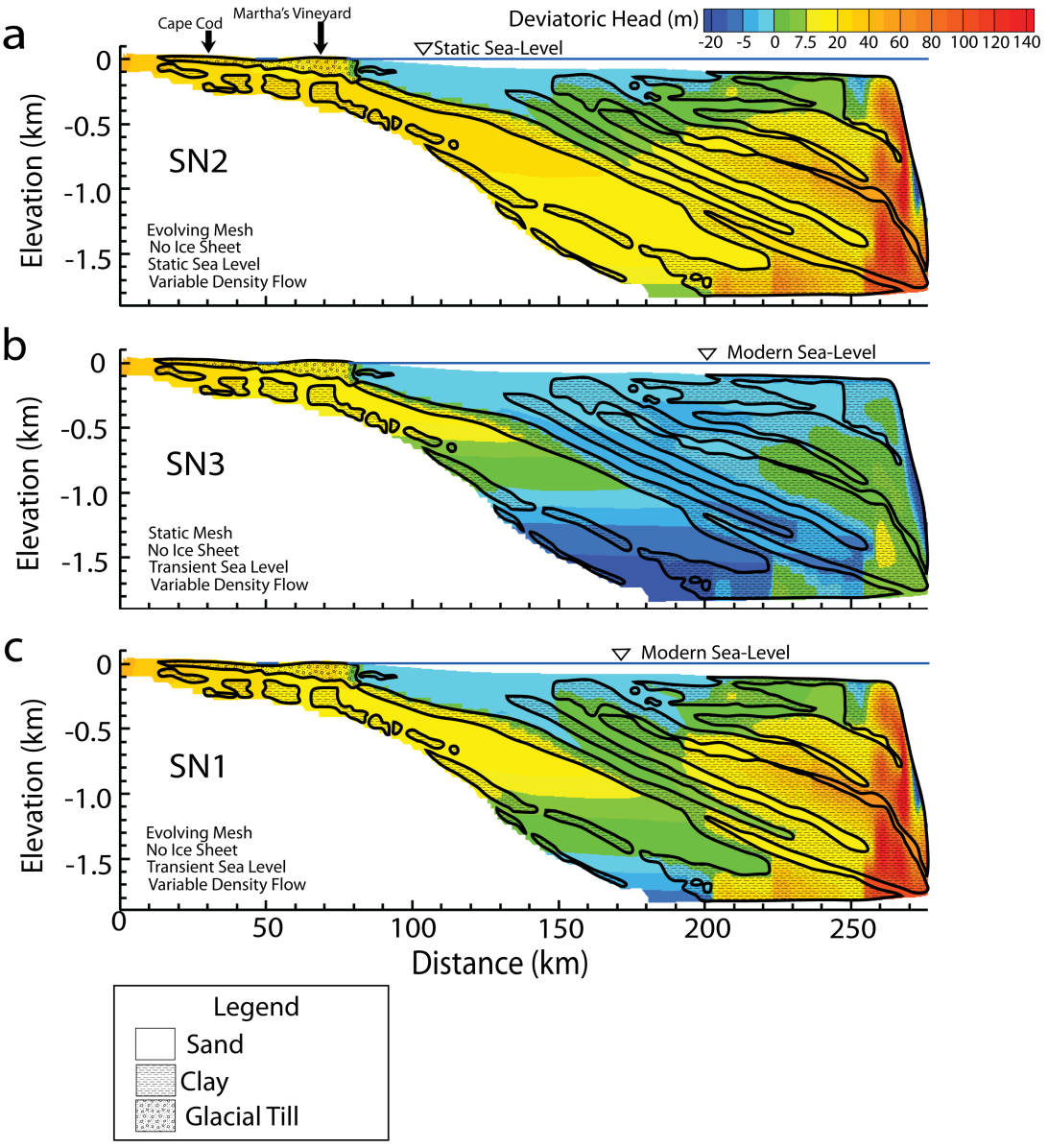

Figure 4.1: Simulated present-day deviatoric head (m) for a.) SN2, b.) SN3, and c.) SN1. Table 3.1 lists the difference between these simulations. Elevation is relative to modern sea level.

m. Further, in these figures, blue represents underpressures. Green, yellow, and red represent increasing levels of overpressures. The stippled patterns represent stratigraphy (sand, clay, till).

In SN2, the simulated present-day offshore hydraulic heads are predominantly overpressured, with large regions between 5 and 20 *m* above hydrostatic head (Figure 4.1a). The pore fluids at Martha's Vineyard Island and Cape Cod are also overpressured. This is because this area is above sea level today and the excess heads represent land surface / water table topography. The clays adjacent to the continental slope are overpressured by up to 180 *m*. These highly overpressured areas correspond with the largest sedimentation rates during the Wisconsin and the Holocene (See Figure 3.1). The strong lateral gradients of head within the clays near the continental slope reflect strong lateral gradients in imposed sedimentation. Underpressured areas (as low as -20 *m* deviatoric head) are located in shallow sediments near and on the continental slope (at 250 *km* and 270 *km* lateral distance). These underpressures correspond with areas that recently (since 225 *ka*) experienced relatively little sedimentation compared to erosion (Figure 3.1). The deviatoric heads in the deep aquifer generally decrease linearly with depth, however down to 1.2 *km* depth heads are consistently around 10 *m* above hydrostatic. This could be accounted for by the combined effect of present-day topographic driven flow at Martha's Vineyard Island and deposition of up to 30 *m* of tills (now forming Martha's Vineyard Island and Cape Cod) since 65 *ka* (see Figure 3.2). Shallow sand pore fluids on the continental shelf tend to be slightly underpressured (deviatoric heads around -1.5 *m*), which are practically hydrostatic. The simulated present-day head gradient causes dominant groundwater flow from the continental shelf-slope break towards the shoreline.

In SN3, the simulated offshore present-day deviatoric heads range from underpressured (-17.5 m) to slightly overpressured (12 m), though most of the pore pressures do not reach deviatoric heads higher than 8 m (Figure 4.1b). The present-day groundwater flow in SN3 is the same as SN2: from the continental shelf-slope break towards the shoreline.

Combining the effects of sediment loading (SN2) and sea-level variations (SN3) in SN1 results in overpressures adjacent to the continental slope and underpressures in deep sediments around 200 km lateral extent (Figure 4.1c). The highest simulated present-day deviatoric heads in SN1 are around 180 m, similar to SN2. However, the extent of high heads (indicated by the area with deviatoric heads higher than 20 m) in the continental shelf pore fluids is decreased relative to SN2, resulting from a combination of sea-level variation, associated infiltration of freshwater, and erosion.

Sea-level variations in SN1 reduced higher heads induced by sedimentation of the glacial tills that form Martha's Vineyard Island and Cape Cod; deviatoric heads in the deep aquifer are lower in SN1 than in SN2 (Figures 4.1a and 4.1c). In conclusion, sediment loading and sea-level fluctuation have a combined effect on present-day hydraulic and deviatoric heads, with sediment loading having the dominant impact. Sediment loading tends to produce a more overpressured system, while sea-level fluctuations promote an underpressured system. The more underpressured system induced by sea-fluctuations is brought about by greater infiltration of fresh water, average lower sea level than present day, and decrease in sea level since 10 ka.

4.2 Influence of Density Instabilities on Salinity Distribution (Question 1, part 2)

In this section, we investigate the effects of variable-density flow versus forced convection. We would expect that variable-density flow would lead to more saline pore fluids in coastal aquifers systems. Relatively dense seawater tends to retard influx of meteoric recharge and promote vertical saltwater fingers during periods of transgression. Figure 4.2 contains the simulated present-day salinity patterns for SN5 (no variable-density flow) and SN4 (base case simulation that takes into account variable-density flow). Sediment loading, sea-level fluctuations, and glaciations are represented in both model runs (SN5 and SN4). However, density instabilities were not permitted to form in SN5.

SN5 and SN4 show similar brackish-to-fresh water lateral extent (to about 250 km) and similar freshwater emplacement within the pore fluids under Martha's Vineyard Island and Cape Cod (Figure 4.2). Within the deep aquifer, salinities between 1 ppt and 6 ppt have a lateral thickness of 100 km in SN5 and 50 km in SN4. In the near surface sand unit between 90 km and 130 km lateral distance, pore fluids are as low as 10 ppt in SN4 and 20 ppt in SN5. In the same area (between 90 km and 130 km) and all along the surface of the continental shelf, the transition between saline water and fresh water has a diffusive appearance in SN4 and a wavy, vertical "finger" appearance in SN5. These large salinity fingers between 90 km and 130 km in Figure 4.2b are caused by density instabilities. Accounting for density instabilities also results in an overall more saline system. The effects of density instabilities can also be seen in pore fluids underneath Martha's Vineyard Island and Cape Cod, where density instabilities promoted greater penetration of saline water into clays in SN4 than in SN5.

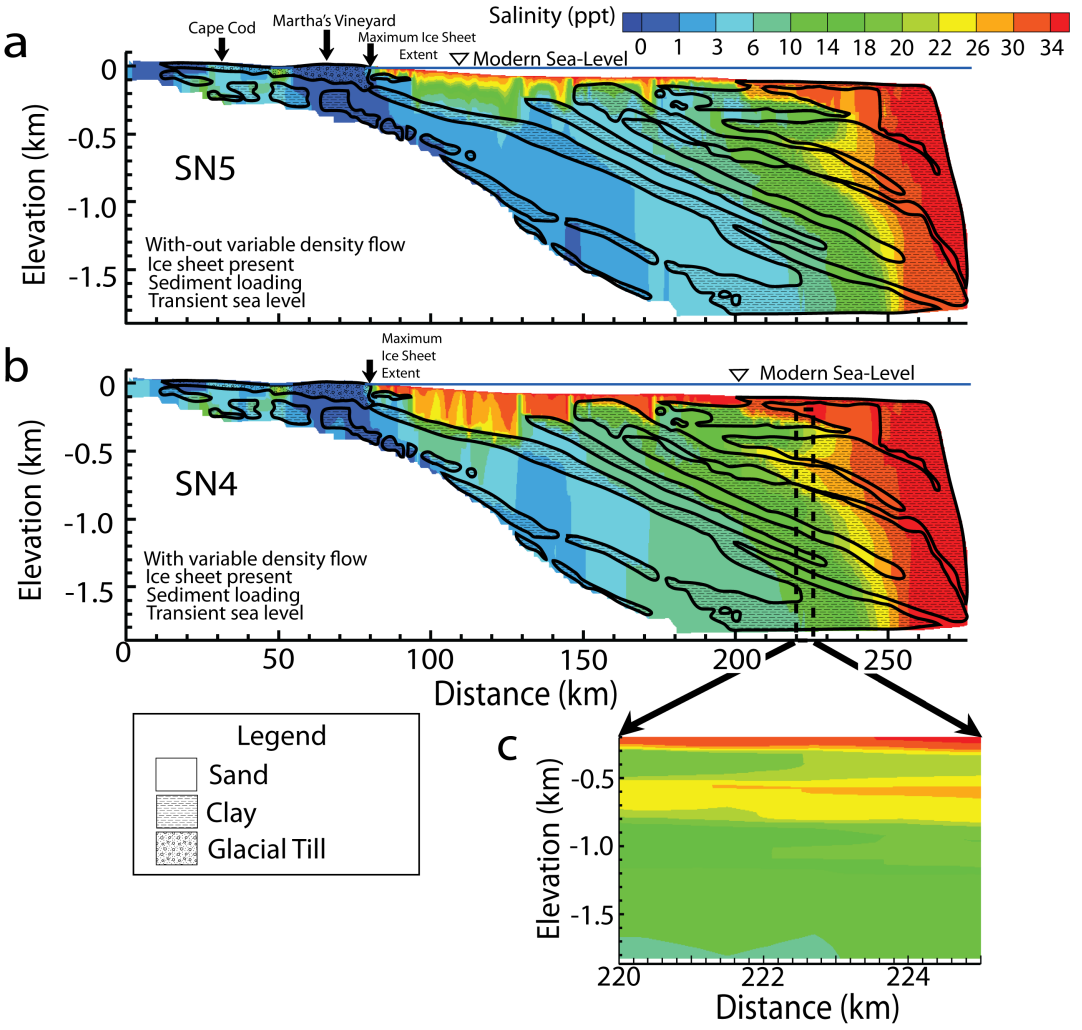

Figure 4.2: Simulated present-day salinity (ppt) for a.) SN5 and b.) SN4. Simulations parameters are listed in Table 3.1. c.) contains a portion of SN4 that has a vertical exaggeration of 1.89x. The vertical exaggeration in a.) and b.) is 43.2x. Elevation is relative to modern sea-level.

The salinity "fingers" seen in SN4 may be exaggerated by mesh effects that are causing "dimples" in SN5 in the same area. The fingering effect can be seen in all the simulations that take into account variable-density flow and may contribute to an overall vertical stripy appearance. The vertical exaggeration (43.2x) in the figures amplifies relatively small vertical differences in concentration contours (Figure 4.2b and 4.2c).

4.3 Influence of Maximum Ice Sheet Extent during Pre-Wisconsin Glaciations (Question 2 and 3)

Ice-sheet extent can influence the maximum head imposed on the continental shelf. As the ice sheet extends further onto the shelf (to 250 *km*), the maximum ice-sheet thickness on the continental shelf increases (to 1.5 *km*). In addition, the duration over which the ice-sheet boundary condition is imposed is longer for a more extensive ice sheet (16 *ky* duration during the Illinoian, when it would otherwise be 12.5 *ky* duration if it only extended to Martha's Vineyard Island). One would expect more extensive ice sheets to lead to more freshwater inflow into continental shelf sediments.

4.3.1 Effect of Ice Sheet Extent on Simulated Present-day Salinity Patterns

Figure 4.3 contains the comparison of simulated present-day salinity for the different ice-sheet extent scenarios; steady state and no ice sheet (SN12), no ice sheet (SN1), the ice sheet extended to Martha's Vineyard Island (80 *km*) for all Pleistocene glaciations (SN4), and the ice sheet extended to the continental shelf-slope break (250 *km*) for all pre-Wisconsin glaciations and then to Martha's

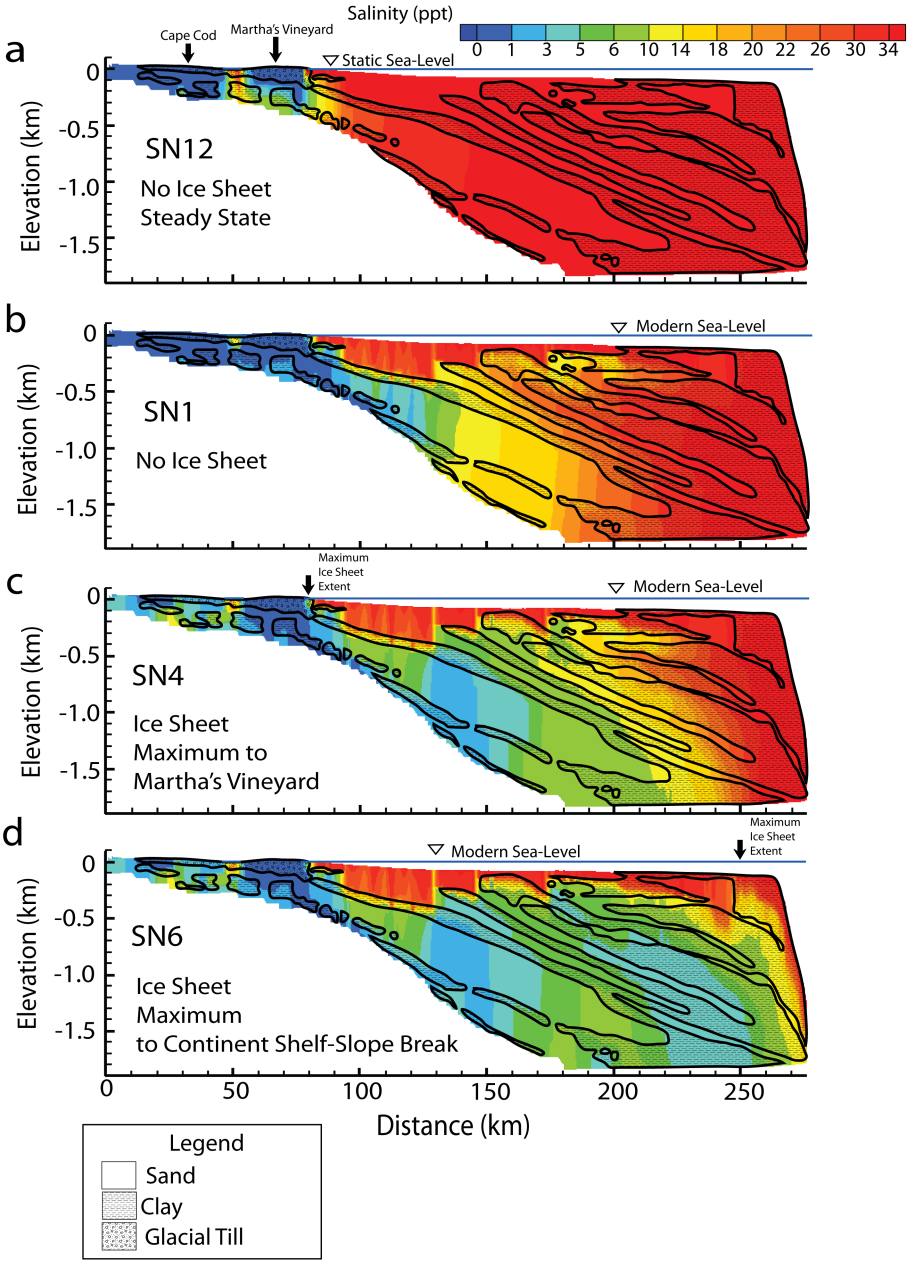

Figure 4.3: Simulated present-day salinity (ppt) of a.) SN12 (no ice sheet and steady state), b.) SN1 (ice sheet is absent), c.) SN4(ice sheet extends to Martha's Vineyard Island), and d.) SN6 (ice sheet extends near to the continental shelf-slope break during pre-Wisconsin glaciations). All models represent variable-density groundwater flow, sea-level variations, and sediment loading. Simulations parameters are listed in Table 3.1. Elevation is relative to modern sea level.

Vineyard Island for the Wisconsin glaciation (SN6). In SN1, pore fluids under Martha's Vineyard Island are relatively fresh (less than 3 ppt; Figure 4.3a and 4.4). Emplaced brackish and fresh water are dominantly restricted to the lowest aquifers and the shallow aquifer between 170 km and 220 km; pore fluids with salinities less than 14 ppt are not found in the low permeability clays adjacent to the continental slope. The furthest lateral extent of emplaced pore fluids less than 18 ppt is around 210 km. The percentage of brackish-to-fresh water (< 5 ppt) is 14 % (Table 4.1).

In SN4, relatively fresh water (less than 3 ppt) is present underneath Martha's Vineyard Island, while pore fluids under Cape Cod are more saline (up to 14 ppt; Figure 4.3b). This result seems to be counterintuitive. It is caused by the delay in flexural rebound and associated saltwater encroachment. This is known to have occurred in southern Maine and is responsible for the Presumpscot clays across coastal Maine (Anderson et al., 1990). A plume of fresher water (< 5 ppt) is present in the deep aquifer, between 120 km and 150 km. This plume is separated from fresh water under Martha's Vineyard Island by an area with salinities ranging between 5 and 10 ppt. Pore fluids with salinities less than 14 ppt and 18 ppt laterally extend to about 240 km, into low permeability clays. The percentage of brackish-to-fresh water (< 5 ppt) in SN4 is 20 %, 6 % higher than SN1 (Table 4.1).

The more extensive ice sheet in SN6, produced simulated present-day salinity patterns under Martha's Vineyard Island and Cape Cod that were similar to SN4; relatively fresh water under Martha's Vineyard Island (less than 2 ppt) and more saline water under Cape Cod (up to 14 ppt; Figure 4.3c). Plumes of relatively fresh water (between 2 and 3 ppt salinity) are in the deep aquifer between

Table 4.1: Simulated Pore-fluid Characteristics

Scenarios	% Brackish-to-Fresh Water (<5 *ppt*)	%<-10‰	% < 15,000 yrs	% 15,000 to 50,000 yrs	% 50,000 to 130,000 yrs	% >= 1 My
SN1	14	0	3	12	7	65
SN4	20	23	3	16	8	44
SN6	37	77	5	18	10	3
SN7	24	25	4	15	8	37
SN8	8	10	5	6	2	75
SN9	5	8	0.57	3	3	76
SN11	26	25	2	14	15	28

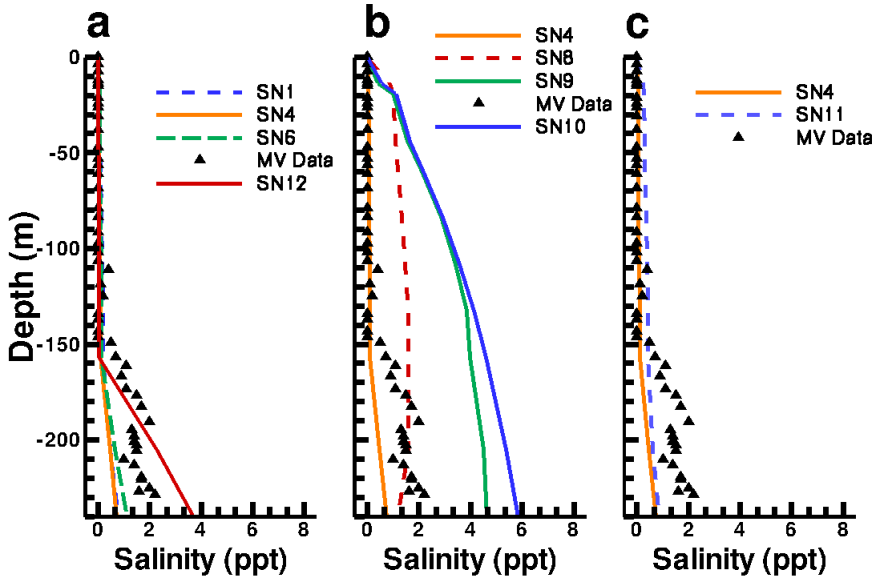

Figure 4.4: Comparison of observed and simulated present-day salinity (ppt) at Martha's Vineyard Island for a.) Figure 4.3, b.) different permeability simulations, and c.) different Pleistocene stratigraphy. Observed data is from well ENW-50. Elevation is relative to modern sea level.

120 and 150 km. Another large plume, between 3 and 5 ppt salinity, is present in the sediments between about 200 and 250 km. The deep aquifer also contains an area with salinities from 5 and 10 ppt, between 90 and 130 km. Brackish water is present (salinities less than 14 ppt and 18 ppt) to the full extent of our model domain (the continental slope, 275 km). The percentage of brackish-to-fresh water (< 5 ppt) in SN6 is 37 %, 23 % more than SN1 and 17 % more than SN4 (Table 4.1). In the absence of flexure, we would expect even more fresh water in nearshore sediments.

Simulated salinities from SN1, SN4, SN6, and SN12 illustrate that modern-day conditions will not promote infiltration of freshwater into far offshore sediments (Figure 4.3). Simulated salinities on Martha's Vineyard are similar between the four simulations (SN1, SN4, SN6, and SN12), however, SN12 (steady-state simulation) is closest to observed data (Figure 4.4). This indicates that present-day conditions likely control salinity distributions on Martha's Vineyard.

4.3.2 Effect of Ice Sheet Extent on Simulated Present-day $\delta^{18}O$ Patterns

As described in Section 3.14, the $\delta^{18}O$ composition of pore fluids on the continental shelf is controlled by its boundary condition. Beneath the ice sheet $\delta^{18}O$ has an assumed composition of -20 ‰ (Grasby et al., 2000; Remenda et al., 1994), seawater has a $\delta^{18}O$ composition of 0 ‰, and meteoric recharge has a $\delta^{18}O$ of -10 ‰. We assumed that the end member compositions did not change with time.

In Figure 4.5 infiltrated $\delta^{18}O$ patterns are consistent with salinity patterns in Figure 4.3. Unexpectedly, in SN4 and SN6 little of the simulated pore fluids have $\delta^{18}O$ near to the ice-sheet end member (-20 ‰ $\delta^{18}O$). The most depleted pore

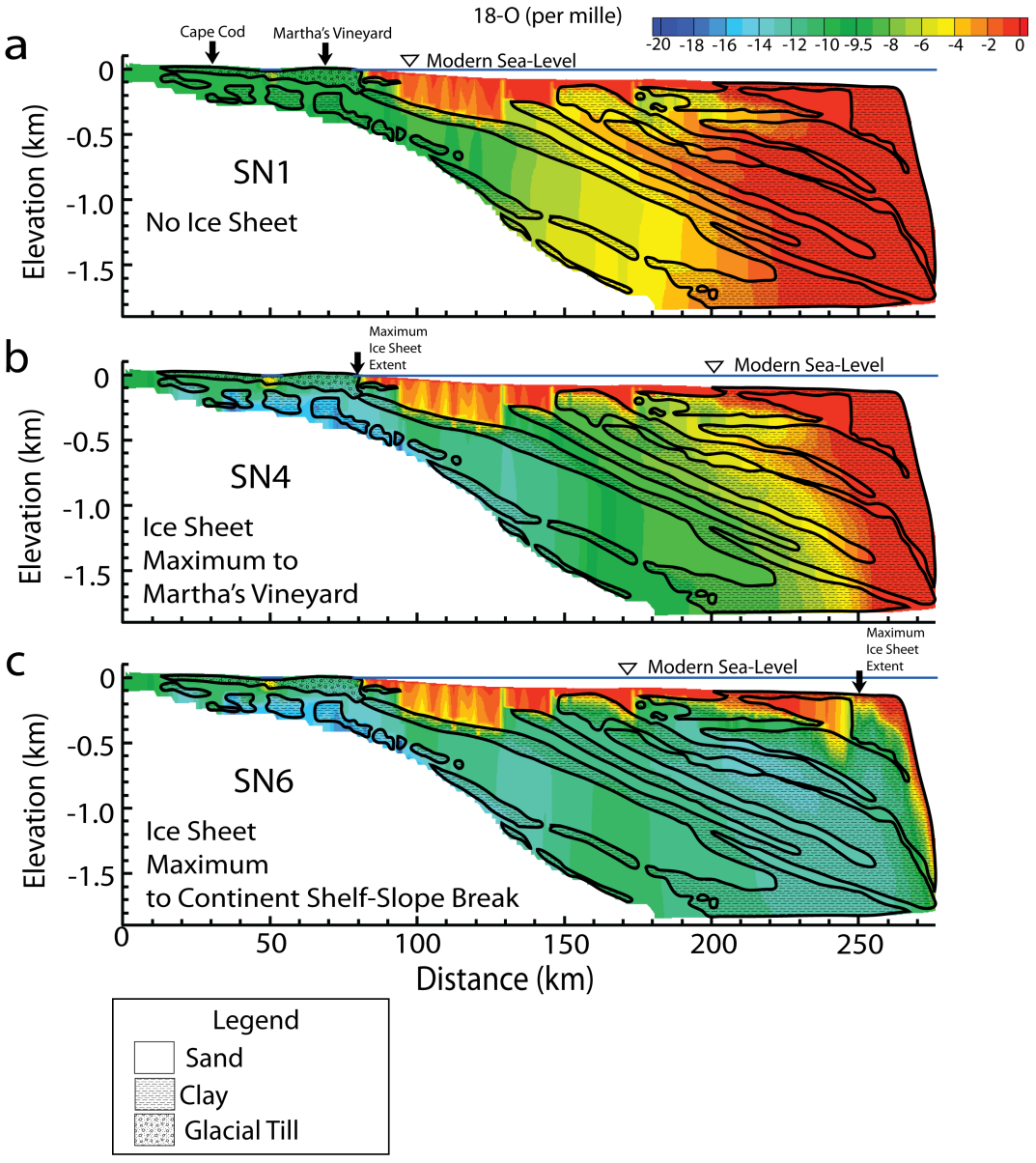

Figure 4.5: Simulated present-day $\delta^{18}O$ (per mille) of a.) SN1 (ice sheet is absent), b.) SN4 (ice sheet extends to Martha's Vineyard Island), and c.) SN6 (ice sheet extends near to the continental shelf-slope break during pre-Wisconsin glaciations). Elevation is relative to modern sea level.

fluids (between -15 ‰ and -19 ‰ $\delta^{18}O$) are sequestered in clays underneath Martha's Vineyard Island and Cape Cod, and in clays not far offshore (no greater than 90 km). Offshore continental-shelf pore fluids (greater than 90 km) reach a minimum of about -13 ‰ $\delta^{18}O$ in both SN4 and SN6. In fact, 23 % of the simulated pore fluids in SN4 and 77 % of the simulated pore fluids in SN6 had a $\delta^{18}O$ more depleted than -10 ‰ (Table 4.1).

A separate analysis (not presented here) reveals that pore fluids in the far offshore part of the model domain contained up to 30 % ice sheet meltwater for SN4 and 40 % ice sheet meltwater for SN6, while under Martha's Vineyard Island and Cape Cod this upward percentage increased to 70 % for both SN4 and SN6. In SN4, the offshore plume of brackish-to-fresh water (< 5 ppt), between 130 and 150 km, was dominantly sourced from meteoric water; 70 % of the plume came from meteoric water and 15 % came from glacial meltwater.

4.3.3 Effect of Ice Sheet Extent on Simulated Present-day Hydraulic Head Patterns

Simulated present-day deviatoric heads for SN1 (Figure 4.6a), SN4 (Figure 4.6b), and SN6 (Figure 4.6c) are similar and contain the complicated hydraulic head patterns discussed in Section 4.1. SN1, SN4, and SN6 have a dominantly non-hydrostatic system containing overpressures adjacent to the continental slope, which are associated with recent areas of sedimentation (Figure 4.6). An underpressured region, associated with an area of low sedimentation, can be seen on the continental slope. Scenarios SN1, SN4, and SN6 all produced slightly underpressured pore fluids (at most -1 m) in shallow continental shelf sediments, which for all practical purposes are hydrostatic. Further, in all the ice

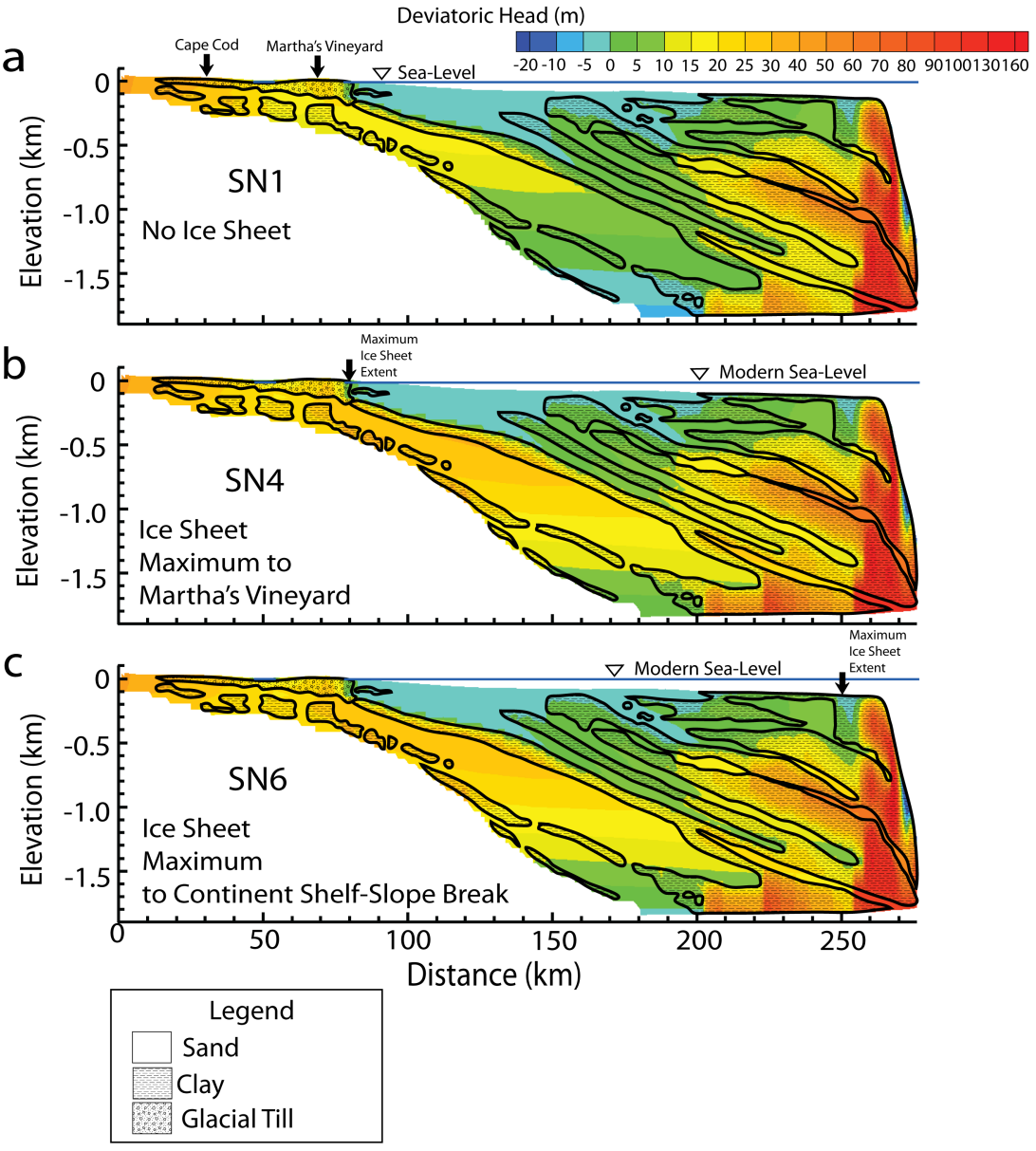

Figure 4.6: Simulated present-day deviatoric head (m) of a.) SN1 (ice sheet is absent), b.) SN4 (ice sheet extends to Martha's Vineyard Island), and c.) SN6 (ice sheet extends near to the continental shelf-slope break during pre-Wisconsin glaciations). Elevation is relative to modern sea level.

sheet simulations (SN1, SN4, and SN6) the lowest aquifer is overpressured towards Martha's Vineyard Island and becomes progressively less overpressured towards the continental slope. In SN1 and SN6, the deepest extent of the aquifer is underpressured (deviatoric heads reach -9.6 *m* for SN1 and -1.5 *m* for SN6). It is interesting to note that a deep well penetrating the sedimentary units at a distance of 180 *km* would observe underpressures and excess-pressures.

In general, implementation of the ice sheet in SN4 and SN6 resulted in higher deviatoric heads under Martha's Vineyard Island, in the deep aquifer, and in deep sediments between 180 and 250 *km* lateral distance, when compared to SN1. The simulated present-day hydraulic heads under Martha's Vineyard Island are 31 *m* above msl for both SN4 and SN6, this is 8 *m* higher than is projected for SN1 (Table 4.2). Notice that the simulated deviatoric heads for SN4 and SN6 are nearly identical.

Table 4.2: Simulated Hydraulic Head in Cretaceous Sediments under Martha's Vineyard Island

Scenarios	Average Head (m)
SN1	23
SN4	31
SN6	31
SN7	27
SN8	104
SN9	22
SN11	56

4.3.4 Simulated Deviatoric Head During Ice Sheet Maxima

In order to illustrate changes in flow during glaciations, we plotted deviatoric heads during recent glacial maxima (Wisconsin and Illinoian) for SN1,

SN4, and SN6 in Figure 4.7. During the Wisconsin (about 20 *ka*), sedimentation was occurring near the continental shelf-slope break. Subaerial clinoforms can be observed between 180 and 210 *km* lateral distance in SN1, SN4, and SN6. The sea level is at 115 *m* below modern sea-level. Permafrost has formed, reaching about 150 *m* thick, along the subaerial continental shelf. In simulations that implemented the ice sheet (SN4 and SN6), the ice sheet is at its maximum extent (Martha's Vineyard Island, 80 *km* in our simulation domain) and height (1.1 *km*) during the Wisconsin. Under the weight of the ice sheet, lithospheric flexure reached a maximum of 400 *m* (Figure 4.7b and 4.7c). Permafrost is absent underneath the ice sheet.

In the simulation without the ice sheet (SN1), the aerially exposed continental shelf results in topographic-driven flow (head gradient equal to 0.0005 m/m) that focuses fresh water through the sand aquifers (Figure 4.7a). During the Wisconsin, in SN4 and SN6, the deviatoric head grades from 1050 *m* under the thickest part of the ice sheet (0 *km*) to 19 *m* at the edge of the ice sheet (80 *km*), producing a head gradient of 0.00416 m/m across the continental shelf. The heads induced by the ice sheet are focused down through the deep aquifer. Groundwater flow is directed down the deep aquifer and up the closest overlying aquifers, preventing infiltration of meteoric water (Figure 4.7b and 4.7c). In SN6, during the Illinoian the ice sheet extended to the continental shelf-slope break. The lithosphere is depressed by a maximum of 500 *m*. Deviatoric head (and hydraulic head) is shore normal, grading from 1433 *m* on the far left side of our domain to 63 *m* at the continental slope, resulting in a head gradient of 0.0055 m/m. Groundwater flow is directed down through all the sand aquifers (Figure 4.7d).

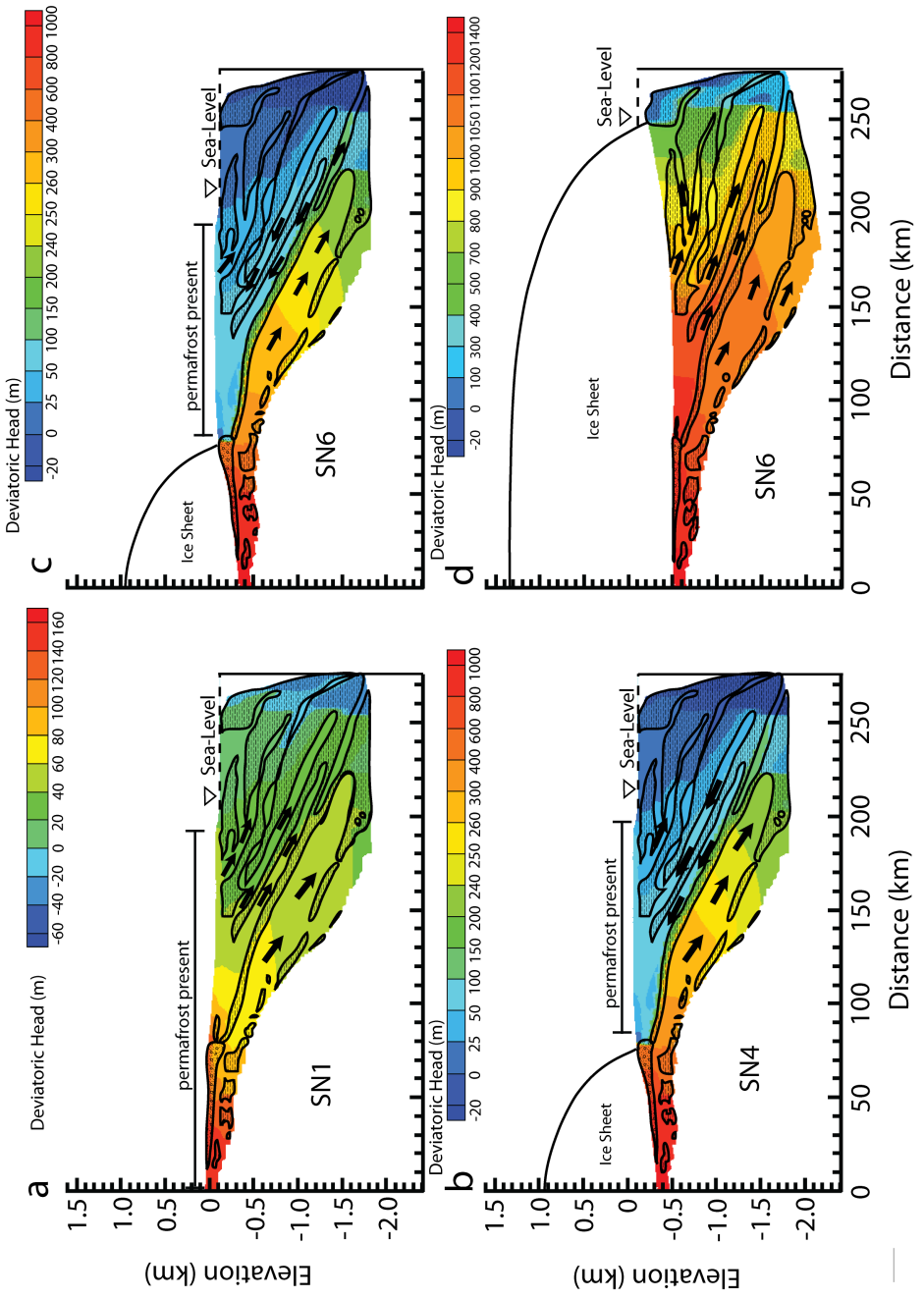

Figure 4.7: Simulated deviatoric head (m) of a.) SN1 (ice sheet is absent) at 20 *ka*, b.) SN4 (ice sheet extends to Martha's Vineyard Island) at 20 *ka*, c.) SN6 (ice sheet extends near to the continental shelf-slope break during Illinoian glaciation) at 20 *ka*, and d.) SN6 at 140 *ka*. Arrows represent the dominant flow direction. Elevation is relative to modern sea level.

4.3.5 Water Age for Ice Sheet Scenarios

We simulated groundwater age for SN1, SN2, and SN6 (Figure 4.8). In SN1, groundwater ages in clays under Martha's Vineyard Island range between about 130 *ky* and 1 *My*, the more permeable sediments above the clays have groundwater ages that range between 0 and 130 *ky* (Figure 4.8a). In the deep aquifer, pore fluids with groundwater ages up to 130 *ky* and 199 *ky* laterally extend to 118 *km* and 123 *km*, respectively. Along the surface of the continental shelf (between 130 and 275 *km*), pore fluids with ages less than 199 *ky* do not reach more than around 200 *m* depth. In the near surface sands between 90 and 130 *km* lateral distance, where instability fingering occurs, pore-fluid ages are dominantly 50 *ky* and less (Figure 4.8a). In SN4, pore fluids in clays underneath Martha's Vineyard Island have ages between 199 and 50 *ky*; overlying sediments have ages that are 50 *ky* and less (Figure 4.8b). In the deep aquifer, pore fluids with groundwater ages less than 130 *ky* extend to 112 *km* laterally and pore fluids with groundwater ages less than 199 *ky* extend to 126 *km*. Groundwater ages along the surface of the continental shelf are similar to SN1 (Figure 4.8b). In SN6, simulated pore fluids underneath Martha's Vineyard Island and Cape Cod are similar to SN4 (Figure 4.8c). The lateral extent of pore fluids with ages less than 130 *ky* in the deep aquifer is 124 *km*, the same as SN4. However, the lateral extent of the pore fluids with ages to 199 *ky* is to 155 *km*, 19 *km* greater than SN4. The depth of pore fluids along the continental shelf surface with groundwater ages less than 199 *ky* is about 400 *m*. The age of pore fluids in the shallow sands, between 90 and 130 *km*, are the same as SN1 and SN4 (50 *ky* and less; Figure 4.8c). SN1, SN4, and SN6 all contain large areas of pore fluids greater than 199 *ky*. SN1 and SN4 also have significant percentages of the domain with groundwater ages greater than 1 *My* (65 % for SN1 and 44 % for SN4; Figure 4.8 and Table 4.1).

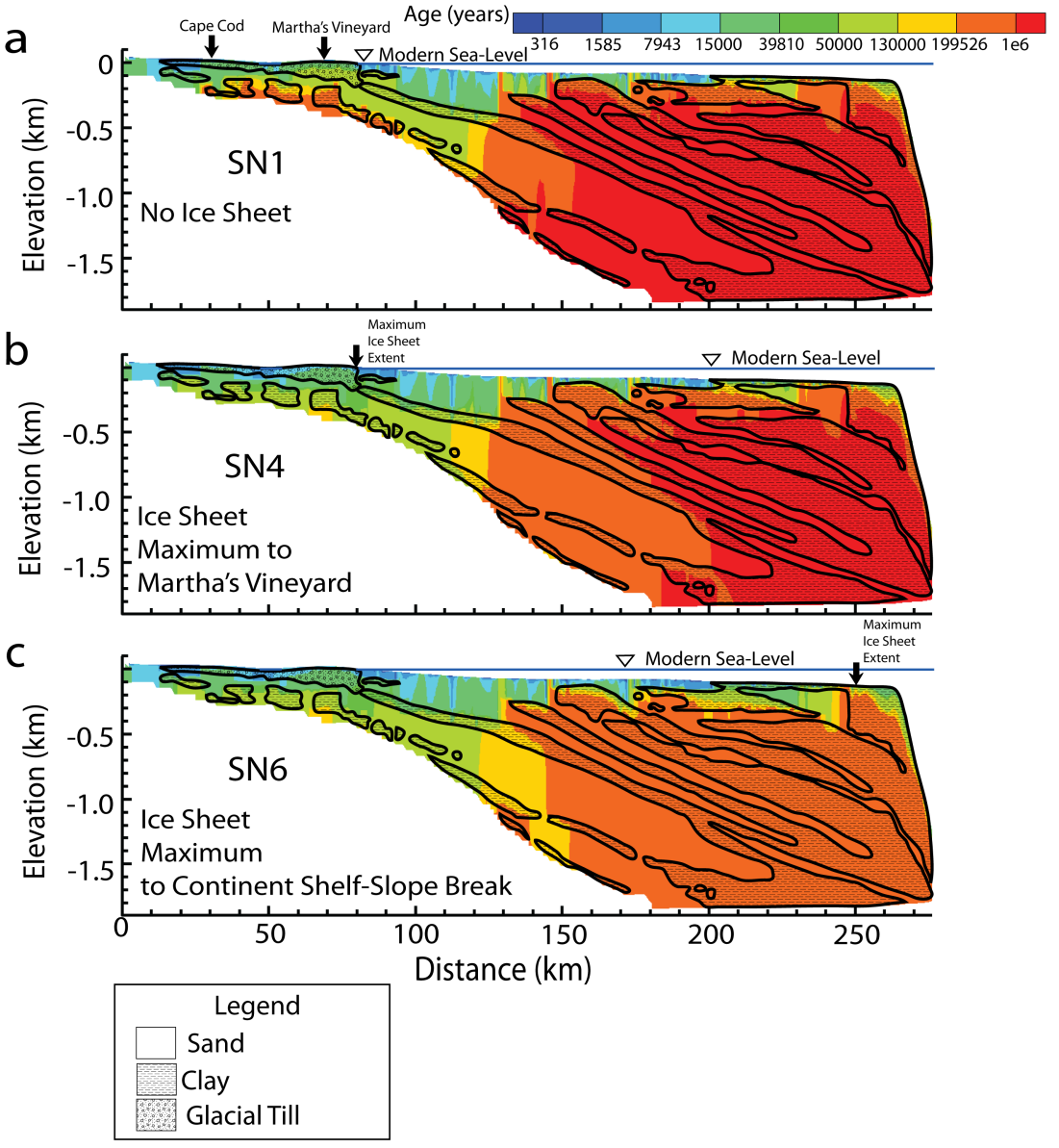

Figure 4.8: Simulated present-day age for scenarios with a.) no ice sheet (SN1), b.) the ice sheet extending to Martha's Vineyard Island (80 *km*; SN4), and c.) the ice sheet extending near the continental shelf-slope break (250 *km*; SN6). The mantle response time was 3000 years. Elevation is relative to modern sea level.

We divided the groundwater ages into three important time periods, 15 *ky* represents water that has infiltrated since the end of the Wisconsin glaciation, 50 *ky* is the maximum carbon dating age, and 130 *ky* signifies water that has infiltrated since the end of the Illinoian glaciation. The percentage of area that has groundwater ages less than 15 *ky* is 3 % in SN1, 3 % in SN4, and 5 % in SN6 (Table 4.1). The percentage of area that has ages between 15 *ky* and 50 *ky* is 12 % for SN1, 16 % for SN4, and 18 % for SN6. In SN1 7 % of the pore fluids have ages between 50 *ky* and 130 *ky*; this number increases to 8 % for SN4 and 10 % for SN6. This information indicates that implementing the ice sheet (in SN4 and SN6) decreased the groundwater age of the continental-shelf pore fluids more than when the ice sheet was absent (SN1). Further, the more expansive ice sheet not only decreased the the age of deep pore fluids, it increased the area that has younger pore fluids (less than 130 *ky*).

4.3.6 Infiltration and Discharge for Ice Sheet Scenarios

Here we present the results for the simulated cumulative infiltration and discharge along the surface of our mesh for SN1 (no ice sheet; Figure 4.9), SN4 (maximum extent of ice sheet to Martha's Vineyard Island; Figure 4.10), and SN6 (maximum extent of ice sheet to continental shelf-slope break; Figure 4.11). For SN1, since 200 *ka* the net flux oscillates around 0 $m^3/m/yr$, generally only veering by at most $0.2x10^4$ $m^3/m/yr$. Discharge and infiltration reach a maximum of about $0.65x10^4$ $m^3/m/yr$ and $-0.75x10^4$ $m^3/m/yr$, respectively, as sea level is decreasing (200-160 *ka* and 70 - 42 *ka*) and rising (135 - 125 *ka* and 12.5 *ka*- present-day). Infiltration and discharge drastically decrease in magnitude to between $0.05x10^4$ and $0.1x10^4$ $m^3/m/yr$ during periods in which temperatures are low

and permafrost formed (160 - 135 *ka* and 42 - 12.5 ka). During periods in which sea level is high (130 - 70 *ka*), the magnitude of infiltration and discharge oscillates between $0.15x10^4$ and $0.3x10^4$ $m^3/m/yr$.

Infiltration and discharge patterns in SN1, SN4, and SN6 are nearly identical during non-glacial periods (Figures 4.9, 4.10, and 4.11). As the ice sheet initially moves onto the continental shelf (150 and 32 *ka*), both infiltration and discharge peak, with infiltration dominating (negative net flux). Net flux increased logarithmically towards 0 $m^3/m/yr$ during the period in which the ice sheet was at its maximum (Figures 4.10 and 4.11). A positive net flux peak (over all discharge) occurred when the ice sheet began to wane and retreat (134 and 15 *ka*). The net flux decreased logarithmically with time after the ice sheet moved away from the continental shelf. Net flux during the last glacial period was about $-0.15x10^4$ $m^3/m/yr$ for SN4 and $0.24x10^4$ $m^3/m/yr$ for SN6 as the ice sheet waxed on to the continental shelf and $0.73x10^4$ $m^3/m/yr$ for both SN4 and SN6 as the ice sheet waned (Figures 4.10 and 4.11). During the Illinoian glaciation (about 150 - 130 *ka*), the net flux peaked at around $-0.58x10^4$ $m^3/m/yr$ for SN4 and $-6.0x10^4$ $m^3/m/yr$ for SN6 as the ice sheet waxed and $3.3x10^4$ $m^3/m/yr$ for SN4 and $9.6x10^4$ $m^3/m/yr$ for SN6 as the ice sheet waned. Notice in Figure 4.11, the net flux oscillates between net infiltration and net discharge during ice-sheet waxing and waning, even so net infiltration dominated as the ice sheet moved onto the continental shelf and net discharge dominated as the ice sheet moved off. The oscillations are likely caused by a series of damped responses to progressively increasing added loads on the system.

Figure 4.12 presents calculated fluxes for two points on the surface of the mesh for SN4. One of the points is at Martha's Vineyard Island (71.8 *km*) and

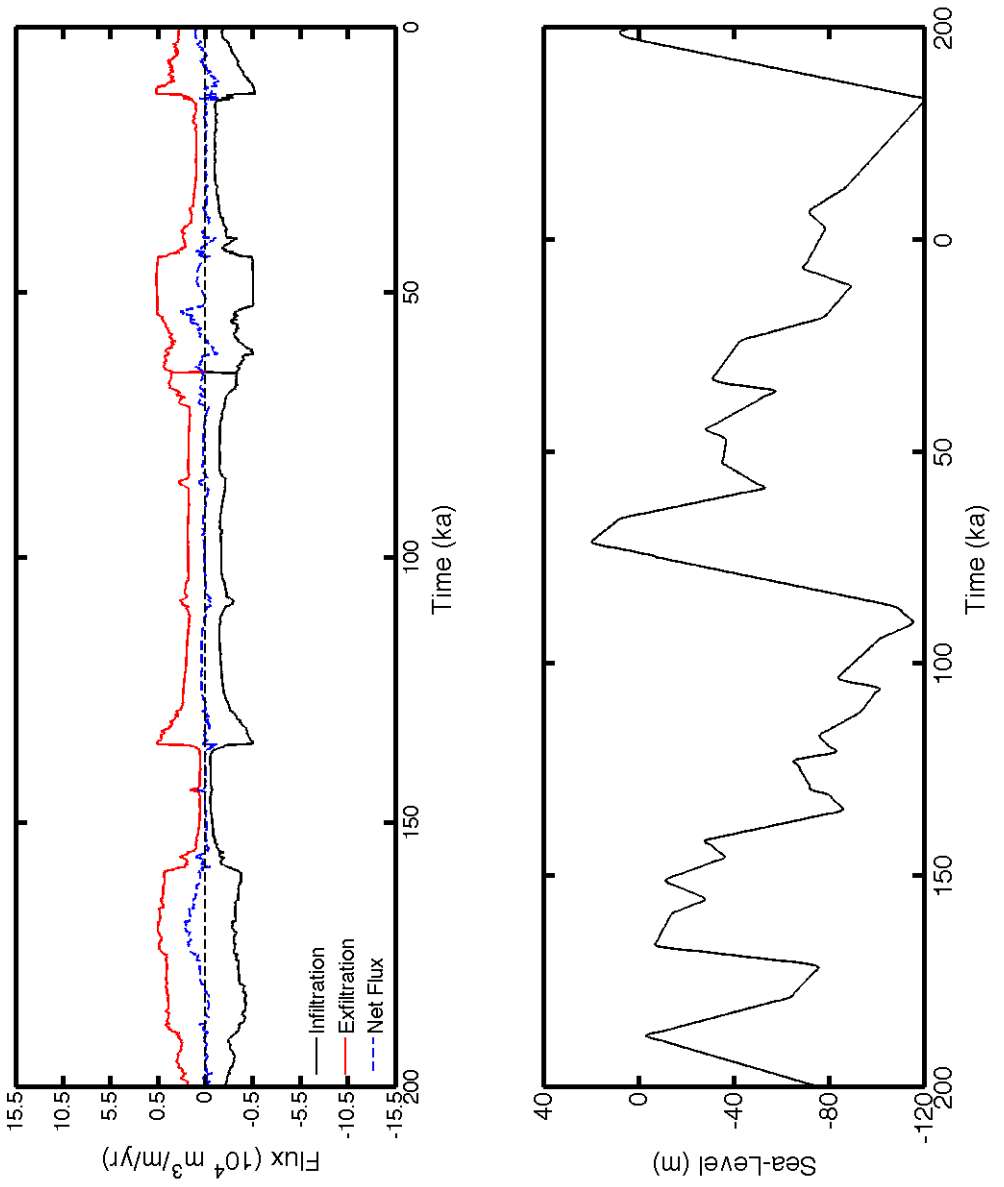

Figure 4.9: Cumulative surface infiltration (solid black line), exfiltration (solid red line), and net flux (dashed blue line) for SN1 (no ice sheet simulation). A black dashed line runs through 0 $m^3/m/yr$ flux. The y-axis is non-linear; the vertical increment increases by an order of magnitude for values greater than 0.5 $m^3/m/yr$ and values less than -0.5 $m^3/m/yr$. Changes in flux are due to sea-level fluctuations and sedimentation. Sea level is plotted on the bottom.

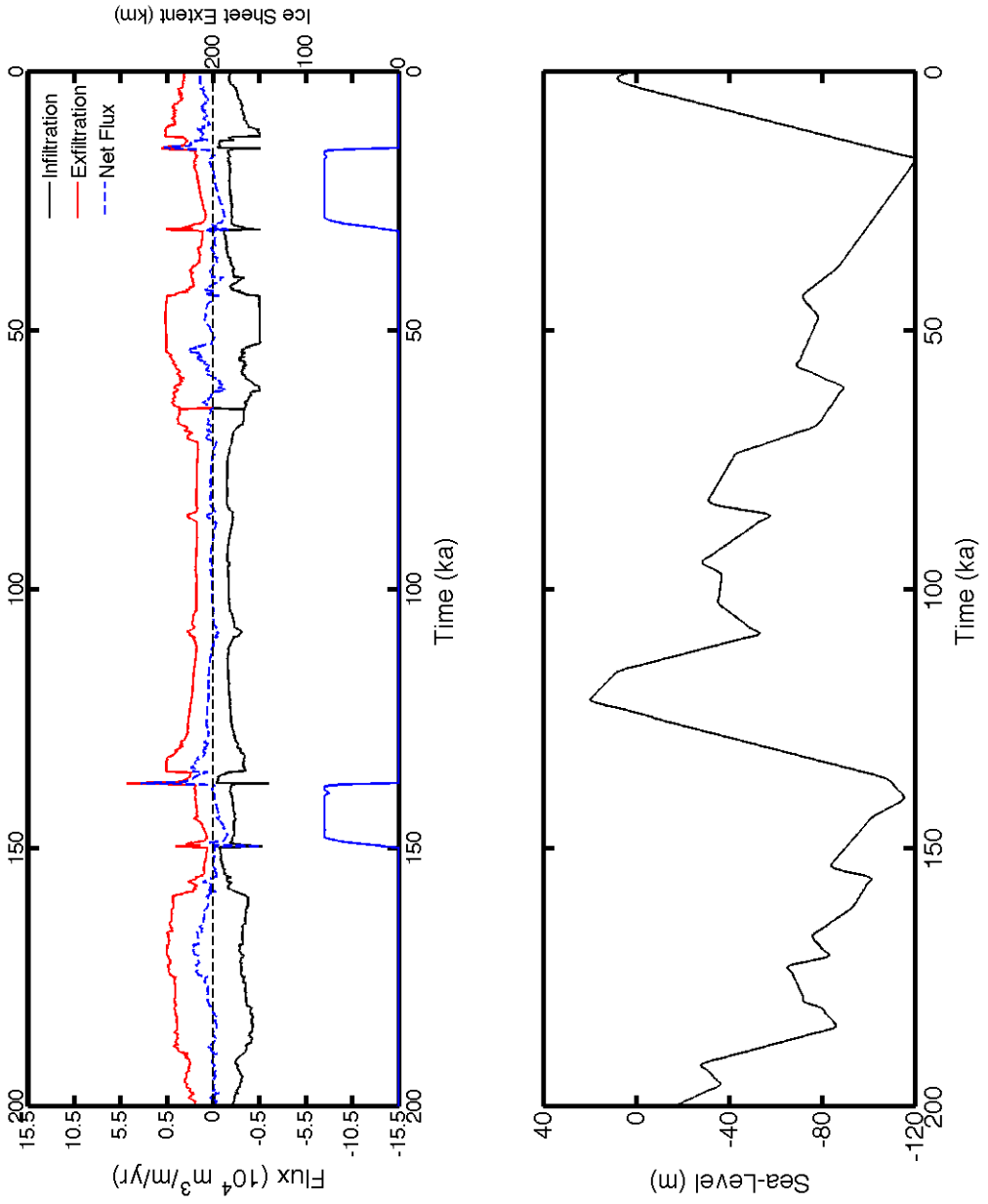

Figure 4.10: Cumulative surface infiltration (solid black line), exfiltration (solid red line), net flux (dashed blue line), and ice sheet extent on the continental shelf (solid blue line) for SN4 (ice sheet extended to 80 km for entire Pleistocene). A black dashed line runs through 0 $m^3/m/yr$ flux. The y-axis is non-linear; the vertical increment increases by an order of magnitude for values greater than 0.5 $m^3/m/yr$ and values less than -0.5 $m^3/m/yr$. Sea level is plotted on the bottom.

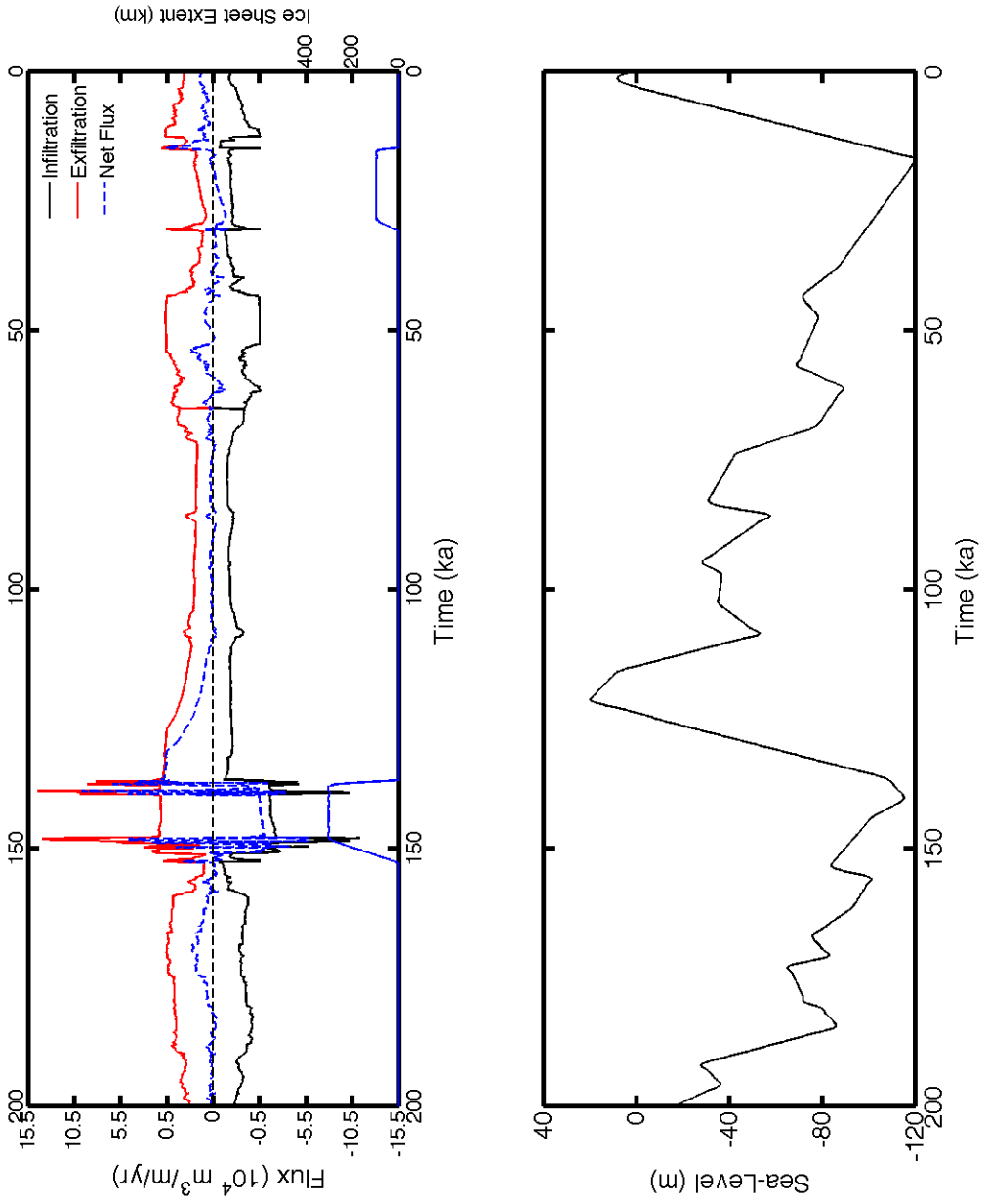

Figure 4.11: Cumulative surface infiltration (solid black line), exfiltration (solid red line), net flux (dashed blue line), and ice sheet extent on the continental shelf (solid blue line) for SN6 (ice sheet extended to 250 km during the pre-Wisconsin glaciations). A black dashed line runs through 0 $m^3/m/yr$ flux. The y-axis is non-linear; the vertical increment increases by an order of magnitude for values greater than 0.5 $m^3/m/yr$ and values less than -0.5 $m^3/m/yr$. Sea level is plotted on the bottom.

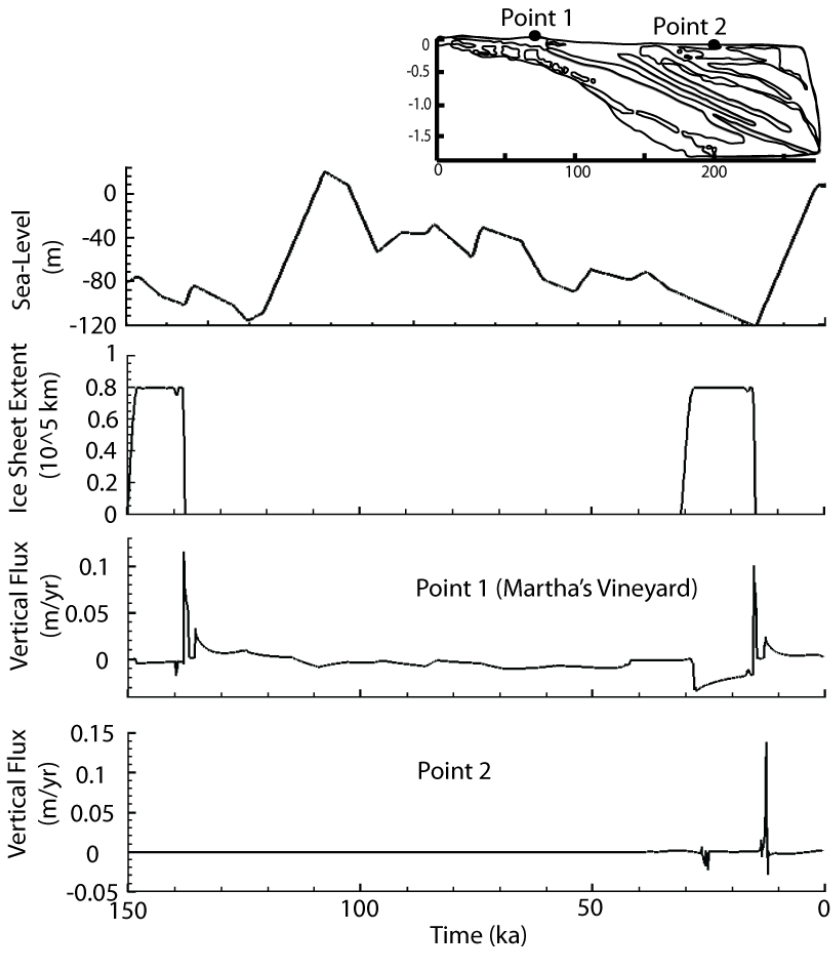

Figure 4.12: Sea level, lateral ice sheet extent relative to our model domain, and surface vertical flux at Martha's Vineyard Island (71.8 *km*; Point1) and 200 *km* (Point 2) for SN4 (ice sheet extended to 80 *km* for entire Pleistocene). These plots are limited to the last 150 *ky*, which includes the Illinoian and Wisconsin glaciations. When the flux is positive it represents discharge (exfiltration) and when the flux is negative it represents recharge (infiltration).

the other is located at the far end of the continental shelf (200 km). Point 1, at Martha's Vineyard Island, alternates between infiltration (-0.03 m/yr) when the ice sheet is prograding on the shelf and discharge (0.11 m/yr) as the ice sheet moves off the shelf. Point 2 (200 km) has a vertical flux that is dominantly 0 m/yr, except for a slightly delayed response (by about 3 ky relative to Point 1) to the Wisconsin ice sheet forcing, which peaks at -0.02 m/yr when the ice sheet is moving onto the shelf and 0.14 m/yr when the ice sheet leaves the shelf. Point 2 displays no response to the Illinoian glaciation (vertical flux remains at 0 m/yr). Between 225 and 65 ka, Point 2 was dominantly on the surface of a clay unit, which likely retarded vertical flux (Figure 3.1). Point 2 shows no response to sea-level fluctuations, however there might be a minor and highly damped response at Point 1 (Figure 4.12).

4.4 Influence of Sedimentation on Salinity and Deviatoric Head Distribution (Question 4)

Continental shelf environments evolve due to deposition, subsidence, and erosion. These processes result in a transient permeability distribution, variant topography along the top surface, and accumulation of a deepening wedge of continental shelf sediments. The permeability and topography of the top units should control, in part, infiltration and/or discharge rates. For example, the deposition of low-permeability tills along the top surface can greatly restrict fresh-water infiltration rates during sea-level high-stands, as well as infiltration of sea-water during sea-level high-stands and seawater inundation caused by flexure. Thus an evolving mesh should have different infiltration patterns than a non-evolving mesh. To complicate this is the influence of increased heads induced by sediment loading, which should act to impede emplacement of fresh water.

Figure 4.13 contains simulated present-day salinity for SN4 (evolving mesh including sedimentation) and SN7 (static mesh not including sedimentation). Salinity patterns under Martha's Vineyard Island and Cape Cod are similar between SN4 and SN7. The lateral extent of present-day freshwater emplacement ($< 18\ ppt$) in continental shelf pore fluids is to around 240 km in SN4 and 250 km in SN7. However, SN7 has overall relatively more fresh continental shelf pore fluids than SN4. The percentage of brackish-to-fresh water ($< 5\ ppt$) in SN7 is 24 %, 4 % more than SN4 (Table 4.1). Further, in SN7 there is not as focused penetration of relatively fresh water into the shallow aquifers between 170 and 220 km as can be seen in SN4, likely due to the absence of localized topographic driven flow during Wisconsin sea-level low-stands (Figure 4.7).

In SN7, the percentage of pore fluids that has $\delta^{18}O$ less than -10 ‰ is 25 %, 2 % more than SN4. Further, the percentage of pore fluids with a groundwater age less than 130 ky is 27 % (the same as SN4) and the amount greater than 1 My is 37 % (7 % less than SN4; Table 4.1).

In SN7, present-day offshore heads are more underpressured (more negative deviatoric heads) than SN4 (Figure 4.14). Underpressured regions dominate shallow sandy aquifers and the deepest end of the lowest aquifer (deviatoric head as low as $-6\ m$). Slightly overpressured areas include the deep aquifer (up to 17 m above hydrostatic), deep clays (up to 50 m), and clays adjacent to the continental shelf (up to 12 m). These are respectively 10 m, 30 m, and at least 130 m less than deviatoric heads simulated for the same areas in SN4. In SN7, the average hydraulic head in Cretaceous sediments under Martha's Vineyard is about 27 m above modern sea-level, 4 m less than SN4 (Table 4.2).

We also output the cumulative vertical surface flux for SN7 (Figure 4.15). The net flux oscillates around 0 $m^3/m/yr$, veering by at most $0.1x10^4\ m^3/m/yr$.

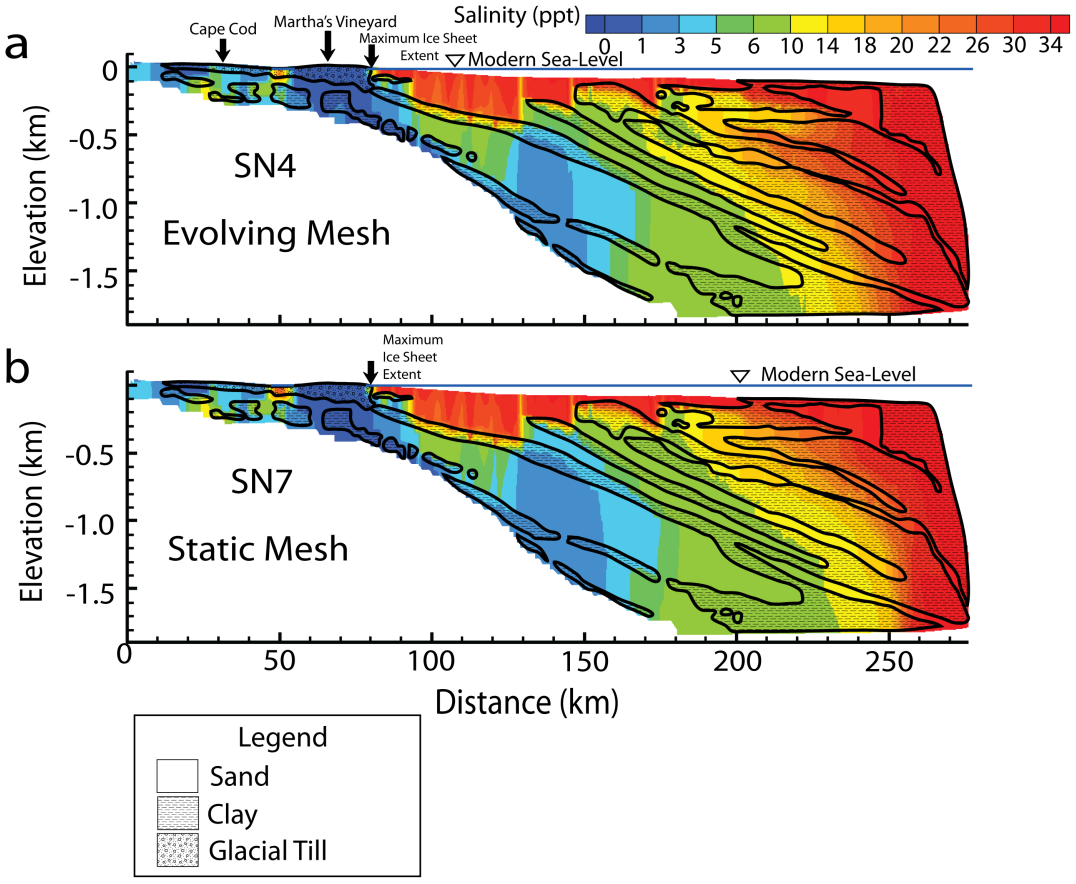

Figure 4.13: Simulated present-day salinity (ppt) distribution for a.) evolving (SN4) and b.) static grid (SN7). Elevation is relative to modern sea level.

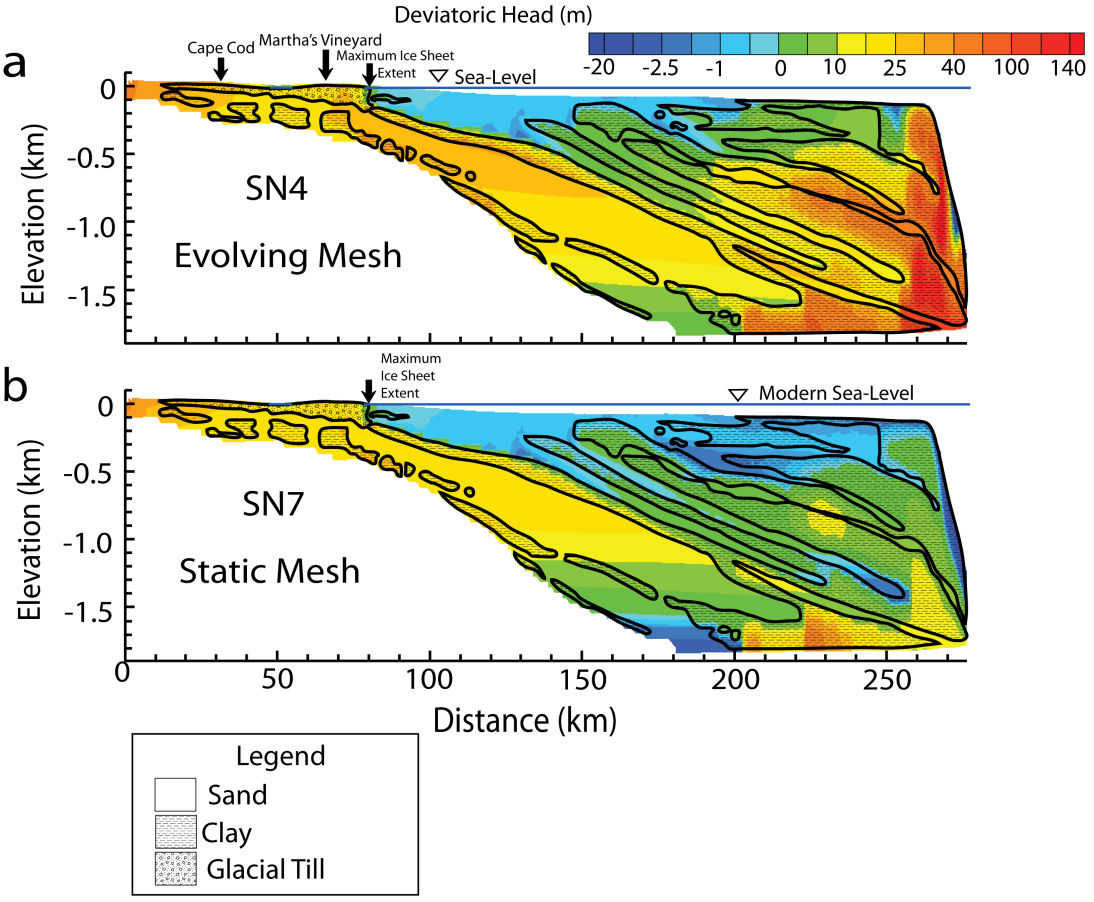

Figure 4.14: Simulated present-day deviatoric head (m) distribution for a.) evolving (SN4) and b.) static grid (SN7). Elevation is relative to modern sea level.

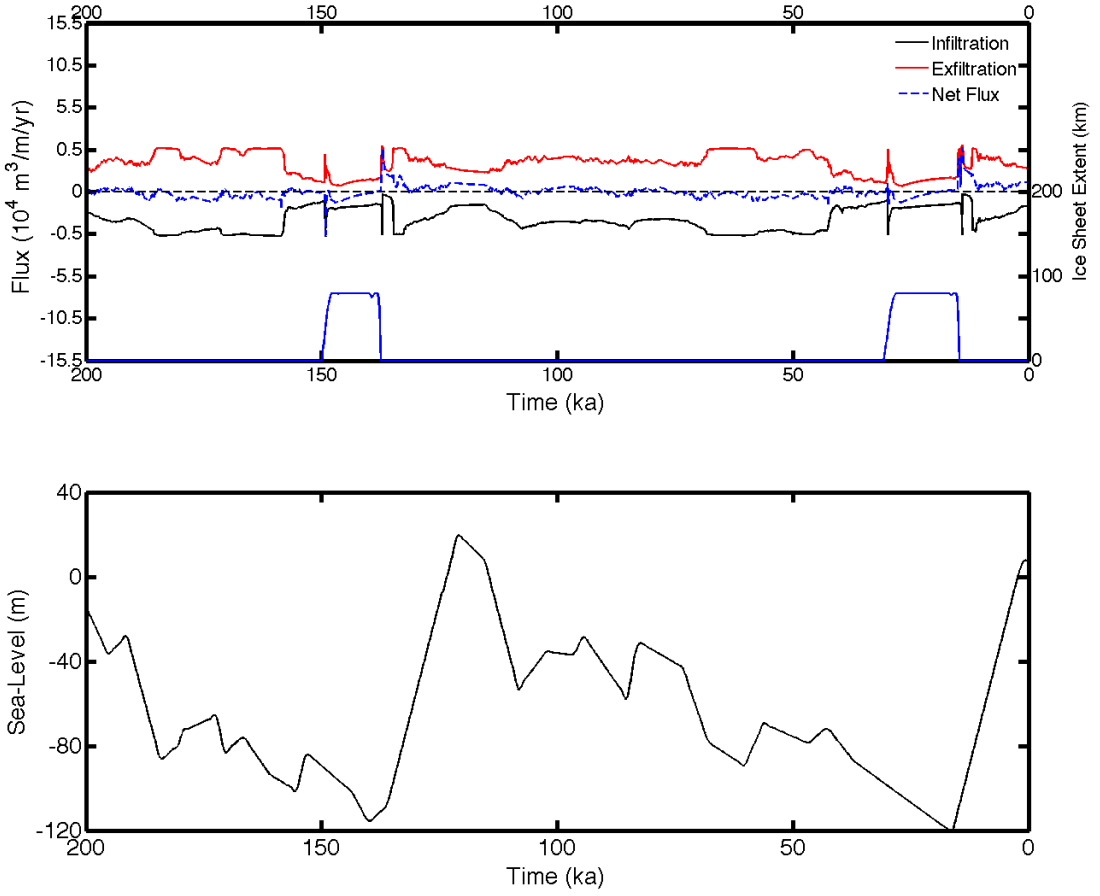

Figure 4.15: Cumulative surface infiltration (solid black line), exfiltration (solid red line), net flux (dashed blue line), and ice sheet extent on the continental shelf (solid blue line) for SN7 (static grid). The y-axis is non-linear; the vertical increment increases by an order of magnitude for values greater than 0.5 $m^3/m/yr$ and values less than -0.5 $m^3/m/yr$. Sea level is plotted on the bottom.

The only exception is during glacial periods, in which net flux peaks at about $-0.15x10^4\ m^3/m/yr$ (Wisconsin glaciation) to $-0.57x10^4\ m^3/m/yr$ (Illinoian glaciation) as the ice sheet moves on to the continental shelf and $0.7x10^4\ m^3/m/yr$ when the ice sheet moves off from the continental shelf.

4.5 Sensitivity of Simulated Present-day Salinity and Deviatoric Head Distributions to Permeability (Question 5)

We would expect low permeability conditions to retard freshwater emplacement and enhance excess pressures. We investigated the sensitivity of our simulated present-day pore fluid chemistry and deviatoric head to permeability by separately decreasing the permeability of the clay (SN8) and the sand (SN9) and then comparing simulated present-day salinities in Figure 4.16 and simulated present-day deviatoric heads in Figure 4.17. We also present results from a homogeneous stratigraphy (SN10).

In SN8 (clay permeability decreased to $k_x = 10^{-18}\ m^2$ and $k_z = 10^{-19}\ m^2$, relative to SN4), present-day emplaced fresh water is restricted to sand aquifers at least partially confined by clay units (Figure 4.16b). Compared to SN4 (Figure 4.16a), SN8 has less area that has emplaced fresh water. The deep lateral extent of pore fluids with pore chemistry less than 14 ppt salinity is 170 km, 70 km less than SN4. The percentage of pore fluids that contain brackish-to-fresh water ($<$ 5 ppt) is 8 %, 12 % less than SN4 (Table 4.1). The percentage of pore fluids that has $\delta^{18}O$ less than -10 ‰ is 10 %, 13 % less than SN4. Further, the percentage of pore fluids with a groundwater age less than 130 ky is 13 % (14 % less than SN4) and the amount greater than 1 My is 75 % (31 % greater than SN4). The clays underlying Martha's Vineyard Island have pore fluid salinities up to 5 ppt,

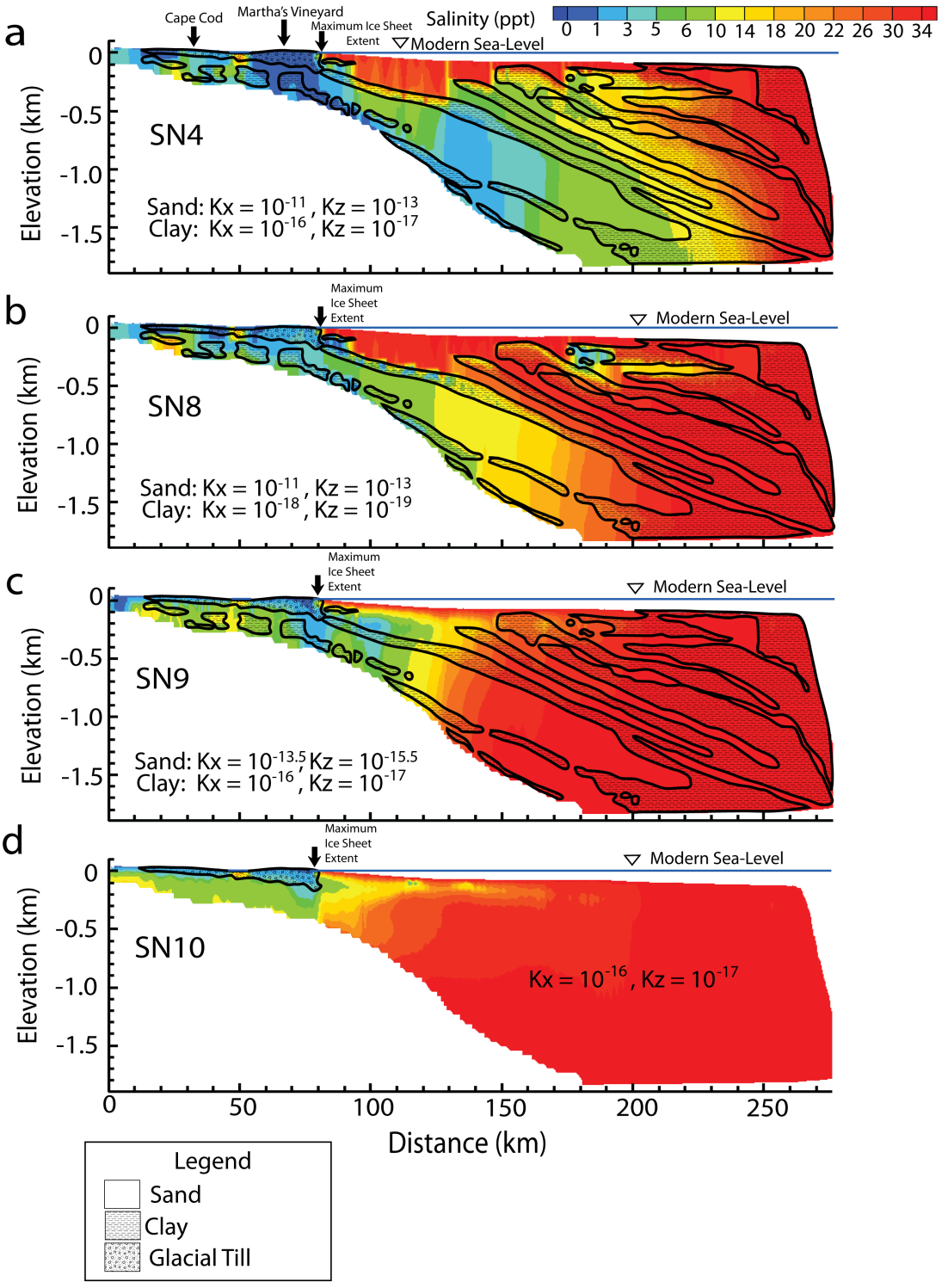

Figure 4.16: Simulated present-day salinity (ppt) distribution for a.) SN4, b.) SN8, and c.) SN9. Elevation is relative to modern sea level.

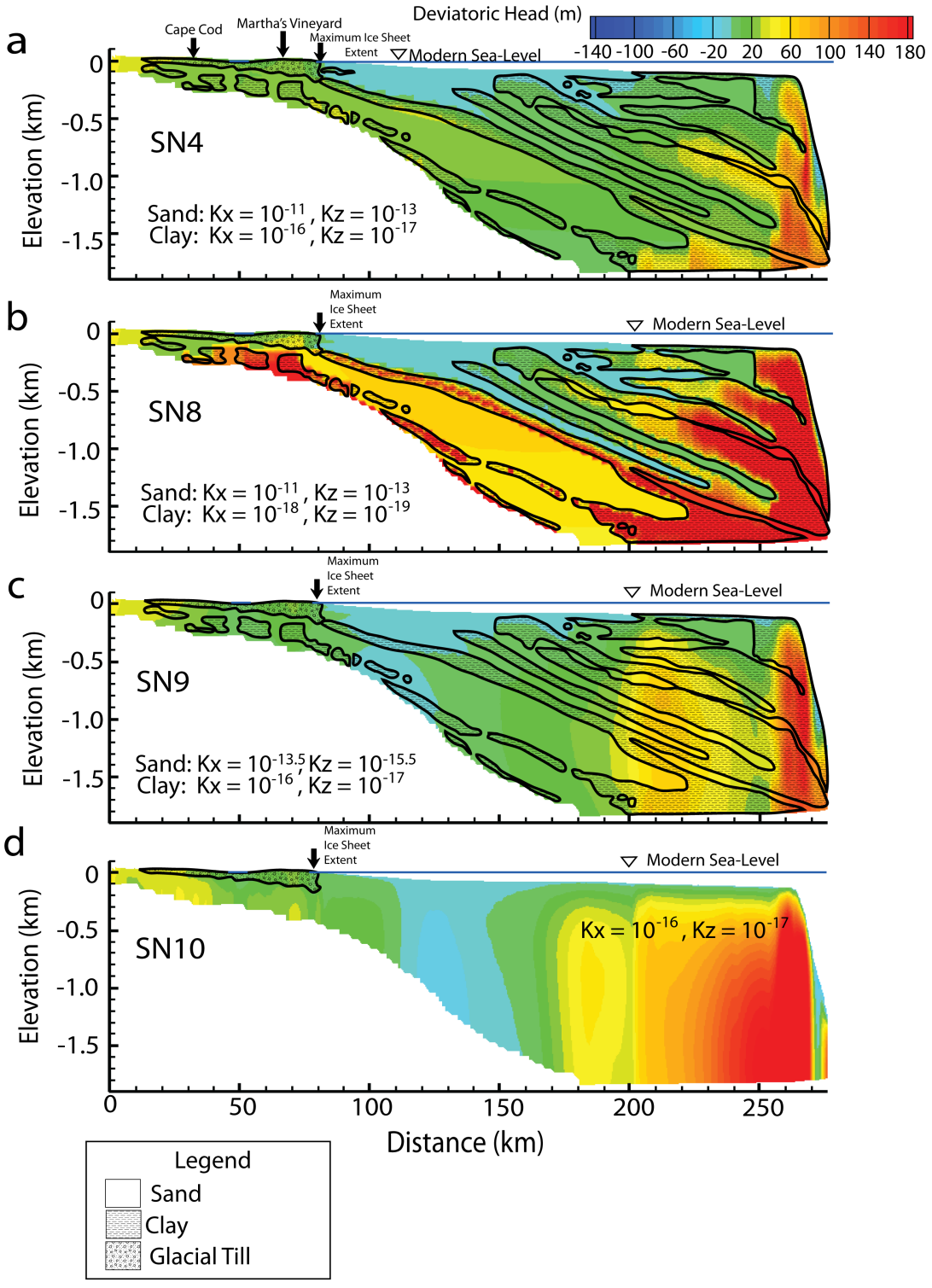

Figure 4.17: Simulated present-day deviatoric head (m) distribution for a.) SN4, b.) SN8, and c.) SN9. Elevation is relative to modern sea level.

which is generally more saline than what is simulated for SN4 (0 ppt - 3 ppt; Figures 4.4b and 4.16b). Pore fluids in shallow aquifers (between 170 and 230 km) are more fresh (by up to 3 ppt) than in SN4.

In SN9 (sand permeability decreased to $k_x = 10^{-13.5}\ m^2$ and $k_z = 10^{-15.5}\ m^2$, relative to SN4), the lateral extent of brackish water was reduced by about 50 m compared to SN4 (when comparing the 14 ppt contours in Figures 4.16a and 4.16c). The emplaced fresh water is less confined to sand aquifers and the simulated salinity under Martha's Vineyard Island is between 0 to 7 ppt salinity (Figures 4.4b and 4.16c). The percentage of brackish-to-fresh water is 5 %, 15 % less than SN4, and the percent of pore fluids with $\delta^{18}O$ less than -10 ‰ is 8 %, 15 % less than SN4 (Table 4.1). The percentage of pore fluids with a groundwater age less than 130 ky is 7 % (20 % less than SN4) and the amount greater than 1 My is 76 % (32 % greater than SN4). The homogeneous stratigraphy in SN10 produces simulated present-day salinity patterns that are similar to SN9, except the lower permeability has reduced freshwater emplacement (Figure 4.16d).

Simulated present-day hydraulic head for SN8 contains overpressures (positive deviatoric head up to 1000 m) confined within low-permeability clays near the continental shelf-slope break (Figure 4.17b). Overpressured pore fluids are also present under Martha's Vineyard Island (deviatoric head up to 200 m). In the relatively confined lower aquifer, deviatoric heads range between 55 and 65 m. Unconfined sand aquifers contain slightly underpressured heads (deviatoric heads between -1.5 and -2.0), thus are near hydrostatic. In SN4, underpressured areas (deviatoric head around -1.4 m) are only present in shallow sands and the overpressures are not as confined to the clays and confined areas as in SN9; overpressures in SN4 seem to be diffusing out of the clays. In SN9, overpressured pore fluids are present under Martha's Vineyard Island (deviatoric head

is up to 20 m) and in a large region extending from 130 km lateral distance to the continental slope (deviatoric head reaches 220 m; Figure 4.17c). These overpressured pore fluids correspond with areas that had sedimentation since 65 ka (Martha's Vineyard Island and near the shelf-slope break; Figure 3.1). An underpressured region, as low as -4 m, occurs around 110 km lateral distance. This underpressured area is a result of decreasing sea level, and associated decrease in load, between 1.1 ka and present-day. Using a homogenous stratigraphy, as in SN10, produced present-day deviatoric head patterns consistent with SN9 (Figure 4.17d). This suggests that the patterns seen in SN9 are due to the small difference in sand and clay permeability. These minor overpressured areas correspond with areas that received less significant sediment deposition, compared to areas directly adjacent to the continental slope, since 65 ka (Figure 3.1).

The simulated hydraulic head in Cretaceous sediments under Martha's Vineyard Island is 104 m for SN8 and 22 m for SN9 (Table 4.2).

4.6 Sensitivity of Simulated Present-day Salinity and Deviatoric Head Distributions to Sediment Facies Distribution (Question 6)

As discussed in Section 3.2, the exact stratigraphy of our imposed area is not known. In order to get an idea of the sensitivity of our model results to stratigraphy, we ran a simulation in which we deposited only clay during the Pleistocene (SN11), as compared to SN4 (and all the other simulations) in which we deposited approximately an equal amount of sand and clay.

Figure 4.18 contains the simulated present-day salinity patterns for SN4 and SN11. Salinity patterns under Martha's Vineyard Island and Cape Cod are very similar between SN4 and SN11 (Figure 4.18 and 4.4c). In SN11, the area

of continental shelf pore fluids that has experienced freshwater emplacement is slightly less than the area in SN4. This is at least partially due to the absence of shallow aquifers in SN11; such aquifers can be observed between 170 km and 210 km in SN4 (Figure 4.18a). However, in SN11 the percentage of pore fluids that contains brackish-to-fresh water (< 5 ppt) is 26 %, 6 % more than SN4. The plume of relatively fresh water in the deep aquifer and between 110 km and 150 km is more fresh in SN11 than SN4, reaching a minimum of 1.6 ppt in SN11 and 2 ppt in SN4. The deposited clay layer prevents displacement of fresh water that sourced from Martha's Vineyard and Cape Cod. The shallow interface (at most 300 m depth) between relatively more fresh water (about 10 ppt) and more saline water (about 20 ppt) is about 100 m thick, which is about twice as thick as the interface in SN4. In SN11, the percentage of pore fluids that have $\delta^{18}O$ less than -10 ‰ is 25 %, 2 % more than SN4 (Table 4.1). The percentage of pore fluids with a groundwater age less than 130 ky is 31 % (the 4 % more than SN4) and the amount greater than 1 My is 28 % (16 % greater than SN4).

Computed present-day deviatoric heads are shown in Figure 4.19. The simulated present-day deviatoric heads in SN11 are overall higher (more overpressured system) than SN4. In SN11, the area with deviatoric heads greater than about 50 m encompasses a dominant portion of the model domain, while hydraulic heads of this magnitude are only confined to clays adjacent to the continental slope in SN4. Simulated hydraulic heads in Cretaceous sediments under Martha's Vineyard Island are about 56 m above msl for SN11, 25 m greater than SN4. This is due to the blanketing effects of the deposited clays. SN11 also contains an underpressured area (deviatoric head as low as -3 m) in the shallow portion of the mesh near the continental shelf-slope break (250 km), where the sedimentation rate was low (Figure 3.1). In SN11, the present-day groundwater flow in the continental shelf sediments is towards the shoreline.

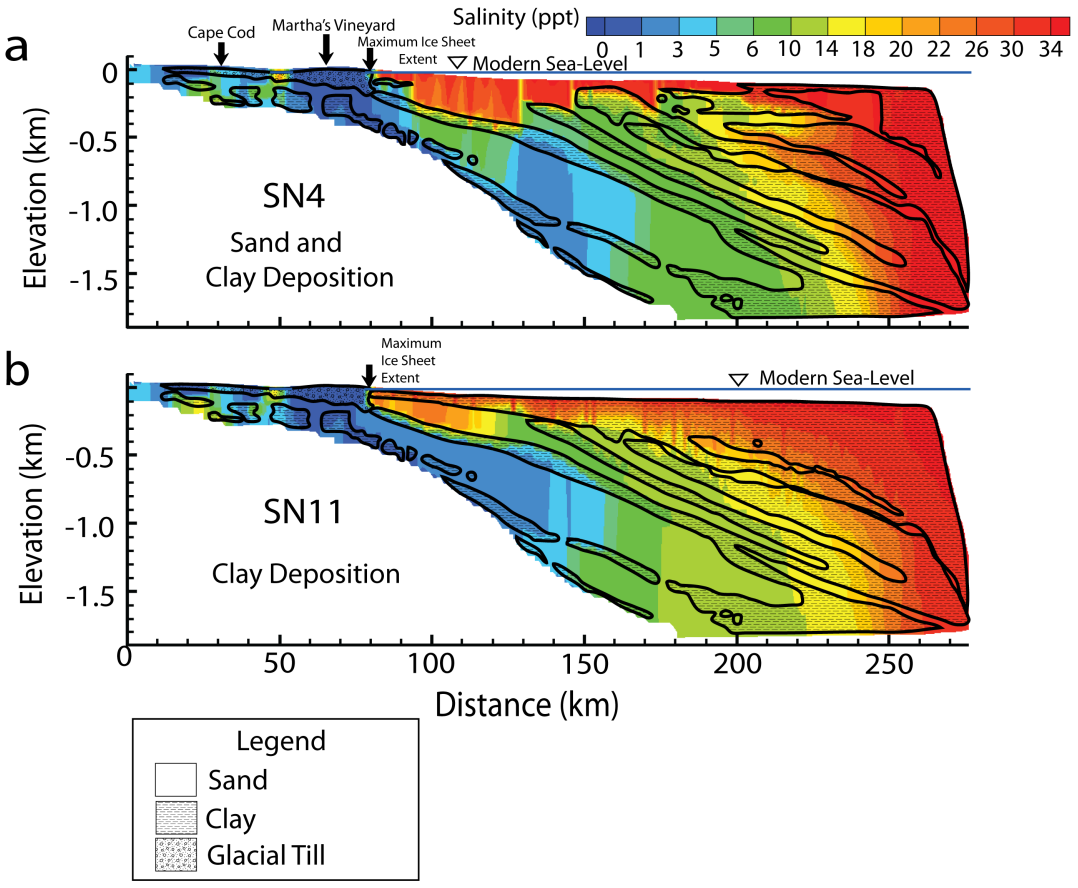

Figure 4.18: Comparison of simulated present-day salinity (ppt) distribution for a.) SN4 and b.) SN11. Scenario SN11 represents deposition of only clays while SN4 represents both sand and clay deposition. Elevation is relative to modern sea level.

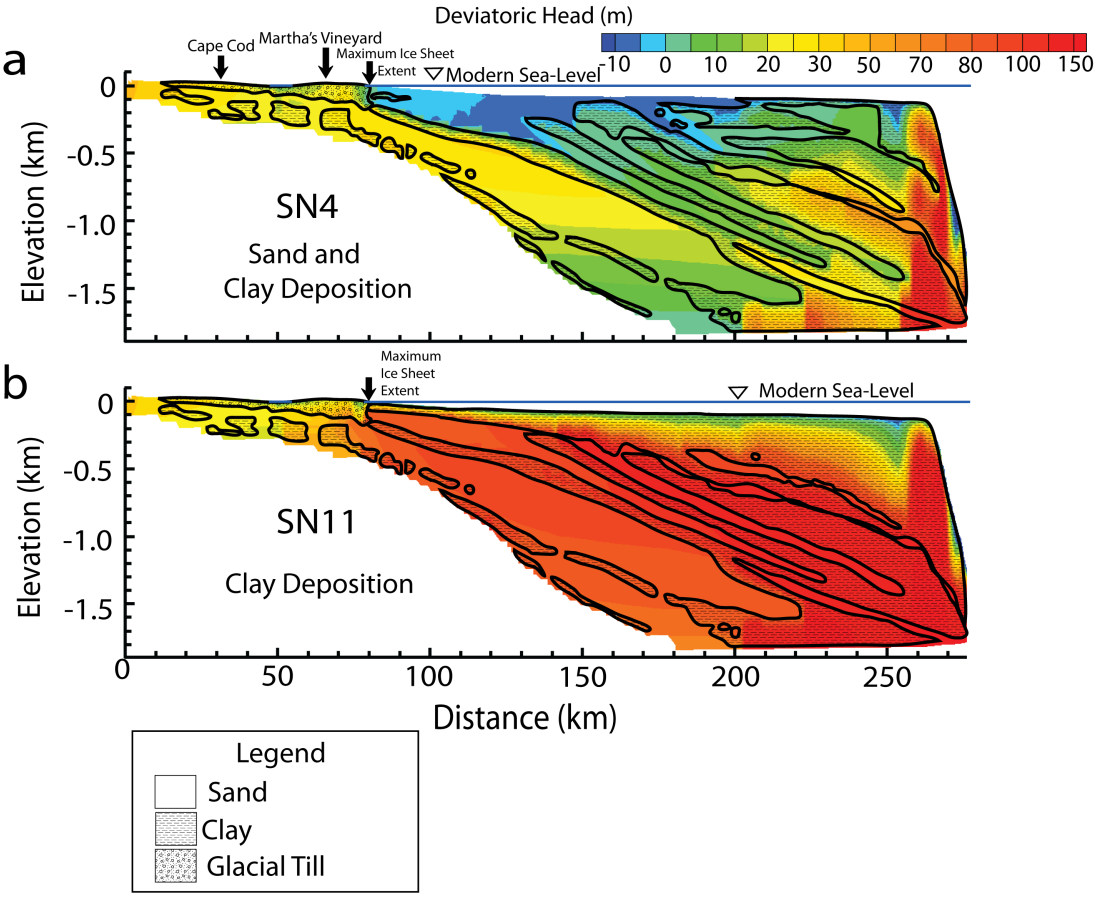

Figure 4.19: Comparison of simulated present-day deviatoric head (m) distribution for a.) SN4 and b.) SN11. Scenario SN11 represents deposition of only clays while SN4 represents both sand and clay deposition. Elevation is relative to modern sea level.

CHAPTER 5

DISCUSSION

Assuming that the permeability values we used for sands (k_x=10^{-11} m^2 and k_z=10^{-13} m^2), clays (k_x=10^{-16} m^2 and k_z=10^{-17} m^2), and tills (10^{-16} m^2 and k_z=10^{-16} m^2) are representative, we found that (1) sediment loading and (2) sea-level fluctuations had dominant control on the present-day deviatoric head distribution on the continental shelf offshore of Martha's Vineyard Island. Sediment loading produced overpressures (up to 180 m) in the low permeability clays, as well as underpressures (as low as -20 m) in regions that experienced erosion and little sedimentation (Figure 4.1a). Sea-level fluctuations induced modest underpressures reducing heads in basal sand units (Figure 4.1b). Sea-level fluctuations also induced overpressures in clay adjacent to the continental slope, but to a minor degree compared to sediment loading.

We found that for the simulations that represented the ice sheet (SN4, ice sheet maximum extent to Martha's Vineyard, and SN6, ice sheet maximum extent to the continental shelf-slope break), glacial loading dominated over all other fluid flow impelling mechanisms during ice sheet maxima, increasing the deviatoric hydraulic head by as much as 0.9 km (during Wisconsin glaciation) to 1.3 km (during Illinoian glaciation in SN6) relative to conditions with no ice sheet. However, fossil overpressures from the Illinoian are not preserved in the present-day system (SN4 and SN6; Figure 4.6). Computed heads from both ice sheet models

are similar to the simulation with no ice sheet (SN1). This indicates that the high permeability of the relatively thick clay units near the continental slope result in little memory of Wisconsin and pre-Wisconsin glaciations. We expected that the simulated present-day hydraulic heads to be larger for the simulation in which the ice sheet extended to the continental shelf-slope break (SN6) than the simulation in which the ice sheet only extended to Martha's Vineyard Island (SN4).

For the three ice sheet simulations, computed pore pressures in Cretaceous sediments under Martha's Vineyard Island (SN1, 23 m, SN4, 31 m, and SN6, 31 m above modern sea level) were 3-4 times greater than observed excess pressures beneath Nantucket Island (7.5 m). Again, these simulated pore pressures were overall relatively similar. These values were also relatively consistent with the simulation in which we only implemented sea-level variation (SN3, 22 m above sea level). Pore-pressure measurements made further offshore in clay/silt rich facies would go a long way towards narrowing down past glacial dynamics. Further, when we increased the sand permeability (k_x=$10^{-13.5}$ m^2 and k_z=$10^{-15.5}$ m^2; SN9), simulated hydraulic heads were consistent with the lower permeability scenarios (22 m above modern sea level). The simulated pore pressures in this same area increase by a factor of 4 (104 m above modern sea level; Table 4.2) when clay permeabilities were decreased (k_x=10^{-18} m^2 and k_z=10^{-19} m^2; SN8) and increased by a factor of 2 (to 56 m above modern sea level) when we used clay-rich Pleistocene stratigraphy. Based on this information, it is reasonable to exclude the low clay permeability (k_x=10^{-18} m^2 and k_z=10^{-19} m^2) as representative of actual conditions. However, more hydraulic head data from deeper offshore wells is needed to further constrain offshore stratigraphy and permeability.

Using homogenous sand and clay permeability (SN10) produced simulated present-day salinity patterns that resembled the classical steady state sea-

water intrusion model (Figures 4.3a and 4.16d). We speculate that if the permeability was still homogeneous, but substantially higher (k_x = 10^{-9} m^2 and k_z = 10^{-10} m^2) then the simulated present-day patterns would be more similar to the classical model, with even less simulated present-day fresh water. Sediment heterogeneity had an important role in creating the conditions that lead to the sequestration of freshwater offshore. Higher permeability units allowed for greater infiltration of fresh water and the lower permeability prevented displacement of fresh water with seawater. The greater difference in sand and clay permeability tended to allow for the greatest amount of simulated fresh water sequestered offshore (Figure 4.16b). In general, it is not only the hydraulic permeability but the heterogeneity (patterns and relative values) that matters in offshore freshwater sequestration.

Decreasing the permeability of either the clay (SN8; k_x = 10^{-18} m^2 and k_y = 10^{-19} m^2) or the sand (SN9; k_x = $10^{-13.5}$ m^2 and k_y = $10^{-15.5}$ m^2), or using a clay-rich Pleistocene stratigraphy (SN11), drastically affected the anomalous offshore pore pressures. Decreasing the permeability of only the clay (SN8) resulted in dominantly overpressured areas in the clays and deep aquifer, with slightly underpressured to nearly hydrostatic conditions (-2 m deviatoric head) in the exposed sand aquifers (Figure 4.17b). Decreasing the permeability of the sand (SN9), resulting in a system with nearly homogenous permeability, produced a greater propensity to have large overpressured areas, with little differentiation between clay and sand. Small regions containing underpressured sediment were confined to the areas that had little recent sedimentation, or at least more substantial erosion than sedimentation (between 80 and 150 km lateral distance; Figures 4.17c and 3.1). The clay-rich Pleistocene stratigraphy (SN11) also contained high

overpressures that encompassed the whole offshore region. These high overpressures induced by a combination of ice sheet, sediment, and sea-level loading would have otherwise more readily diffused out in lower permeability and more sand rich stratigraphy.

As mentioned above, the presence of the ice sheet drastically increased shore-normal head gradients and freshwater emplacement. Simulations in which the ice sheet extent was varied (no ice sheet; SN1; ice sheet terminating at Martha's Vineyard Island, SN4; ice sheet to the continental shelf-slope break, SN6) indicated that implementation of the ice sheet resulted in greater emplacement of brackish-to-fresh water due to forced advection and dispersion of fresh water through low permeability clays (Figure 4.3). It is possible that grid dispersion promoted greater extention of brackish-to-fresh water emplacement. Dispersion was probably enhanced by our representing the effects of the ice sheet for each Pleistocene glacial period (over 50 glacial periods since 2.75 ka). In earlier models, typically only one to two glacial cycles have been taken into account. The repeated advancements caused greater dispersion of fresh water into the lower permeability clays further offshore and less confinement of fresh water to aquifers, as was used in continental shelf models by Marksamer et al. (2007) and Person et al. (2003).

The presence of the ice sheet increased surface infiltration all along the continental shelf, by up to an order of magnitude. There was also reversal of groundwater flow upon removal of the ice sheet (Figures 4.9, 4.10, and 4.11) (Grasby et al., 2000; Lemieux et al., 2008b). The percentage of brackish-to-fresh pore fluids (< 5 ppt) increased by 6 % with implementation of the ice sheet that only extended to Martha's Vineyard. For the scenario in which the ice sheet

reached the continental shelf-slope break (SN6), it lingered on the continental shelf longer and increased the percentage of brackish-to-fresh pore fluids (< 5 ppt) in the continental shelf by 17 % (Table 4.1) . However, we found that all three models (SN1, SN4, and SN6) had close to identical salinity patterns under Martha's Vineyard. (Figure 4.4a). Decreasing the permeability of the clays (SN9) or the sands (SN8) resulted in slightly more saline pore fluids beneath Martha's Vineyard, and all along the continental shelf (the percentage of pore fluids < 5 ppt decreased by 12 % in SN8 and 15 % in SN9, relative to SN4).

To our surprise, flexural adjustments to the lithosphere caused submergence of the land surface below sea-level, resulting in saltwater encroachment after the ice sheet retreated. To some degree this worked against freshwater emplacement. This mechanism caused the simulated pore fluids under Martha's Vineyard Island to be more saline for the low permeability scenarios in which the maximum ice sheet extent was to Martha's Vineyard (SN8 and SN9; Figure 4.4b), and much more saline conditions under Cape Cod for all the simulations in which the ice sheet was represented (Figures 4.3 and 4.16).

Salinity data was available from relatively deep wells on Nantucket Island (USGS 6001, 500 m deep) and Martha's Vineyard (ENW-50, 250 m deep) to provide ground truth for our models. Unfortunately, these wells are restricted to the nearshore environments and, like the hydraulic head data, provided little help in constraining hydrogeologic parameters. Model results suggest that deep ($>$ 1000 m) aquifers, 90 - 130 km offshore should host brackish-to-fresh waters. Currently, future drilling is proposed to occur to a maximum of 800 m depth along the continental shelf (Figure 5.1). This depth should be sufficient, in all simulations, to capture meteoric and glacial meltwater within shallow continental shelf

pore fluids and deeper sediments. However, extending drilling to 1.3 km depth would allow us to better understand the extent of freshwater penetration. Since continental shelf stratigraphy and permeability used in our models (as well as ice sheet loading and extent) are all uncertain, wells should be sited taking into account the bulk of our results produced by this sensitivity study.

Since the ice sheet was only present on the continental shelf about 12 % of the Pleistocene in our models, implementation of the ice sheet had little influence on surface vertical flux patterns during interglacial periods (infiltration and discharge patterns for SN1, SN4, and SN6 were nearly identical during these periods). As similarly noted by Lemieux et al. (2008), we found that at any time in our simulation the infiltration and discharge are likely not in equilibrium with current sea-level condition. The waxing and waning of the ice sheet and the rising and falling of sea-level produced ever-changing boundary conditions and delayed transient response of the system, resulting in a system that has highly transient surface flux. It is clear that dynamic equilibrium does not exists for salinity transport in our simulations, since climate and geology change is not deterministically periodic.

Free convection, often expressed as fingering, in permeable strata is a common effect of density instabilities brought about by seawater overlapping fresh pore fluid. It has been considered for systems off the coast of Florida (Kooi and Groen, 2001) and Suriname (Groen et al., 2000). In our higher permeability simulations (SN1, SN4, and SN6) free convection controlled pore-fluid chemistry in the shallow, offshore environment (between 90 - 130 km offshore), that experienced repeated transgressions throughout the Pleistocene. Clay-rich Pleistocene sediments prevented fingering of seawater and displacement of fresh water, resulting in larger areas with brackish-to-fresh water (< 5 ppt, increased by 6 %

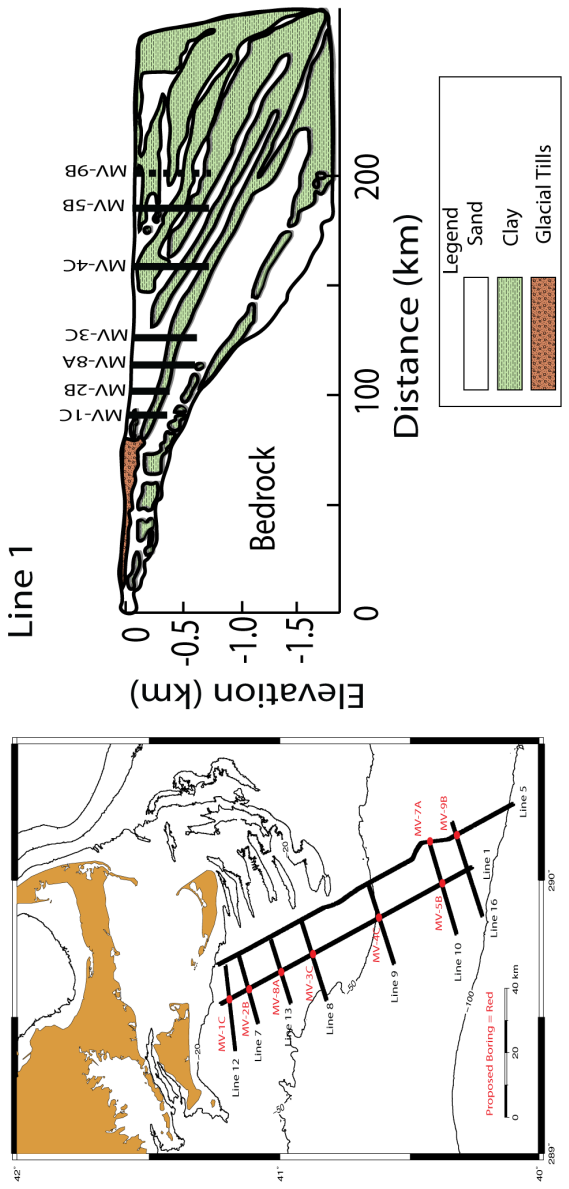

Figure 5.1: Proposed drilling locations (MV-#) offshore of Martha's Vineyard Island and how they correspond with our cross-section. Lines on the map represent seismic lines taken during our geophysical survey (EN-465). The vertical black lines indicate the current proposed borehole depths.

relative to SN4) and pore fluids with $\delta^{18}O$ less than -10 ‰(increased by 2 % compared to SN4).

In our simulations in which we implemented the ice sheet (SN4 and SN6), surprisingly few pore fluids contained $\delta^{18}O$ signatures near the glacial end member (-20 ‰; Figure 4.5). This is predominantly due to a high component of mixing. Even so, the percentage of pore fluids that contained $\delta^{18}O$ less than -10 ‰ (the meteoric water end member) is 23 % (SN4) to 77 % (SN6). The absence of an ice sheet end member is a common observation in many continental sedimentary basins that have been glaciated (Ma et al., 2004; McIntosh and Walter, 2005). Thus, our numerical results are not surprising.

The degree of mixing is further emphasized by the distribution of groundwater ages. For the simulations in which we implemented the ice sheet (SN4 and SN6), about 19 to 23 % of pore fluids had mean groundwater ages less than or equal to the 50 *ky* (maximum carbon dating age) and 27 to 33 % of pore fluids had mean groundwater ages from the last two interglacials (130 *ka*). This would mean that 67 to 73 % of the pore fluids have groundwater ages greater than 130 *ky*. Most of the continental shelf experienced some type of emplacement of fresh water since 130 *ka*, but mixing with older water in our simulations diminished the signature (Figure 4.8). These contour maps of simulated residence times can be used in selecting offshore well locations that can be dated using ^{14}C methods (ages < 50 *ky*).

Most paleo-hydrogeologic models of the Pleistocene neglect the effects of sediment deposition and erosion (Lemieux et al., 2008b; Person et al., 2003); representing them in our models had significant effects on present-day salinity and pore-pressure patterns. Using the modern stratigraphy for the entire Pleistocene

did not accurately account for transient changes in sea-floor topography. In our simulations, during the Wisconsin glaciation (about 20 *ka*) sea level lowered below the crest of clinoform development (Figure 4.7). The simulated aerially exposed clinoform produced a local high head gradient, which focused meteoric water deep into an adjacent shallow aquifer (between 170 and 240 *km* lateral distance; Figure 4.13a). The extent of freshwater emplacement into this aquifer was diminished in the static simulation due to the absence of this local topographic gradient (SN7; Figure 4.13b). Interestingly, there was greater emplacement of fresh water in the simulation that neglected sedimentation and erosion. We expected that the presence of shallow Wisconsin tills over Cape Cod and Martha's Vineyard throughout the entire simulation would have blocked meltwater and overall freshwater infiltration. However, overpressures induced by sedimentation retarded influx of fresh water (Figure 4.14). This indicates that anomalous heads due to sedimentation moderated infiltration patterns. This mechanism seems to have been more important than the surface permeability in our relatively high permeability system.

There are three implications to this research, some that reiterate the work of others. First, that passive continental shelf margins are a potential source of brackish-to-fresh water for coastal cities that may be in need of water resources in the future (Cohen et al., 2010). Second, the presence of the ice-sheet is not necessary to induce freshwater infiltration into continental shelf sediments. Third, the potential amount of brackish-to-fresh water sequestered offshore Martha's Vineyard Island drastically increases, by almost a factor of two, with the added new understanding that the Laurentide ice sheet may have reached to the continental shelf-slope break.

Low-latitude coastal environments likely experienced freshwater infiltration during sea-level low-stands. Brackish-to-fresh water contained within the coastal sediments could be a very important water resource for low-lattitude populous coastal countries, such as Singapore. Some populous countries are on the down stream portion of the rivers and thus have need of their own freshwater source. Testing the viability of tapping into this offshore coastal water resource would need to be conducted by a country that has sufficient financial resources and freshwater demand.

Further, even though the ice sheet is only present on the continental shelf for a small portion of the Pleistocene, increased infiltration due to the ice sheet suggests that the presence of ice sheet meltwater along the continental shelf could be influencing coastal biomes. Glacial meltwater coming from mountain glaciers along the Gulf of Alaska contained high bioavailable dissolved organic carbon (DOC) and older ^{14}C ages compared to stream water (Hood et al., 2009). Further, McIntosh et al. (2002) noted that infiltration of glacial meltwater within the Michigan basin promoted microbiological reactions in organic rich shale deposits, leading to the generation of economically significant quantities of natural gas. With this information, it is possible that these coastal areas once affected by an ice sheet may have unknown petroleum reserves. However, it also brings to question why petroleum resources were not found in Georges Bank and more places along the New England continental margin.

CHAPTER 6

CONCLUSION

In this study, we attempted to better understand the mechanisms controlling pore-pressure, salinity, isotope ($\delta^{18}O$), and groundwater age distribution on the Atlantic continental shelf offshore of Martha's Vineyard Island by using cross-sectional mathematical modeling and the finite-element method to simulate continental-shelf paleo-hydrology through the Pleistocene (2.75 *Ma* - present-day). The study was motivated by new high resolution multi-channel seismic data that was collected in 2009, in support of a proposed IODP drilling campaign. Specifically, we attempted to understand how fluid-flow driving forces (compaction, density instabilities, and topography driven flow), ice-sheet loading, ice-sheet maximum extent, permeability, and Pleistocene stratigraphy affects fresh-water and deviatoric head distribution. This included using simulations with an evolving mesh that took into account Pleistocene sedimentation, erosion, and subsidence. We used salinity, $\delta^{18}O$, groundwater age, and hydraulic head data from Martha's Vineyard Island and Nantucket Island provided some degree of ground truth to constrain our models.

We found that sedimentation, sea-level fluctuation, and ice-sheet loading controlled present-day freshwater distribution. Overpressures (up to 180 m) induced by sedimentation retarded freshwater influx, while sea-level low-stands and ice-sheet loading produced shore-normal gradients (0.0005 and 0.00416 m/m,

respectively) that focused fresh water into continental-shelf sediments. A more expansive ice sheet (extending out to the continental shelf-slope break; shore-normal gradient of 0.0055 m/m) nearly doubled the percentage of emplaced simulated present-day brackish-to-fresh water (< 5 ppt; increased from 20 % to 37 % of continental-shelf pore fluids) compared to simulations in which the ice sheet extended to Martha's Vineyard. Sand and clay distribution and permeability played an essential role in freshwater infiltration; an approximately equal distribution of sand and clay, and a greater difference in sand and clay permeability resulted in the greatest preservation of brackish-to-fresh pore fluids. However, onshore pore fluids are not highly sensitive to ice-sheet extent nor sand and clay permeability.

Our results and sensitivity study indicate that offshore sediment data is needed to adequately simulate continental-shelf paleo-hydrogeology. Onshore hydrology is dominantly controlled by present-day conditions and thus shows little to no record of Pleistocene ice sheet influence. Further, proposed bore-hole depths may need to be deepened (possibly to 1.3 km) to ensure encountering brackish-to-fresh pore fluids.

REFERENCES

Amato, R. V. and Bebout, J. W. (1980). Geologic and Operational Summary, Cost No. G-1 Well, Georges Bank Area, North Atlantic OCS. Open File Report 80-268, United States Department of the Interior, Geological Survey.

Amato, R. V. and Simonis, E. K. (1980). Geologic and Operational Summary, Cost No. G-2 Well, Georges Bank Area, North Atlantic OCS. Open File Report 80-269, United States Department of the Interior, Geological Survey.

Anderson, R. S., Miller, N. G., Davis, R. B., and Nelson, R. E. (1990). Terrestrial fossils in the marine Presumpscot Formation: implications for Late Wisconsinan paleoenvironments and isostatic rebound along the coast of Maine. *Canadian Journal of Earth Science*, 27:1241–1246.

Balco, G. and Rovey, C. W. (2010). Absolute chronology for major Pleistocene advances of the Laurentide Ice Sheet. *Geology*, 38(9):795–798.

Balco, G., Stone, J. O., Porter, S. C., and Caffee, M. W. (2002). Cosmogenic-nuclide ages for New England coastal moraines, Martha's Vineyard and Cape Cod, Massachusetts, USA. *Quaternary Science Reviews*, 21:2127–2135.

Barnhardt, W. A., Gehrels, W. R., and Kelley, J. T. (1995). Late Quaternary relative sea-level change in the western Gulf of Maine: Evidence for migrating glacial forebulge. *Geology*, 23:317–320.

Bense, V. F. and Person, M. (2008). Transient hydrodynamics within intercratonic sedimentary basins during glacial cycles. *Journal of Geophysical Research*, 113:F04005.

Bethke, C. M. (1986). Inverse hydrologic analysis of the distribution and origin of Gulf Coast-type geopressured zones. *Journal of Geophysical Research*, 91:6535–6545.

Bethke, C. M. and Corbet, T. F. (1988). Linear and nonlinear solutions for one-dimensional compaction flow in sedimentary basins. *Water Resource Research*, 24:461–467.

Bintanja, R., van de Wal, R., and Oerlemans, J. (2005). Modelled atmospheric temperatures and global sea levels over the past million years. *Nature*, 437:125–128.

Blum, P., Xu, J., and Donthireddy, S. (1996). 21. Geotechnical properties of Pleistocene sediments from the New Jersey upper continental slope. *Proceedings of the Ocean Drilling Program Scientific Results*, 150:377–384.

Bowman, J., Willett, S., and Cook, S. (1994). Oxygen isotopic transport and exchange during fluid flow: One-dimensional models and applications. *American Journal of Science*, 294:1–55.

Breckenridge, A., Johnson, T. C., Beske-Dlehl, S., and Mothersill, J. S. (2004). The timing of regional Lateglaical events and post-glacial sedimentation rates for Lake Superior. *Quaternary Science Reviews*, 23:2355–2367.

Buxton, H. T. and Modica, E. (1992). Patterns and Rates of Ground-Water Flow on Long Island, New York. *Ground Water*, 30:857–866.

Christie-Blick, N. (1991). Onlap, offlap, and the origin of unconformity-bounded depositional sequences. *Marine Geology*, 97:35–56.

Cohen, D., Person, M., Wang, P., Gable, C. W., Hutchinson, D., Marksamer, A., Dugan, B., Kooi, H., Groen, K., Lizarralde, D., Evans, R. L., Day-Lewis, F. D., and Lane, J. W. (2010). Origin and extent of fresh paleowaters on the Atlantic Continental Shelf, USA. *Ground Water*, 48:143–158.

Criss, C., Gregory, R. T., and Taylor, H. P. (1987). Kinetic theory of oxygen isotope exchange between minerals and water. *Geochimica et Cosmochimica Acta*, 51:1108–1108.

Cuffey, K. M. and Clow, G. D. (1997). Temperature, accumulation, and ice sheet elevation in central Greenland through the last deglacial transition. *Journal of Geophysical Research*, 102:26383–26396.

Dugan, B. and Flemings, P. (2002). Fluid flow and stability of the US continental slope offshore New Jersey from the Pleistocene to the present. *Geofluids*, 2:137–146.

Dugan, B. and Flemings, P. B. (2000). Overpressure and Fluid Flow in the New Jersey Continental Slope: Implications for Slope Failure and Cold Seeps. *Science*, 289:288–291.

Dutton, A., Bard, E., Antonioli, F., Esat, T., Lambeck, K., and McCulloch, M. (2009). Phasing and amplitude of sea-level and climate change during the penultimate interglacial. *Nature Geoscience*, 2:355–359.

Dyke, A., Andrews, J., Clark, P., England, J., Miller, G., Shaw, J., and Veillette, J. (2002). The Laurentide and Innuitian ice sheets during the Last Glacial Maximum. *Quaternary Science Reviews*, 21:9–31.

Edmunds, W. M., Hinsby, K., Marlin, C., Condesso de Melo, M. T., Manzano, M., Vaikmae, R., and Travi, Y. (2001). Evolution of groundwater systems at the European coastline. In Edmunds, W. M. and Milne, C. J., editors, *Paleowaters in Coastal Europe: evolution of groundwater since the Late Pleistocene*, number 189 in Special Publications, pages 289–311. The Geological Society, London.

Engelhardt, H. and Kamb, B. (1997). Basal hydraulic system of a West Antarctic ice stream: Constraints from borehole observations. *Journal of Glaciology*, 43:207–230.

Feehley, C. E., Zheng, C., and Molz, F. J. (2000). A dual-domain mass transfer approach for modeling solute transport in heterogeneous aquifers: Application to the Macrodispersion Experiment (MADE) site. *Water Resource Research*, 36:2501–2515.

Flowers, G., Marshall, S., Bjornsson, H., and Clarke, G. (2005). Sensitivity of Vatnajokull ice cap hydrology and dynamics to climate warming over the next 2 centuries. *Journal of Geophysical Research*, 110:F02011.

Folger, D., Hathaway, J., Christopher, R., Valentine, P., and Poag, C. (1978). Stratigraphic test well, Nantucket Island, Massachusetts. U.S. Geological Survey Circular C 773, 28, U.S. Geological Survey.

Freeze, A. R. and Cherry, J. A. (1979). *Groundwater*. Prentice Hall, Englewood Cliffs, New Jersey.

Fulthorpe, C. S. and Austin, J. A. (2008). Assessing the significance of alongstrike variations of middle to late Miocene prograding clinoformal sequence geometries beneath the New Jersey continental shelf. *Basin Research*, 20:269–283.

Gale, A. S., Hardenbol, J., Hathway, B., Kennedy, W. J., Young, J. R., and Phansalkar, V. (2002). Global correlation of Cenomanian (Upper Cretaceous) sequences: Evidence for Milankovitch control on sea level. *Geology*, 30:291–294.

Garrison, L. E. (1970). Development of Continental Shelf South of New England. *The American Association of Petroleum Geologists Bulletin*, 54:109–124.

Garven, G. and Freeze, R. (1984). Theoretical analysis of the role of groundwater flow in the genesis of stratabound ore deposits; 1, Mathematical and numerical model. *American Journal of Science*, 284:1085–1124.

Goode, D. J. (1996). Direct simulation of groundwater age. *Water Resource Research*, 32:289–296.

Grasby, S., Osadetz, K., Betcher, R., and Render, F. (2000). Reversal of the regional-scale flow system of the Williston basin in response to Pleistocene glaciation. *Geology*, 28:635–638.

Groen, J., Velstra, J., and Meesters, A. (2000). Salinization processes in paleowaters in coastal sediments of Suriname: evidence from $\delta^{37}Cl$ analysis and diffusion modelling. *Journal of Hydrology*, 234:1–20.

Gustavson, T. C. (1976). Paleotemperature analysis of the marine Pleistocene of Long Island, New York, and Nantucket Island, Massachusetts. *Geological Society of American Bulletin*, 87:1–8.

Guswa, J. H. and LeBlanc, D. R. (1985). Digital Models of Ground-Water Flow in the Cape Cod Aquifer System, Massachusetts. Water-Supply Paper 2209, U.S. Geological Survey.

Gutierrez, B., Uchupi, E., Driscoll, N., and Aubrey, D. (2003). Relative sea-level rise and the development of valley-fill and shallow-water sequences in Nantucket Sound, Massachusetts. *Marine Geology*, 193:295–314.

Hall, R., Poppe, L., and Ferrebee, W. (1980). A stratigraphic test well, Martha's Vineyard, Massachusetts. Geological Survey Bulletin 1488, U.S. Geological Survey.

Haq, B. U., Hardenbol, J., and Vail, P. R. (1987). Chronology of Fluctuating Sea Levels Since the Triassic. *Science*, 235:1156–1167.

Hathaway, J. (1981). Data file the 1976 Atlantic Margin Coring (AMCOR) Project of the U.S. Geological Survey. Open File Report 81-239, U.S. Geological Survey.

Hathaway, J., Poag, C., Valentine, P., Miller, R., Schultz, D., Manheim, F., Kohout, F., Bothner, M., and Sangrey, D. (1979). U.S. Geological Survey core drilling on the Atlantic shelf. *Science*, 206:515–527.

Hendry, M. J. (1982). Hydraulic Conductivity of Glacial Till in Alberta. *Ground Water*, 20:162–169.

Hetenyi, M. (1946). *Beams on Elastic Foundations Theory with Applications in the Fields of Civil and Mechanical Engineering*. The University of Michigan Press.

Hood, E., Fellman, J., Spencer, R., Hernes, P., Edwards, R., D'Amore, D., and Scott, D. (2009). Glaciers as a source of ancient and labile organic matter to the marine environment. *Nature*, 462:1044–1047.

Hooke, R. (1998). *Principles of Glacier Mechanics*. Prentice Hall, Upper Saddle, New Jersey.

Hooyer, T. S. and Iverson, N. R. (2002). Flow mechanism of the Des Moines Lobe of the Laurentide Ice Sheet. *Journal of Glaciology*, 48:575–586.

Hubbert, M. (1940). The theory of ground-water motion. *Journal of Geology*, 48:785–944.

Hubbert, M. K. and Rubey, W. W. (1959). Role of fluid pressure in mechanics of overthrust faulting I. Mechanics of fluid-filled porous solids and its application to overthrust faulting. *The Geological Society of American Bulletin*, 70:115–166.

Hughes, T. J., Denton, G. H., Andersen, B. G., Schilling, D. H., Fastook, J. J., and Lingle, G. S. (1981). The Last Great Ice Sheets: A Global View. In Denton, G. H. and Hughes, T. J., editors, *The Last Great Ice Sheets*, pages 263–317. Jon Wiley and Sons, Inc., New York.

Johnston, R. (1983). The saltwater-freshwater interface in the Tertiary limestone aquifer, southeast Atlantic outer-continental shelf of the U.S.A. *Journal of Hydrology*, 61:239–249.

Kawamura, K., Parrenin, F., Lisiecki, L., Uemura, R., Vimeux, F., Severinghaus, J., Hutterli, M., Nakazawa, T., Aoki, S., Jouzel, J., Raymo, M. ., Matsumoto, K., Nakata, H., Motoyama, H., Fujita, S., Goto-Azuma, K., Fujii, Y., and Watanabe, O. (2007). Northern Hemisphere forcing of climatic cycles in Antarctica over the past 360,000 years. *Nature*, 448:912–916.

Kaye, C. A. (1964). Outline of Pleistocene Geology of Martha's Vineyard, Massachusetts. Professional Paper 501-C, U.S. Geological Survey.

Kestin, J., Khalifa, H. E., and Correia, R. J. (1981). Tables of the Dynamics and Kinematic Viscosity of Aqueous NaCl Solutions in the Temperature Range 20-150 ^oC and the Pressure Range 0.1-35 MPa. *Journal of Physical Chemistry Reference Data*, 10:71–87.

Klitgord, K., Poag, P., Schneider, C., and North, L. (1994). Geophysical database of the East Coast of the United States northern Atlantic margin—cross sections and gridded database (Georges Bank Basin, Long Island Platform, and Baltimore Canyon Trough). Open File Report 94-637, U.S. Geological Survey.

Kohout, F. A., Hathaway, J. C., Folger, D., Bothner, M., Walker, E. H., Delaney, D. F., Frimpter, M. H., Weed, E. G. A., and Rhodehamel, E. C. (1977). Fresh ground water stored in aquifers under the continental shelf: Implications from a deep test, Nantucket Island, Massachusetts. *Water Resource Bulletin*, 13:373–386.

Konikow, L. and Grove, D. (1977). Derivation of equations describing solute transport in ground water. Resources Investigations 77-19, U.S. Geological Survey Water.

Kooi, H. and Groen, J. (2001). Offshore continuation of coastal groundwater systems; predictions using sharp-interface approximations and variable-density flow modeling. *Journal of Hydrology*, 246:19–35.

Kooi, H. and Groen, J. (2003). Geological processes and the management of groundwater resources in coastal areas. *Netherlands Journal of Geosciences / Geologie en Mijnbouw*, 82:31–40.

Larsen, H. C., Dahl-Jensen, T., and Hooper, J. R. (1998). 39. Crustal structure along the leg 152 drilling transect. *Proceedings of the Ocean Drilling Program Scientific Results*, 152:463–475.

Le Brocq, A., Payne, A., Siegert, M., and Alley, R. (2009). A subglacial water-flow model for West Antarctica. *Journal of Glaciology*, 55:879–888.

Le Meur, E. and Huybrechts, P. (1996). A comparison of different ways of dealing with isostasy: examples from modelling the Antarctic ice sheet during the last glacial cycle. *Annals of Glaciology*, 23:309–317.

Lemieux, J.-M., Sudicky, E., Peltier, W., and Tarasov, L. (2008a). Dynamics of groundwater recharge and seepage over the Canadian landscape during the Wisconsinian glaciation. *Journal of Geophysical Research*, 113:F01011.

Lemieux, J.-M., Sudicky, E., Peltier, W., and Tarasov, L. (2008b). Simulating the impact of glaciations on continental groundwater flow systems: 2. Model application on the Wisconsinian glaciation over the Canadian landscape. *Journal of Geophysical Research*, 113:F03018.

Lemieux, J.-M. and Sudicky, E. A. (2010). Simulation of groundwater age evolution during the Wisconsinian glaciation over the Canadian landscape. *Environmental Fluid Mechanics*, 10:91–102.

Ma, L., Castro, M. C., and Hall, C. M. (2004). A late Pleistocene-Holocene noble gas paleotemperature record in southern Michigan. *Geophysical Research Letters*, 31:L23204.

Mailloux, B., Person, M., Stayer, P., Hudleston, P., Cather, S., and Dunbar, N. (1999). Tectonic and stratigraphic controls on the hydrothermal evolution of the Rio Grande Rift. *Water Resource Research*, 35:2641–2659.

Manzano, M., Custodio, E., Loosli, H., Cabrera, M., Riera, X., and Custodio, J. (2001). Paleowater in coastal aquifers in Spain. In Edmunds, W. M. and Milne, C. J., editors, *Paleowaters in Coastal Europe: evolution of groundwater since the Late Pleistocene*, number 189 in Special Publications, pages 107–138. The Geological Society, London.

Marksamer, A. J. (2007). Integrated geophysical, hydrochemical, and hydrologic data to understand the freshwater resources on Nantucket Island, Massachusetts. Master's thesis, Indiana University.

Marshall, S. J., Tarasov, L., Clarke, G. K., and Peltier, W. R. (2000). Glaciological reconstruction of the Laurentide Ice Sheet: physical processes and modelling challenges. *Canadian Journal of Earth Science*, 37:769–793.

Masterson, J., Stone, B., Walters, D., and Savoie, J. (1997). Hydrogeologic framework of western Cape Cod. Hydrologic Investigations Atlas HA-741, U.S. Geological Survey.

McIntosh, J. and Walter, L. (2005). Volumetrically significant recharge of Pleistocene glacial meltwaters into epicratonic basins: Constraints imposed by solute mass balances. *Chemical Geology*, 222:292–309.

McKenzie, D. (1978). Some remarks on the development of the sedimentary basins. *Earth and Planetary Science Letters*, 40:25–32.

McKenzie, J. M., Voss, C., and Siegel, D. I. (2007). Groundwater flow with energy transport and water-ice phase change: Numerical simulations, benchmarks, and application to freezing in peat bogs. *Advances in Water Resources*, 30:996–983.

Metzger, J. M., Flemings, P. B., Christie-Blick, N., Mountain, G. S., Austin Jr., J. A., and Hesselbo, S. P. (2000). Late Miocene and Pleistocene sequences at the New Jersey outer continental shelf (ODP leg 174A, sites 1071 and 1072). *Sedimentary Geology*, 134:149–180.

Miller, K. G., Kominz, M. A., Browning, J. V., Wright, J. D., Mountain, G. S., Katz, M. E., Sugarman, P. J., Cramer, B. S., Christie-Blick, N., and Pekar, S. F. (2005). The Phanerozoic record of global sea-level change. *Science*, 310:1293–1298.

Morrissey, S., Clark, J. F., Bennet, M., Richardson, E., and Stute, M. (2010). Groundwater reorganization in the Floridan aquifer following Holocene sea-level rise. *Nature Geoscience*, 3:683–687.

Oldale, R. and O'Hara, C. (1980). New radiocarbon dates from the inner continental shelf off southeastern Massachusetts and a local sea-level-rise curve for the past 12,000 yr. *Geology*, 8:102–106.

Oldale, R. N. (1992). *Cape Cod and the Islands: The Geologic Story*. Parnassus Press, Illinois, 1 edition.

Peltier, R. (1996). Mantle viscosity and ice-age sheet topography. *Science*, 273:1359–1364.

Peltier, W. (1998). Postglaical variations in the level of the sea: Implications for climate dynamics and solid-Earth geophysics. *Reviews of Geophysics*, 36:603–689.

Person, M., Dugan, B., Swenson, J., Urbano, L., Stott, C., Taylor, J., and Millett, M. (2003). Pleistocene hydrogeology of the Atlantic continental shelf, New England. *Geological Society of American Bulletin*, 115:1324–1343.

Person, M., McIntosh, J., Bense, V., and Remenda, V. H. (2007). Pleistocene hydrology of North America: The role of ice sheets in reorganizing groundwater flow systems. *Reviews of Geophysics*, 45:RG3007.

Person, M., Raffensperger, J. P., Ge, S., and Garven, G. (1996). Basin-scale hydrogeologic modeling. *Reviews of Geophysics*, 34:61–87.

Person, M., Taylor, J. Z., and Dingman, S. L. (1998). Sharp Interface Models of Salt Water Intrusion and Wellhead Delineation on Nantucket Island, Massachusetts. *Ground Water*, 36:731–742.

Pirmez, C., Pratson, L. F., and Steckler, M. S. (1998). Clinoform development by advection-diffusion of suspended sediment: Modeling and comparison to natural systems. *Journal of Geophysical Research*, 103:24141–24157.

Poppe, L. J. and Poag, C. (1993). Mesozoic stratigraphy and paleoenvironments of the Georges Bank Basin: A correlation of exploratory and cost wells. *Marine Geology*, 113:147–162.

Pratson, L. F., Ryan, W. B. F., Moutain, G. S., and Twichell, D. C. (1994). Submarine canyon initiation by downslope-eroding sediment flows: Evidence in Late Cenozoic stratigraphy on the New Jersey continental slope. *Geological Society of American Bulletin*, 106:395–412.

Provost, A., Voss, C., and Neuzil, C. (1998). SKI SITE-94 Glaciation and regional ground-water flow in the Fennoscandian Shield. SKI Report 96, Stockholm: Swedish Nuclear Power Inspectorate.

Raymo, M. E. and Huybers, P. (2008). Unlocking the mysteries of the ice ages. *Nature*, 451:284–285.

Raymo, M. E., Lisiecki, L. E., and Nisanciogu, K. H. (2006). Plio-pleistocene ice volume, Antarctic climate, and the global $\delta^{18}O$ record. *Science*, 313:492–495.

Redfield, A. C. and Rubin, M. (1962). The age of salt marsh peat and its relation to recent changes in sea-level at Barnstable, Massachusetts. *Proceedings of the National Academy of Science*, 48:1728–1735.

Remenda, V. H., Cherry, J. A., and Edwards, T. W. D. (1994). Isotopic composition of old ground water from Lake Agassiz: Implications for Late Pleistocene climate. *Science*, 266:1975–1978.

Roy, M., Clark, P. U., Barendregt, R. W., Glasmann, J. R., and Enkin, R. J. (2004). Glacial stratigraphy and paleomagnetism of late Cenozoic deposits of the north-central United States. *Geological Society of American Bulletin*, 116:30–41.

Schlee, J. and Pratt, R. M. (1970). Atlantic continental shelf and slope of the United States - Gravels of the northeastern part. Professional Paper 529-H, U.S. Geological Survey.

Sharp, J. M. (1984). Hydrogeologic Characteristics of Shallow Glacial Drift Aquifers in Dissected Till Plains (North-Central Missouri). *Ground Water*, 22:683–689.

Siddall, M., Rohling, E. J., Almogi-Labin, A., Hemleben, C., Meischner, D., Schmelzer, I., and Smeed, D. A. (2003). Sea-level fluctuations during the last glacial cycle. *Nature*, 423:853–858.

Sosdian, S. and Rosenthal, Y. (2009). Deep-sea temperature and ice volume changes across the Pliocene-Pleistocene climate transaction. *Science*, 325:306–310.

Steckler, M. S., Mountain, G. S., Miller, K. G., and Christie-Blick, N. (1999). Reconstruction of Tertiary progradation and clinoform development on the New Jersey passive margin by 2-D backstripping. *Marine Geology*, 154:399–420.

Turcotte, D. and Schubert, G. (1982). *Geodynamics*. Jon Wiley and Sons, Inc.

Uchupi, E., Giese, G. S., Aubrey, D. G., and Kim, D. J. (1996). The late Quaternary construction of Cape Cod, Massachusetts: a reconsideration of the W.M. Davis model. *Geological Society of American Special Paper*, 309:1–69.

Uchupi, E. and Mulligan, A. E. (2006). Late Pleistocene stratigraphy of Upper Cape Cod and Nantucket Sound, Massachusetts. *Marine Geology*, 227:93–118.

Vialov, S. S. (1958). Regularities of glacial shields movement and the theory of plastic viscours flow. *International Association of Hydrological Sciences Publication*, 47:266–275.

Watts, A. (2001). *Isostasy and Flexure of the Lithosphere*. Cambridge University Press.

White, N. and McKenzie, D. (1988). Formation of the "Steer's head" geometry of sedimentary basins by differential stretching of the crust and mantle. *Geology*, 16:250–253.

Wieck, J., Person, M., and Strayer, L. (1995). A finite element model for simulating fault block motion and hydrothermal fluid flow within rifting basins. *Water Resources Research*, 31:3241–3258.